UNIVERSITA' DEGLI STUDI DI PAVIA

FACOLTA' DI INGEGNERIA
DIPARTIMENTO DI INGEGNERIA INDUSTRIALE E DELL'INFORMAZIONE

DOTTORATO DI RICERCA IN BIOINGEGNERIA E BIOINFORMATICA
XXX CICLO - 2017

METHODOLOGICAL AND PRACTICAL ISSUES IN TMDD MODELING WITH APPLICATION TO ONCOLOGY

PhD Thesis by
SILVIA MARIA LAVEZZI

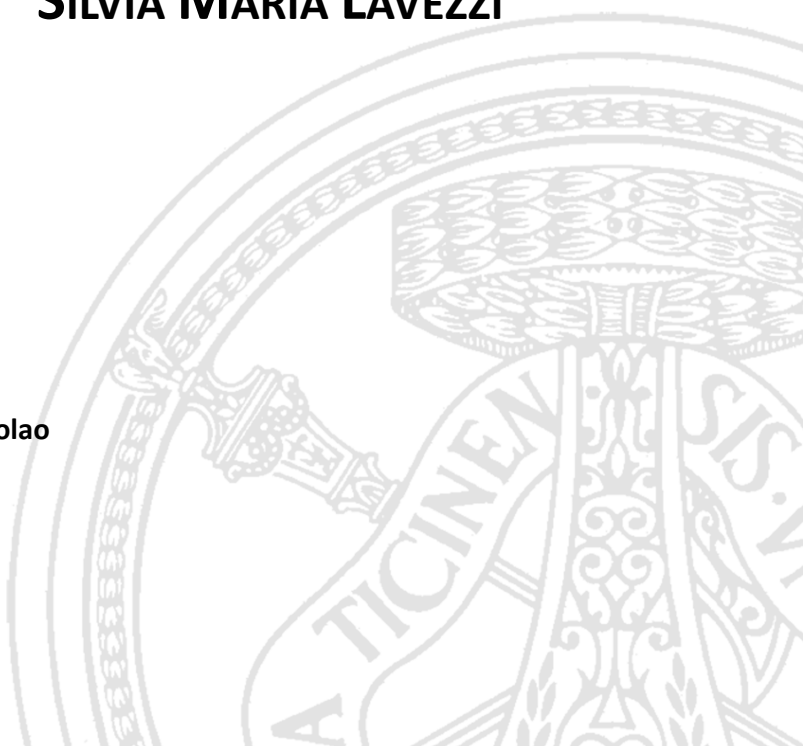

Advisor:
Prof. Giuseppe De Nicolao

PhD Program Chair:
Prof. Riccardo Bellazzi

For the things of this world cannot be made known without a knowledge of mathematics.

Roger Bacon

Abstract (English)

The process of drug development is long and burdensome as it requires a deep understanding of the underlying mechanisms of drug action and effect. This is particularly challenging when biological drugs are involved, as they display unique pharmacokinetic (PK) features, with respect to more well-defined chemical drugs. Monoclonal antibodies (mAbs) can be considered the most difficult biological drugs to characterize because of their large molecules and complex structures. They often display nonlinear PK, that is usually due, at least partly, to target mediated drug disposition (TMDD): the binding of the mAb to its pharmacological target influences its own disposition. Mathematical models are recognized as valuable tools to gain a deeper understanding of mAb PK, and in particular of the role played by the target on drug disposition. In this thesis, different models focusing on TMDD are explored theoretically and also applied on a real dataset in oncology, ranging from more complex and mechanistic models, to simpler empirical ones. More in detail, a minimal physiologically based PK (mPBPK) model is integrated with different mechanistic TMDD models, giving rise to four mPBPK-TMDD models. These are inspected with a particular focus on identifiability issues, to evaluate their use

for simulation and identification on real PK data. A TMDD model is then explored via a tool built with the R package Shiny, to demonstrate how to gain more confidence with the model at hand through simulations. Finally, an empirical model describing nonlinear PK built for an anticancer mAb is refined via covariate inclusion exploiting data coming from a real clinical trial, to confirm that the observed interaction with a co-administered small-molecule drug is partly due to TMDD. Overall, this thesis presents methods for exploring, building and refining mathematical models for mAb PK of diverse complexity. The application of these methods leads to a greater confidence with the model in use, allows the exploration of possible alternative study designs, and finally bears a deepening in the understanding of mAbs PK processes.

Abstract (Italian)

Il processo di sviluppo di farmaci è lungo e gravoso, anche perché è necessario conoscere approfonditamente i sottostanti meccanismi di azione ed effetto del farmaco; ciò può rappresentare una sfida in particolare per i farmaci biologici, che manifestano caratteristiche di farmacocinetica (PK) uniche rispetto ai farmaci di origine chimica. Gli anticorpi monoclonali (mAbs) possono essere considerati i farmaci biologici più difficili da caratterizzare, per via delle loro grandi molecole e delle loro strutture complesse. Per i mAbs, spesso si osserva una PK nonlineare, dovuta (almeno in parte) alla "target mediated drug disposition" (TMDD): i legami che si creano tra mAb e target farmacologico influenzano la disposizione del farmaco stesso. In questa tesi, diversi modelli focalizzati sul fenomeno del TMDD sono sia esplorati a livello teorico, sia applicati su un dataset reale in campo oncologico, passando dai modelli più complessi e meccanicistici, fino ad arrivare a modelli empirici più semplici. Più nel dettaglio, un modello minimo di PK basato sulla fisiologia (mPBPK) è integrato con diversi modelli TMDD meccanicistici, dando origine a quattro modelli mPBPK-TMDD. Questi vengono esaminati con un'attenzione particolare ai problemi di identificabilità, per valutare il loro uso per la

simulazione e l'identificazione su dati reali di PK. In seguito, un modello TMDD è esplorato tramite un tool costruito con il pacchetto R Shiny, per mostrare come acquistare maggiore confidenza con il modello in uso attraverso le simulazioni. Infine, un modello empirico che descrive una PK nonlineare, costruito per un mAb antitumorale, viene rifinito tramite l'inclusione di covariate sfruttando dati di uno studio clinico reale, per confermare che l'interazione osservata con una piccola molecola cosomministrata è dovuta in parte al TMDD. Nel complesso, questa tesi presenta metodi per esplorare, costruire e raffinare modelli matematici di diversa complessità per la PK dei mAbs. L'applicazione di questi metodi porta a una maggiore confidenza con il modello in uso, permette l'esplorazione di eventuali disegni di studio alternativi, e infine porta a un approfondimento nella comprensione dei processi di PK dei mAbs.

List of Abbreviations

BR bendamustine and rituximab (plus placebo)

BR-I bendamustine and rituximab, plus ibrutinib

BTK Bruton's tyrosine kinase

CH constant heavy

CI confidence interval

CL constant light

CLL Chronic Lymphocytic Leukemia

CV coefficient of variation

CWRES Conditional Weighted Residuals

CYP cytochrome P450 enzyme

DDI drug-drug interaction

DV dependent variable

Fab fragment antigen-binding

Fc fragment crystallizable

FcRn neonatal (or Brambell) Fc receptor

FIM Fisher Information Matrix

FOCE first-order conditional estimation

Fv fragment variable

GOF Goodness Of Fit

Ig Immunoglobulin

IIV inter-individual variability

i.m. intramuscular

INES INteractive Explorator and Simulator

ISF interstitial fluid

IV intravenous

mAb monoclonal antibody

MC Monte Carlo

ML Maximum Likelihood

MM Michaelis-Menten

mPBPK minimal PBPK

MPS mononuclear phagocyte system

MW molecular weight

NHL non-Hodgkin's Lymphoma

NLME nonlinear mixed-effects

PBPK physiologically based pharmacokinetic(s)

PD pharmacodynamic(s)

PK pharmacokinetic(s)

PP Predictive Plot

PTS Probability of Technical Success

QE quasi equilibrium

QSS quasi-steady-state

RMSE Root Mean Square Error

s.c. subcutaneous

SE standard error

SLL Small Lymphocytic Lymphoma

SPD Sum of the Products of the two largest Diameters (of the selected lesions)

TMDD target mediated drug disposition

VH variable heavy

VL variable light

VPC visual predictive check

Contents

List of Figures

List of Tables

Chapter 1

Introduction

1.1 Background

1.1.1 Pharmaceutical research and development

The process of drug discovery and development, from compounds selection to clinical approval, involves a number of challenges, such as the selection of the right patient population or the right dose, and, at the same time, the restraint of costs and time expenses [8]. This is demonstrated by the high attrition rates (i.e. new compounds failure rates) observed in all development phases, in particular in the later stages. In the clinics, less than 10% of new compounds entered in Phase I eventually receive approval [9, 10]. The situation is even worse in the oncology therapeutic area [11], where the successful compounds percentage is reduced to about 5% [10]. Therefore, the need to improve decision-making processes (e.g., dose selection, go/no go decisions) is apparent, so as to save time and money that can be diverted to more promising drug candidates [9].
Pharmaceutical compounds can be divided in two main classes: chem-

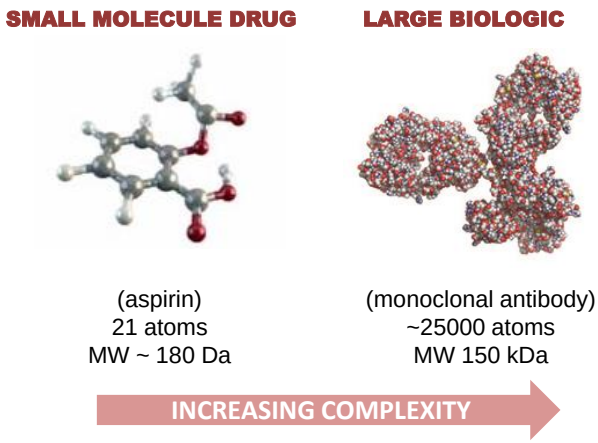

Figure 1.1: Illustrative representation of a chemical small-molecule drug versus a biologic compound, highlighting differences in structure, number of atoms, and molecular weight (MW).

ical medicinal products, manufactured using chemical sources and processes, and biologics (also called biopharmaceuticals), inherently biological in nature and manufactured using biotechnology [12]. Chemical drugs usually consist in small molecules, with well-defined structures; biologics instead are much larger, have more complex structures and peculiar biological/biophysical characteristics, which lead to a difficult characterization of the compound [12, 13, 14] (Figure 1.1). Biopharmaceuticals, with respect to small molecules, have unique pharmacokinetic (PK) characteristics (e.g., slower absorption rate, confined distribution, and long half-life) and they are generally designed for a specific target [13].
As with small-molecule drugs, pharmaceutical research and development of biologics is expensive and risky [15].

1.1.2 Pharmacometrics in drug discovery and development

The difficulties and the open challenges of pharmaceutical research and development have been frequently debated over the years, to underline the most critical passages and to suggest possible solutions. Pharmacometrics, i.e. mathematical modeling applied in the pharmaceutical context, has been recognized as a valid tool to help in achieving an effective drug discovery and development process [1] (see e.g. [8, 16, 17, 18]). Regulatory agencies as well have supported the value of Model Informed Drug Discovery and Development (MID3), i.e., in other words, the application of mathematical modeling to integrate knowledge and generate inference from compound, mechanism and disease level data, in terms of predictions and extrapolations [1, 9, 19]. Mathematical models describe the temporal relationships between drug administration according to a particular dosing regimen, drug exposure and therapeutic/toxic effects.
The system under exam (e.g. the human body) is seen as a set of compartments, where the drug enters, distributes and transforms, exerting its mechanism of action. Model equations are based on the mass conservation principle and they usually consist in differential equations. According to the empirical approach, compartments do not represent specific organs, but instead material ensembles behaving homogeneously either in terms of their kinetic properties (e.g. tissues rapidly/slowly equilibrating with blood) or in terms of physiological grounds (e.g. organs involved in excretion). The interconnections between compartments represent material flows, e.g. actual drug transportation or drug transformation via chemical reactions. According to the physiologically-based approach, each compartment represents an organ or tissue (or a group of tissues that behave similarly) and has a size and blood flow that mimics those of the organ in vivo [13, 20]; compartments are joined together via blood or lymph flows. Interest-

ingly, with this approach, it is possible to extrapolate (i) to conditions where the physiological processes are altered (e.g. disease states), and (ii) across different species (accounting for differences in blood flow, organ sizes, etc.) [20].
Besides what is known about the compound and the underlying PK and/or PD processes, also the uncertainty in the knowledge can be taken into account via mathematical modeling. Indeed, the so called mixed-effects (or population) models include also random variability observed in both exposure and response for all drugs, that might be partly explained by inter-individual differences. Such models, besides a deterministic structure which describes the input-output relationships, present also a statistical structure which allows the quantification of random variability on parameters and/or observations. Furthermore, in these models, individual characteristics (i.e. covariates), such as body weight, age, sex, concomitant medications, etc., can be included to evaluate their influence on drug exposure and response [21].
Pharmacometrics help addressing important scientific issues, such as the evaluation of administration pathways, the selection of the dosing regimen, the characterization of drug-drug interactions (DDIs) or drug-disease interactions, or prediction of study outcome in terms of PK and/or pharmacodynamic (PD) endpoints (Figure 1.2, see also [1]). In this way, mathematical modeling supports decision-making (e.g. go/no go decisions), thus helping in controlling costs.
Via mathematical models, data collected throughout drug development can be progressively integrated at each stage, also incorporating relevant previous information and/or clearly stated assumptions. Mathematical models can be considered as a knowledge repository [17], and hence help in leveraging existing knowledge and in enhancing the information gain [8, 18].
In particular, pharmacometrics can help in filling knowledge gaps about the unique PK features of biologic drugs, such as monoclonal antibodies (mAbs), cytokines, recombinant proteins, fusion proteins,

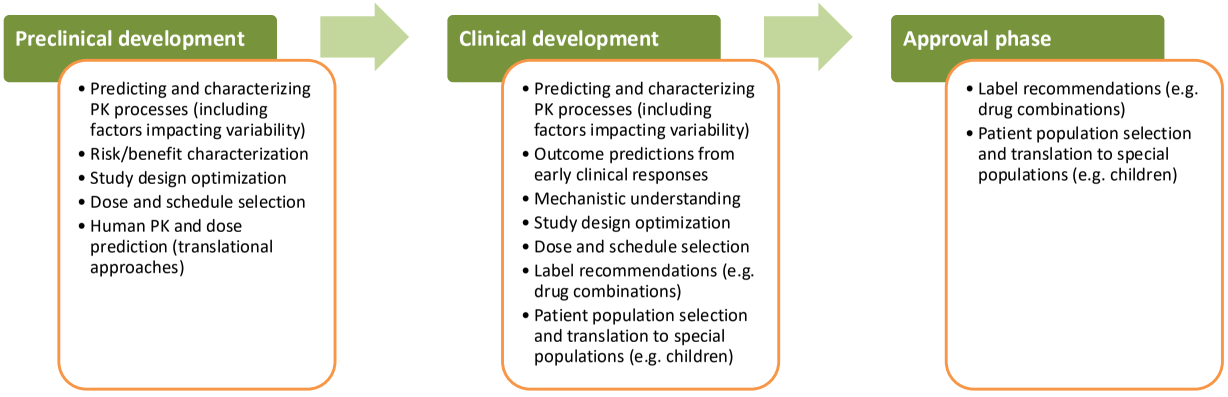

Figure 1.2: Examples of possible applications of pharmacometric approaches at different stages of drug development (figure adapted from Figure 1 in [1]). The list is not exhaustive: pharmacometrics can be used at each stage for a number of different purposes, and the same purpose can be pursued across different stages. For a more complete review of scientific issues tackled by modeling approaches see [1].

antibody fragments, antibody-drug conjugates. Mathematical models not only may help in leveraging the available incomplete information, but they are also important to generate additional information [5, 22]. This is of special interest as biopharmaceuticals are becoming an important class of products in drug development, because of their promise and potential [13, 23]. Furthermore, most of them target difficult-to-treat populations, with indications ranging from oncology and autoimmunity to orphan and genetic diseases [23]. Pharmacometrics can offer a valid tool to guide their development at various stages, and is useful for optimizing the dosing and sampling schedules [5, 23].

1.1.3 Monoclonal antibodies

The majority of biologic products consist of mAbs, followed by cytokines and growth factors. The research and development of mAbs is a rapidly progressing field, and, given the technological advances, it is not likely to slow in the near future [21]. The number of mAbs currently under development is over 500 [20].
Processes determining the PK properties of mAbs and functional derivatives are very different from those of small chemical molecules. mAbs can be considered the most complicated biologic products to characterize. Indeed, they are the largest molecules currently available, with molecular weight (MW) around 150 kDa and complex secondary and tertiary structures. The main pharmacological characteristics of mAbs are described in Chapter 2 of this thesis.
Multiple factors, such as charge, size, and target affinity, can affect the PK of mAbs, which all could have an impact on their efficacy and safety [23]. mAbs PK behavior, like for small molecules, can be described by the processes of absorption, distribution, metabolism and elimination [20]; nevertheless the underlying mechanisms that govern such processes are not fully known.
A further avenue that should be explored regards the DDIs that may

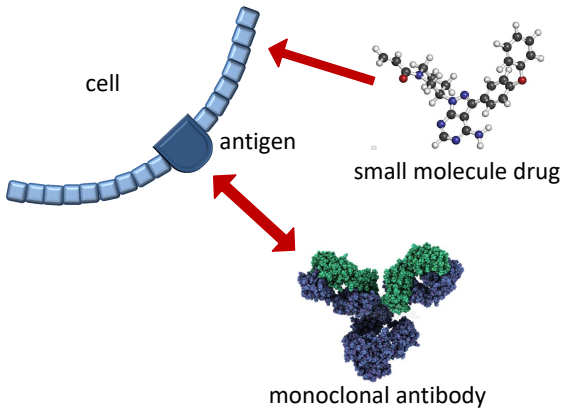

Figure 1.3: Schematic representation of DDI where the small molecule acts as a perpetrator and the monoclonal antibody is the victim. The small molecule drug, through its mechanism of action, interacts with the cell expressing the antigen, for instance inducing its depletion. The mAb and the antigen bind and start the cascade of events involved in the mAb mechanism of action and in its disposition and elimination.

occur between mAbs or between a mAb and a small molecule. In particular for certain therapeutic areas, such as oncology, to gain greater clinical benefit, biologics are increasingly being combined with small molecules and/or with other biologics [23]. For many years there was a perception that therapeutic proteins do not exhibit drug interactions when administered with small molecules, because of the different drug mechanisms. Nevertheless, in the last years the interest for DDIs involving mAbs has grown and numerous interactions have been reported [20]; frequently, the small molecule acts as a perpetrator of the DDI by interacting with the target of the protein, leading to changes in target mediated clearance [21] (see Figure 1.3).

1.1.4 Mathematical models for mAbs

Population analyses are routinely employed in most development programmes to characterize the PK-PD profile of mAbs, and their results are often reflected in drug labeling [5, 13, 23]. Mathematical models are used in particular to quantify large molecules peculiar disposition features, sources of variability, and impact of covariates on exposure and/or response.
Regardless of the PK behavior, the therapeutic antibodies PD is often described via indirect response models, accounting for lag periods between drug administration and response. In most cases, mAb PK appears to be nonlinear, and it can be influenced by different factors, such as receptor shedding, the patient disease state, and the physiology of the system being targeted [5].
Numerous models have been proposed to describe mAb PK, ranging from the mechanistic physiologically-based to the more empirical compartmental ones (Figure 1.4); a brief review is presented in this thesis in Chapter 3.

Physiologically-based PK (PBPK) models can be used to describe mAbs PK, taking into account the physiological processes underlying their disposition, and evaluating mAbs concentration also in the organ where the target is located. PBPK has been used for understanding mAb delivery; a template PBPK model for mAbs was provided by Shah and Betts in [2]. Nevertheless, building a PBPK model is lengthy and burdensome, due to lack of tissue concentration data, parameter availability, and parameter identifiability [13]. Compartmental lumping is a common technique used to simplify the system [13]: tissues that behave similarly may be fused together (lumped), maintaining the mechanistic ground of the model and reducing at the same time the number of parameters [24, 25]. In this way, the so-called minimal PBPK (mPBPK) models are obtained. The description of the mPBPK model for mAbs proposed in [3] is provided in Chapter 3.

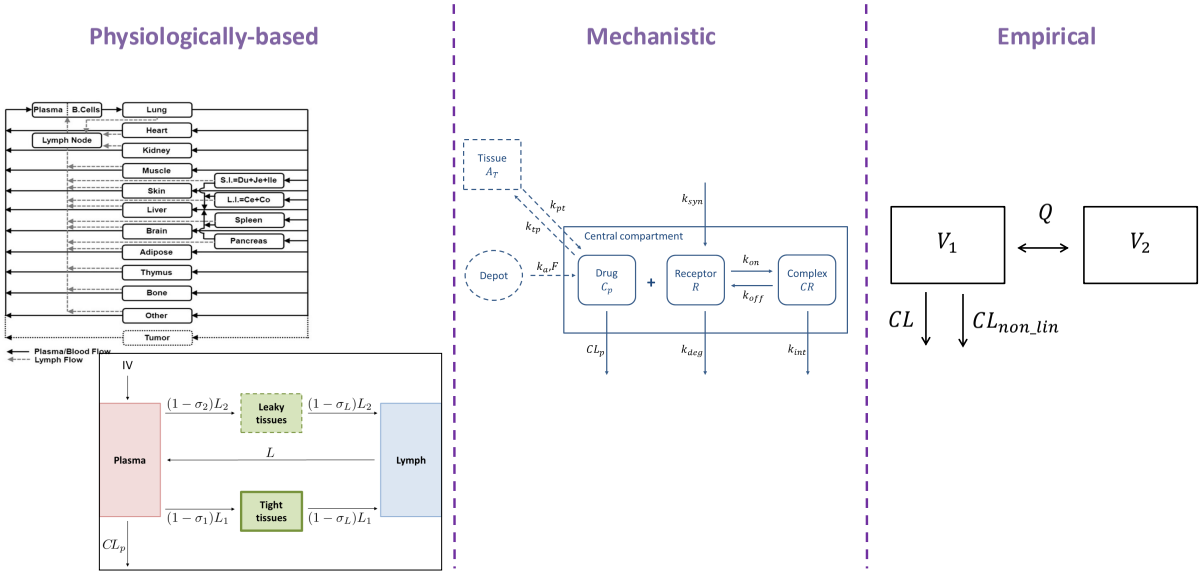

Figure 1.4: Schematics of the three types of PK model proposed for mAbs. On the left, two examples of physiologically-based models: the one proposed in [2], and the minimal version proposed in [3]. In the middle, the full TMDD model as introduced in [4], and on the right an empirical compartmental model with linear and nonlinear elimination.

Simpler compartmental mechanistic models may be considered, in particular to simultaneously describe the dynamics of drug disposition and target engagement. The nonlinearity observed in PK for the majority of mAbs is often due to target mediated drug disposition (TMDD), i.e. the phenomenon according to which drug-target binding significantly influences mAb PK. For this reason, mechanistically-grounded TMDD models are commonly used. A full TMDD model was proposed in [4] (see Chapter 5 for an exploratory analysis of this model); a number of approximated models, exploiting simplifying assumptions, were also introduced [13] (see Chapter 3). The integration of TMDD models within the mPBPK framework [3] is thoroughly evaluated in Chapter 4. As they are mechanistically-grounded, TMDD models provide unique advantage in understanding drug mechanism of action and effects. In particular they can provide insight into the antibody-target interaction and in target concentration profiles [13, 20]. As TMDD models may be difficult to identify based on the available data [23], in experimental practice it is often necessary to resort to more empirical models.

Two-compartmental models, with linear and/or nonlinear elimination, are the most used for describing mAb PK, where the nonlinear pathway may be attributed to saturation of target mediated clearance pathways [23]. This kind of model, with both linear and nonlinear clearance components, was proposed for rituximab PK in Chronic Lymphocytic Leukemia (CLL) patients [7], and it is refined via demographic and PD covariates inclusion in Chapter 6. Even though they do not offer any mechanistic understanding, empirical compartmental models offer a viable way to identify mAb PK on commonly available data.

In general, PK models used for mAbs are often similar, notwithstanding the differences in their pharmacological targets, their therapeutic indications, and the disease status of the selected patient populations. This might be due, at least in part, to the similarities in the molecular structure [23].

1.2 Thesis main contributions and overview

The general aim of the thesis is to increase the understanding of the PK behavior of mAbs, both in terms of physiological understanding and in terms of modeling. Models for mAbs PK, taking into account TMDD, are here investigated.
First, a methodological approach for assessing mPBPK and TMDD models integration is proposed. Moreover, an exploratory simulation analysis is performed with a newly developed tool to highlight some key aspects of the full TMDD model (e.g., dose-dependence, variability impact). Finally, a DDI between a mAb and a small molecule drug is studied based on real clinical data.
The first project helps in gaining a better insight into complex PK models, and provides suggestions on their practical use. For instance, the type and the amount of data needed to identify mPBPK-TMDD models are given particular attention. The second project demonstrates that even an exploratory simulation analysis can prove helpful to detect identifiability issues and gain general confidence with the full TMDD model. The third project, dealing with the refinement of an empirical mAb PK model to describe an observed DDI, gains a deeper mechanistic understanding of both the mechanism of action of the mAb and its interaction with the small molecule.

The thesis is organized in seven chapters (Introduction included), and two appendices.

- Chapter 2 details pharmacological and PK properties of mAbs, with a special mention to drug-drug interactions, and mAbs use in clinical oncology.

- Chapter 3 reports the state of the art of the empirical and mech-

anistic models employed for mAbs PK characterization.

- Chapter 4 presents the thorough exploration of four models integrating a mPBPK model with four different TMDD components. Such explorations consist in simulation and identifiability analyses; the aim is to evaluate the use of mPBPK-TMDD models for different research objectives.

- Chapter 5 demonstrates the usefulness of a simulation software tool (called INES, i.e. INteractive Explorator and Simulator) in investigating a simpler yet mechanistically grounded TMDD model. In particular, different scenarios (different doses/parameters) and the impact of random variability on model outcomes are explored.

- Chapter 6 is about the application and refinement (via covariate inclusion) of an empirical model for mAb PK, based on data coming from a real clinical trial, in the context of cancer research.

- Chapter 7 concludes the thesis, highlighting the key messages and contributions of each chapter and of the thesis in general.

- Appendix A includes theoretical definitions of the model properties assessed in Chapter 4 for the presented mPBPK-TMDD models. Furthermore, software implementation details for properties assessment are provided.

- Appendix B presents the simulation software tool INES, introduced in Chapter 5, in terms of general encoding, structure, and main features. Furthermore, a corollary tool for the computation of Probability of Technical Success (PTS), called "PTS app", is also briefly described.

The majority of the contents reported in this thesis are the result of scientific collaboration with pharmaceutical industries, which are detailed in the next section.

1.3 Collaborations and related publications

The material of Chapter 4 (and related Appendix A) is the result of a collaboration with GlaxoSmithKline, Clinical Pharmacology Modeling and Simulation group (*project leader*: Monica Simeoni).
A related journal publication is being submitted; the work has already been partially presented in:

- E. Mezzalana, S.M. Lavezzi, S. Zamuner, G. De Nicolao, P. Ma, M. Simeoni, Integrating target mediated drug disposition (TMDD) into a minimal physiologically-based modelling framework: evaluation of different quasi-steady-state approximations. *Population Approach Group in Europe (PAGE),* 24^{th} *meeting*, Hersonissos, Crete, Greece, June 2015.

- S.M. Lavezzi, S. Zamuner, G. De Nicolao, P. Ma, M. Simeoni, Structural and practical identifiability of some mPBPK-TMDD models. *Population Approach Group in Europe (PAGE),* 25^{th} *meeting*, Lisbon, Portugal, June 2016.

The material of Chapter 5 (and related Appendix B) is the result of a project developed in collaboration with Janssen Research and Development, Global Clinical Pharmacology group (*project leaders*: Italo Poggesi, Daniele Ouellet). A related poster publication is:

- S.M. Lavezzi, Y. Cherkas, N. Haddish-Berhane, S. Jagannatha, G. De Nicolao, D. Ouellet, I. Poggesi, Probability of Technical

Success of a New Molecular Entity in the Preclinical to Clinical Translational Phase. *Population Approach Group in Europe (PAGE),* 26^{th} *meeting*, Budapest, Hungary, June 2017.

The material of Chapter 6 was also developed in collaboration with Janssen Research and Development, Global Clinical Pharmacology group (*project leader*: Italo Poggesi).
This work will be reported in a journal article, and it was partly published in:

- P. Cramer, F. Demirkan, G. Fraser, A. Pristupa, N.L. Bartlett, M.-S. Dilhuydy, J. Loscertales, A. Avigdor, S.A. Rule, O. Samoilova, A. Goy, S. Ganguly, I. Poggesi, S.M. Lavezzi, G. De Nicolao, J. de Jong, M. Neyens, M. Salman, A. Howes, M. Mahler, Systemic Exposure of Rituximab Increased By Ibrutinib: Pharmacokinetic Results from the Helios Trial. *ASH 58* (Blood 2016), Abstr 4403

- P. Cramer, F. Demirkan, G. Fraser, A. Pristupa, N.L. Bartlett, M.-S. Dilhuydy, J. Loscertales, A. Avigdor, S.A. Rule, O. Samoilova, A. Goy, S. Ganguly, I. Poggesi, S.M. Lavezzi, G. De Nicolao, J. de Jong, M. Neyens, M. Salman, A. Howes, M. Mahler, Ibrutinib increases the systemic exposure of rituximab: pharmacokinetic results from the Helios trial. *14-ICML*, Hematological Oncology, 35 (S2), 232-233 (2017)

- S.M. Lavezzi, J. de Jong, M. Neyens, P. Cramer, F. Demirkan, G. Fraser, A. Pristupa, N. Bartlett, M.-S. Dilhuydy, J. Loscertales, A. Avigdor, S. Rule, O. Samoilova, A. Goy, S. Ganguly, M. Salman, A. Howes, M. Mahler, G. De Nicolao, I. Poggesi, Modelling of rituximab clearance reduction due to ibrutinib coadministration. *Population Approach Group in Europe (PAGE),* 26^{th} *meeting*, Budapest, Hungary, June 2017.

Chapter 2

Monoclonal antibodies

2.1 Structure and general properties

Antibodies, also called immunoglobulins (Igs), are large proteins produced by animals and humans to identify and neutralize foreign objects, such as bacteria and viruses [26, 27]. Igs are grouped into five classes, on the basis of their molecular mass and antigen-binding capacity: IgA, IgD, IgE, IgG and IgM. Among these, IgG is the predominant class, comprising $\sim 80\%$ of the Igs in human serum. An antibody is composed of a basic Y-shaped unit with three major structural domains: two identical Fabs and an Fc domain (Figure 2.1). Each Fab (fragment antigen-binding) contains an antigen-binding site. The Fc (fragment crystallizable) contains structural features that determine the downstream consequences of antigen binding, often called the effector function of the antibody. For example, the Fc portion determines whether binding to a cell surface receptor prevents signaling through that receptor or causes the cell's destruction. The Fc domain also contains the binding site for the neonatal (or Brambell) Fc recep-

tor (FcRn), which mediates vectorial transport of the antibody across some cellular membranes [28]. Each Ig molecule contains two identical heavy chains and two identical light chains [29, 27, 28]. The heavy chain domains are designated as VH, CH1, CH2, and CH3, where V denotes "variable" and C denotes "constant" regions. The light chain domains are designated as VL and CL. The antigen-binding region is formed by the variable domains of the heavy and light chains (Fv) [28].

mAbs are a class of highly specific antibodies, produced via the hybridoma technology developed in 1975 by Köhler and Milstein [30], in which mAbs are produced by a single clone of transformed B cells [31, 26]. In particular, the fusion of a B cell producing a single antibody, and a myeloma cell results in an immortal antibody-producer B cell, called a hybridoma. mAbs produced by a clone cell population have the same PK (e.g., distribution, elimination) and PD properties (e.g., affinity, mechanism of action) properties [31]. mAbs were first shown to have potential for therapeutic activity in the clinic in 1982 [5]. All of the approved therapeutic antibodies are of the IgG class [29, 27, 28]. Intact IgGs have MW $\sim$ 150 kDa and they have a much longer elimination half-life compared to the other classes (IgA, IgD, IgE, IgM) [29]. IgGs can be in turn divided into four subclasses, based on the structure of their heavy chains: IgG1, IgG2, IgG3, and IgG4. In the development of new mAbs, Ig isotypes are mostly chosen with long elimination half-lives: as IgG3 has a much shorter elimination half-life (7 days) than those of the other IgG subtypes (20-21 days), none of the approved mAbs is of this subtype. The long serum half-life is a distinctive advantage over conventional low-molecular-mass drugs, as it allows infrequent dosing. Furthermore the high specificity of therapeutic mAbs facilitates precise action and limits off-target toxicity [27, 32].

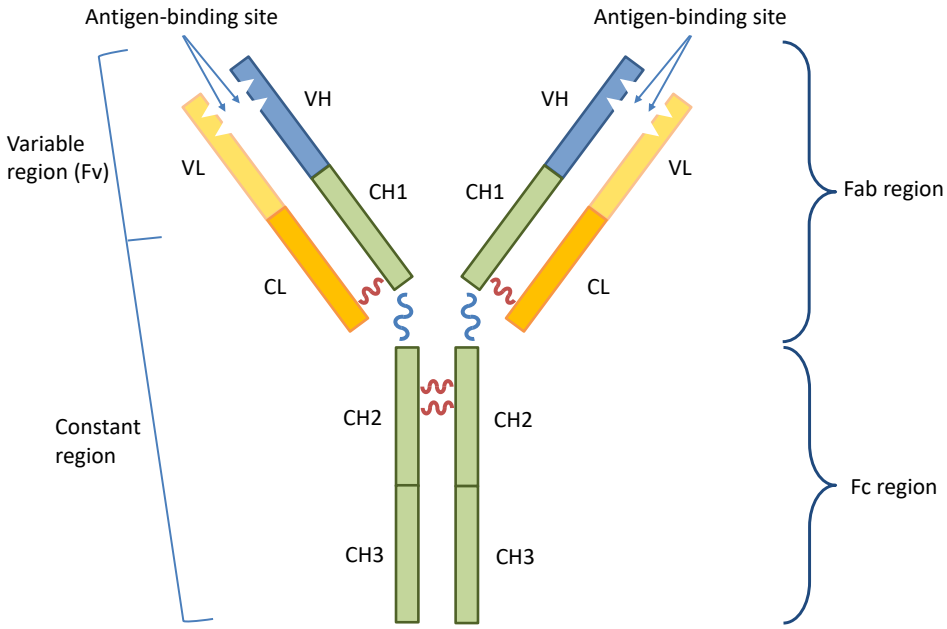

Figure 2.1: A schematic representation of the structural and functional domains of Igs. Fc and Fab regions can be distinguished, the latter containing antigen-binding sites. Light chains variable and constant domains are indicated respectively with VL and CL. Each heavy chain is composed of one variable domain, denoted with VH, followed by a constant domain, denoted with CH1, a hinge region (blue wavy line), and other two constant domains, i.e. CH2 and CH3. The red wavy lines indicate interchain disulfide bonds.

2.2 Classification

The first mAbs were generated from mouse and rat hybridomas. These first-generation antibodies found only limited success in the clinic because of their short half-lives and the induction of immunological response (immunogenicity). Indeed, sensitization to mAb therapeutics poses significant risk to the patient and may blunt the efficacy of these therapies [26]. A number of approaches have been developed to humanize rodent antibodies, eliminating xenogeneic protein [31, 27]. A first step was the development of chimeric mAbs, which are made of mouse variable regions and human constant regions (reducing the mouse protein sequences to about 33% of the total molecule) [27, 28]. A further refinement of this approach resulted in humanized mAbs [31, 28], where $90 - 95\%$ of the antibody is composed of sequence derived from human IgG [27]. The bioengineering strategy even led to the development of "fully human" mAbs [31, 28] (see Figure 2.2). The reduced immunogenity of this new generation of mAbs is expected to enhance efficacy, safety, and ease of use [26].

2.3 Mechanism of action

The pharmacological effects of antibodies are initiated by the noncovalent interaction between antibody and antigen (also referred to as receptor, or target) [28]. mAbs target a specific (most commonly endogenous) antigen with high affinity. Affinity is expressed, in molar units, as the antibody-antigen dissociation constant k_D, and it represents the strength of the (reversible) association between antibody and antigen. Affinity is a primary determinant of the concentration of antibody required to bind to a given fraction of target, thus it is important for therapeutic dose evaluation [28]. mAbs induce their

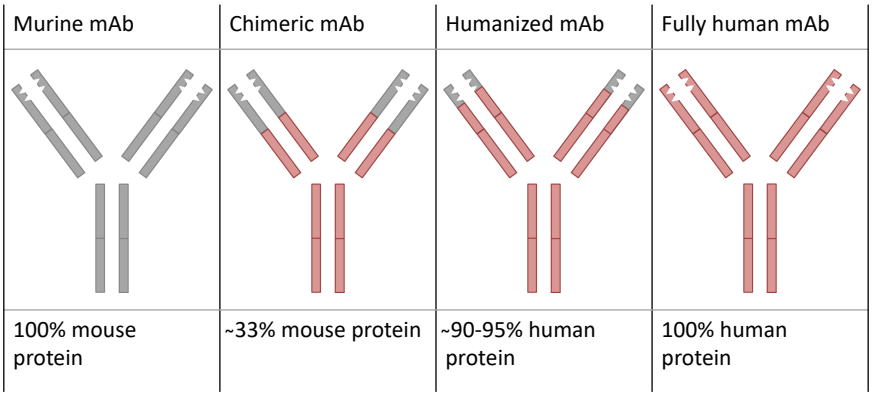

Figure 2.2: Classification of mAbs according to the degree of humanization.

therapeutic effect via a number of mechanisms, which may be classified into four categories: induction of cell lysis following binding to a cell surface receptor; neutralisation of an exogenous or endogenous molecule (e.g., a toxin or a cytokine); alteration of cellular functions (e.g. immunosuppression); delivery of toxic or radioactive agents to target cells [31]. Most mAbs act through multiple cooperative mechanisms and may interact with concurrent therapies [28] (see Section 2.4.5).

2.4 Pharmacokinetics

mAbs are hydrophilic high MW proteins: besides their pharmacological mechanism, also their PK features are therefore different from those of small-molecule drugs (MW $< 1,000$ Da) [29]. However, like conventional drugs, mAbs undergo absorption, distribution and elim-

ination processes [31].

2.4.1 Administration and absorption

mAbs are commonly administered intravenously. Intravenous (IV) route allows the administration of large volumes and total and immediate systemic delivery. However, IV injection may not always be appropriate: hour-long infusions require a hospital environment and are often associated with side effects [26]. Hence, some therapeutic antibodies are administered extravascularly by s.c. or i.m. injection [31]. Absorption into the systemic circulation after s.c. or i.m. injection occurs via lymphatic drainage, therefore it is a slow process. Because of this, it generally takes a few days (typically from two to eight [27]) to reach the peak plasma concentration after a single dose. Extravascular routes do not allow the administration of large volumes and lead to higher PK variability [31]. Oral administration of mAbs for systemic therapy is not indicated, because of their size, polarity and gastrointestinal degradation [29]. Indeed, oral bioavailability is negligible, while absolute bioavailability after s.c. or i.m. administration is generally reported between 50 and 100% [13, 27].

2.4.2 Distribution

The distribution of mAbs is determined by the rate of extravasation and distribution in tissue, the rate and extent of antibody binding in tissue, and the rate of elimination from tissue. Because of polarity and molecule dimension, mAbs diffusion across vascular endothelial cells is very slow, and convection is believed to be the primary mechanism responsible for the transport from blood to interstitial fluid (ISF) of tissues [29, 31, 27]. The reflection coefficient of a tissue is an indicator of the fraction of solvent that does not filter through the tissue pores: if it is $\ll 1$ the solvent can easily extravasate in the tissue, while if it

is close to 1 the solvent is not allowed to pass.
For mAbs, tissue reflection coefficients are often assumed to be equal in all tissues, with values in the range of $0.95 - 0.98$. However, it is likely that reflection coefficients may be much lower in tissues where the vascular endothelium is known to be fenestrated or "leaky" (i.e. there are pores in the endothelial cells). Lymphatic vessels are much larger than paracellular pores that may be found in vascular endothelium. therefore, it is assumed that antibodies have relatively little restriction in moving via convection through the lymph [27]. For this reason, typically reflection coefficients of $0 - 0.2$ are assumed for convective elimination of antibody via lymphatic drainage.
About half of native IgG was found distributed in extravascular space; because of mAbs limited cellular permeability, ISF is considered the primary extravascular distribution space. Convective uptake into tissue and convective elimination from tissue are not equally efficient: mAbs concentrations in ISF are substantially lower than in plasma. In many tissues, concentrations of unbound IgG are approximately tenfold lower than concentrations in plasma (however, higher concentrations are observed in leaky tissues). Distribution of IgG antibodies to the brain is poor: mAbs have a limited ability to penetrate to the brain and cerebrospinal fluid, indeed endogenous IgG levels in CSF are $\leq 1\%$ of levels in serum [28, 33].
If the target of mAbs is localized in tissue, slow distribution might be an obstacle for clinical efficacy. Indeed, according to the "binding-site barrier" hypothesis, the antigen may be present in high concentrations in peripheral tissue, leading to tight binding to cells near the sites of extravasation. As a result, the antibody is confined to regions surrounding blood vessels, and hence its distribution deeper into the tissue is limited. The use or large mAb doses saturating binding sites may resolve the situation: however, such doses may not be feasible and/or give rise to off-target toxicities [23, 29, 27].
Because of the slow and/or low distribution, mAbs usually have small

volumes of distribution, approximately equal to plasma volume [29, 31].

2.4.3 Metabolism and elimination

Renal elimination is a primary pathway of clearance of small-molecule drugs, but it is relatively unimportant for IgGs, as their large size prevent efficient glomerular filtration. Metabolism of endogenous IgG occurs in various body tissues and in plasma. It is also possible that a significant fraction of drug elimination occurs from tissue sites that do not rapidly equilibrate with plasma [27]. Using PBPK modeling, the contribution of various organs to the elimination of endogenous IgG was estimated: 33% for skin, 24% for muscle, 16% for liver, and 12% for gut tissue [29].
Several mechanisms are reported to be involved in the elimination of Igs. The most important is catabolism: the first step of this process is proteolysis, i.e. breaking the mAb protein down into amino acids, mediated by liver and mononuclear phagocyte system (MPS) [29]. In particular, MPS (i.e. the part of the immune system consisting of the phagocytic cells, such as macrophages and monocytes, located in reticular connective tissue) is expected to play a role in the elimination of mAbs, as these are also key factors in the elimination of endogenous IgG. Internalization and subsequent degradation of IgG by lysosomes in these cells occur predominantly after binding of the Fc part of the antibody to Fcγ-receptors expressed on these cells. Nevertheless, as therapeutically administered mAbs are generally a small fraction of total endogenous IgG, it is not likely that this route is easily saturated by therapeutic mAbs [29, 27]. Furthermore, intracellularly, a mechanism is present that protects IgGs from subsequent rapid intracellular catabolism, mediated by FcRn [29]. This is expressed on hepatocytes, endothelial cells, and phagocytic cells of the MPS. When IgG undergoes endocytosis, the acidic pH of the endosome promotes binding of

the IgG Fc domain to FcRn, which recycles IgG to the cell surface and salvages IgG from lysosomal degradation [28]: the IgG-FcRn complex is transported back to the cell surface and released again into the circulation, while unbound IgG is degraded to amino acids by lysosomes that are present in the cell (Figure 2.3). The long elimination half-life of endogenous IgG (21 days) compared with those of other plasma proteins and its increased clearance at higher concentrations can be explained by binding of IgG to the FcRn. Moreover, the low affinity of human FcRn for mouse IgG helps to explain the very rapid elimination of murine mAbs in humans [31, 27]. The FcRn-mediated protective mechanism is not saturated by endogenous IgG and by most mAbs at their therapeutic dose [27]; very high doses of therapeutic mAbs (or mAbs with high affinity for FcRn) would be necessary to achieve saturation [29].

Another important elimination route for mAbs is due to TMDD: this is the primary route of antibody clearance. The term TMDD was first coined by Levy [34], to describe the phenomenon in which a drug is bound with high affinity and to a significant extent (relative to dose) to its pharmacologic target, such that this interaction is reflected in the PK characteristics of the drug itself [4]. Target mediated elimination consists in degradation within the target cells, after endocytosis [27]. The free antigens on target cells surface bind to the Fab domains of the antibody, serving as a sink; for this reason, this phenomen is also referred to as "antigen sink" [29, 28]. This mechanism is saturable because of finite target availability [27]. The rate of uptake and elimination of antibodies by target mediated pathways is a function of dose and the expression level of the target, as well as a function of the kinetics of receptor internalization and intracellular catabolism. The majority of marketed antibodies demonstrate nonlinear kinetics [29]: dose-dependent elimination consistent with target mediated elimination (i.e. clearance decreases as a function of dose) is frequently observed [27].

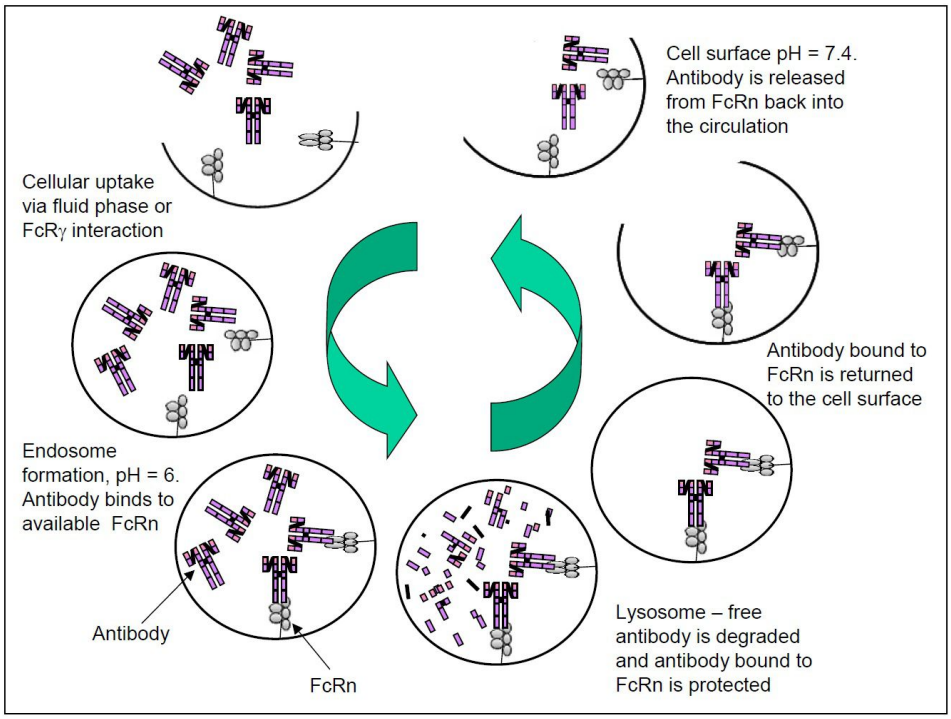

Figure 2.3: Schematic reported in [5] for IgG salvage due to Brambell receptors.

2.4.4 Immunogenicity

Besides the mechanisms discussed above, several other factors are important in the disposition of mAbs. mAbs are exogenous proteins and can therefore induce an immune response [31] that negatively impact the antibody's PK, safety and efficacy profile [27, 28]: this phenomenon is called immunogenicity. When an immune reaction occurs, newly formed endogenous antiglobulins may bind to the mAb, altering elimination rates [29]. Antiglobulin responses are designated according to the therapeutic antibody construct: human anti-mouse antibodies (HAMA), human anti-chimeric antibodies (HACA), and human anti-human antibodies (HAHA) [29, 28]. Accelerated clearance of therapeutic antibodies or neutralization of the antigen-binding domain due to immunogenicity can result in loss of product efficacy, impaired antigen targeting, or interference with antibody-based diagnostic tests. Serious safety risks may also be associated with immunogenicity: adverse reactions may be local or systemic and may vary from mild injection site reactions to life-threating anaphylaxis [28]. All therapeutic antibodies approved to date have shown some degree of immunogenicity [27], even in immunosuppressed patients. The development of humanization technology has successfully decreased the incidence of immunogenicity observed with murine and chimeric mAbs [28]. Indeed, in general the impact of the immune response is inversely dependent on the grade of humanization of the antibody [29, 31]. However, since humanized antibodies still present residual murine protein, and human antibodies have unique idiotypes [27, 28], immunogenicity concerns have not been eliminated. Besides antibody type, other factors associated with immunogenicity include duration of therapy, dose, and route of administration [27].

2.4.5 Drug-drug interactions

In contrast with small-molecule drugs, DDIs occurring through effects on enzyme systems (e.g. cytochrome P450 [CYP] system) are not usually expected and explicitly studied during mAbs clinical development [29, 28], as metabolizing enzymes are not presumed to be involved in mAb elimination [35]. In several specifically designed clinical trials, no relevant influence of mAbs on metabolism of co-medication has been shown; however, some exceptions have been reported [29]. Furthermore, other interaction mechanisms are possible and have been observed [21].
mAbs are currently being successfully developed for indications where patients use a number of concurrent medications, hence a more routine investigation of the PK DDI potential of any new therapeutic mAb, especially when co-administered with small-molecule drugs, is necessary [35]. DDIs involving mAbs are raising growing interest and concern [23]; some interactions are now used intentionally to improve mAb pharmacological effects [20].
DDIs where the mAb is the perpetrator and the small molecule is the victim are rarely reported [36]. For instance, mAbs may induce changes in cytokine levels, indirectly inducing CYP3A4 inhibition.
More frequently, DDIs where the mAb is the victim and the small molecule is the perpetrator are observed. Small molecules might modulate the activity between the mAb and the Fcγ-receptors or might affect the level of Fcγ-receptor expression. PD interactions may also occur, when small molecules coadministration influences target mediated clearance, by reducing target cells or target-bearing cells [20, 36] (as shown in Chapter 6).

2.5 Monoclonal antibodies in oncology

In cancer scientific research, mAbs are developed not only to target a particular tissue but also tumor cells within tissues [31]. mAbs are widely used in experimental studies either naked or with radioactive material or other drugs attached. Since they affect the immune system, they are also called immunotherapeutics as opposed to chemotherapeutics, which are drugs that interfere cancer cell growth [26]. The employment of classical therapeutic modalities such as chemotherapy, surgery, and radiation, often leads to severe side effects. Immunotherapy as a fourth modality of cancer therapy has already been developed and proven to be quite effective. In oncology, a combination of therapeutic modalities, together with combinations of multiple drug regimens, is usually required. Hence, in this therapeutic area, it is particularly important to investigate potentially significant DDIs between mAbs and small-molecule drugs, to identify and document any significant clinical impact [35] (see Section 2.4.5).
The first (naked) mAb used as cancer immunotherapy was rituximab. It is a chimeric IgG-1 mAb directed against CD20, which is a transmembrane protein on mature B-lymphocytes [26]. It is indicated for B-cell non-Hodgkin's Lymphoma (NHL) and CLL; over 90% of lymphoma B cells are CD20 positive [31]. Rituximab is the therapeutic protein whose PK DDI model is developed in Chapter 6, for CLL patients co-administered with either an anticancer small molecule drug or a placebo.
The specific mechanisms of action of therapeutic antibodies in cancer treatment can be various. For instance, mAbs can: (i) bind to cell-surface proteins leading to the destruction of cancer cell, (ii) interfere with the growth and differentiation of malignant cells, (iii) transport anticancer agents (radioactive materials or other drugs) on malignant cells via antigen binding [26, 27].
Antibody distribution in tumor tissue is very heterogeneous. Diffusion

to the tumour may be impaired because of elevated ISF pressure and thhe creation of a binding-site barrier (see Section 2.4.2). The problem of poor and heterogenous tumor penetration can be addressed choosing the appropriate dosing regimen. Indeed, fractionated doses, instead of a single large one, can provide a decrease in tumor size, leading to improvements and changes in blood flow and reductions in interstitial pressure. In this way, subsequent doses can access regions different from those accessed earlier [29]. Patient biological and clinical status together with antitumor response were also reported to influence mAb PK in cancer treatment [37, 38, 39, 40]: PK and PD processes are interdependent [31]. Despite the wealth of information available in immunology literature, little work has been done to incorporate such knowledge into mechanistic PK-PD models, describing mechanisms like (i), (ii) or (iii) [27], necessary to understand the interdependence between mAb PK and PD in cancer treatment.

Chapter 3

PK and TMDD modeling for mAbs: state of the art

Population PK modeling and simulation have been used in the clinical evaluation of most mAbs. The population approach should be preferred over individual data analysis in order to develop predictive models, to take into account individual covariates (e.g. demographic predictors, genotypes and disease status), to find sources of variability, and to guide the selection of appropriate dosing regimens [29, 31]. A brief review of the model types proposed for mAb PK is now presented.

3.1 Empirical compartmental models

Most population PK analyses have reported a two-compartmental model, with the volume of the central compartment being approximately similar to the plasma volume (3 L), linear distribution to the peripheral compartment, and elimination from the central compartment. The central compartment usually corresponds to blood or

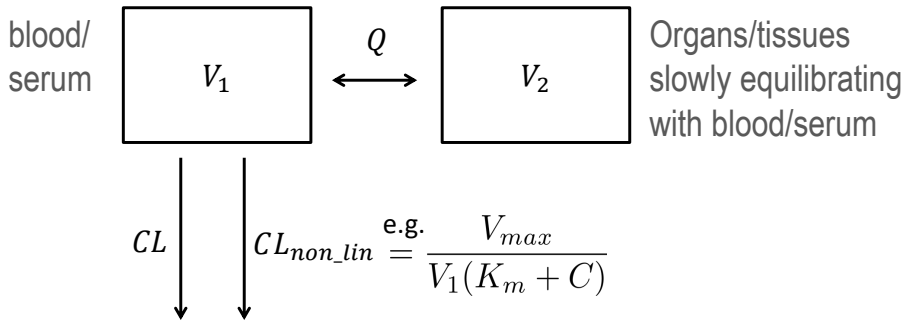

Figure 3.1: Representation of the most common empirical PK model for mAbs. V_1 and V_2 are apparent distribution volumes in central and peripheral compartments, respectively, while Q is intercompartmental clearance. CL represents the linear elimination term, while CL_{non_lin}, expressed via an MM equation, is the nonlinear elimination term.

serum, whereas the peripheral compartment to organs or tissues slowly equilibrating with blood or serum [31] (Figure 3.1).

Elimination has been reported to be linear for some mAbs, but nonlinear for others: this might be explained by differences in target affinity, tissue distribution, or the range of achieved plasma/tissue concentrations. The most popular choice for describing nonlinear elimination is a Michaelis-Menten (MM) function of the drug concentration [41] (see Figure 3.1), representing the saturable process of drug associating with and dissociating from the target and, in parallel, the degradation of the drug-target complex.

Even when including nonlinear elimination from the central compartment, these empirical models may be limited because they assume that distribution is a first-order process and that the central compartment is in equilibrium with the site of elimination. For mAbs these assumptions are likely not to be verified: distribution may have a nonlinear

and saturable component as well, and furthermore non-negligible clearance may occur in peripheral compartments [31]. For several mAbs, more mechanistic models have been applied that incorporate antigen binding and target mediated elimination [29].

3.2 TMDD models

TMDD represents one specific source of nonlinear kinetics, where drug-target binding and subsequent events (complex dissociation and degradation) result in dose-dependent changes in overall distribution and/or elimination parameters [4]. TMDD occurs with many mAbs [42, 41]; in some cases, TMDD-related nonlinearity may not be observed in experimental data, because the clinical doses administered often saturate this clearance pathway [41]. When observed, non-linear kinetics due to TMDD has significant impact on dose selection, dosing scheme, and sampling times. A mechanistic TMDD characterization can provide information on the target and on its interaction with the drug [42, 41].

3.2.1 Mechanistic full TMDD model

Mager and Jusko proposed a mechanistically-grounded model for TMDD description, whose key feature is that saturable, high-affinity binding of the drug to its pharmacologic target is responsible for PK nonlinearity [4]. According to this model (Figure 3.2), drug-target binding is assumed to occur only in the central compartment. In particular, drug in the central compartment binds to free antigens to form a drug-target complex. When there is no external drug input, the endogenous free target is synthesized in a zero-order process and degraded in a first-order process. The drug elimination pathway via

binding to the target and subsequent degradation of the complex could be saturated, when the target amount or capacity is limited [41]. The total binding capacity imparts nonlinearity in distribution and sometimes in elimination. Once formed, the complex may dissociate or, in the case of target mediated endocytosis, undergo internalization and degradation. Unbound drug can also be directly eliminated or be subjected to non-specific tissue binding or distribution [4]. A depot compartment may also be included to represent s.c. or i.m. administration sites. Variations to the full TMDD model exist: for instance, it has been suggested that a general TMDD model with drug-target binding in the peripheral compartment could be more relevant, since the disease-related target sites often reside in tissues [41].

Thanks to its mechanistic base, the model proposed in [4] is flexible, as specific aspects may be included or excluded depending on the pharmacology of the system. For example, when the drug-target complex does not internalize or degrade, the corresponding rate constant may be removed from the model.

Although its a priori identifiability has been demonstrated [43], this model displays practical identifiability issues. Indeed, it was noticed that the identification of the TMDD model parameters from the PK data alone can be difficult, especially with relatively sparse clinical data, and/or if only the drug concentration (free or total) is measured. The concentrations of the target or the drug-target complex are routinely unavailable because of assay constraints, and, when available, may not be sufficient to describe the initial binding process, making the general TMDD model in [4] over-parameterized [41]. Another reason for the non-identifiability of the parameters from the PK data is the large difference between the drug-target binding process, with the characteristic half-life of minutes or hours, and the elimination of the free drug, with the characteristic half-life of days or weeks [44]. Furthermore, the nonlinear differential equations make the theoretical analysis and numerical implementation of the TMDD model more diffi-

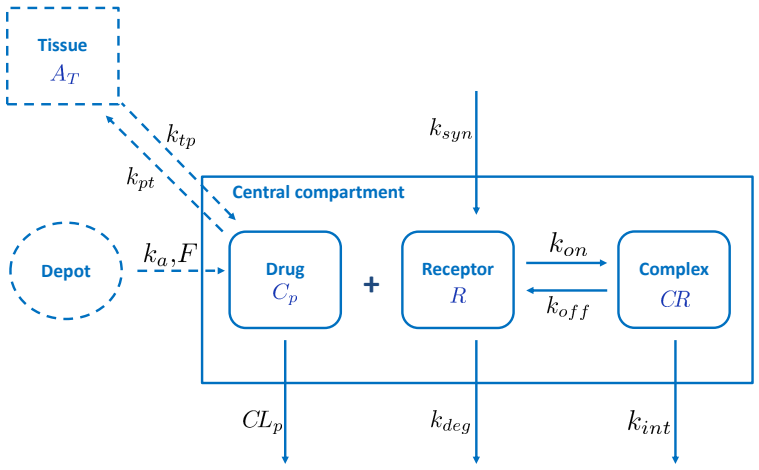

$$\frac{dC_p}{dt} = In(t) - k_{on} R\, C_p + k_{off} CR - \frac{CL_p}{V_p} C_p - k_{pt} C_p + k_{tp} \frac{A_T}{V_p}$$
$$\frac{dR}{dt} = k_{syn} - k_{on} R\, C_p + k_{off} CR - k_{deg} R$$
$$\frac{dCR}{dt} = k_{on} R\, C_p - (k_{off} + k_{int}) CR$$
$$\frac{dA_T}{dt} = k_{pt} C_p V_p - k_{tp} A_T$$

Figure 3.2: The general TMDD model proposed in [4]. In the central compartment, the drug (with concentration C_p) may bind to free receptors (with concentration R) with constant rate k_{on}, forming drug-receptor complex (with concentration CR), or be directly eliminated with clearance CL_p. Free receptors, without drug, are synthetized with 0^{th}-order constant rate k_{syn} and degraded with 1^{st}-order rate constant k_{deg}. The complex can dissociate (rate constant k_{off}), or undergo internalization (rate constant k_{int}). A peripheral compartment (with amount A_T) can be used to consider unbound drug distribution to and from other tissues (with rate constants k_{pt} and k_{tp}); a depot compartment can be included for non-IV administration (with absportion rate k_a and bioavailability F).

cult to handle, especially in a population approach context; moreover, model convergence and parameter estimation are sensitive to initial values needed in running nonlinear model-fitting algorithms [41]. Some model simplifications and a number of model variants have therefore been proposed and discussed [4, 41, 44].

3.2.2 TMDD model approximations

A direct simplification could be to assume the total binding capacity to be constant, as suggested in [4, 41]: this holds when the degradation rates of the complex and free target can be assumed to be the same. The assumption is also convenient if data on the total target are sparse or unavailable, but the amount is considered to remain constant during mAb administration. If this does not hold, other attempts can be made by modifying or deriving some differential or algebraic equations with assumptions such as QE and QSS. Setting total binding capacity to constant is, however, an independent way of simplification and can be attempted for all models [41]. As mentioned before, the model reported in [4], also called "full TMDD model", as it has no simplifications, easily becomes over-parameterized and poorly identifiable.
To overcome this difficulty, the QE approximation of the full TMDD model was developed [45]. The main assumption used to derive the QE approximation is that the free drug, the target and the complex are at QE. This means that drug-target association and dissociation processes are much faster than the other processes described by the TMDD model (drug distribution, and elimination of target, drug and complex) [45, 44]. Hence, the QE model is applicable in the situation when the association and dissociation rates are high compared to the other rate constants, and the relationship between concentrations of the free drug, the free target and the drug-target complex is at any time determined by the equilibrium dissociation constant k_D. When

the rate of elimination of the complex is not negligible compared to the dissociation rate, the QE condition may not hold [44].
An alternative to the QE assumption is represented by a QSS condition on the drug-target complex. When complex concentration is at QSS, drug-target association is assumed to be faster than drug dissociation and all other modeled processes [46]. The QSS condition appears to imply that the derivative of the drug-target complex over time is equal to zero: in fact, it is not zero, but most of the time it is negligibly small compared to the rates of the other processes. This situation could be applicable, in particular, to a drug with fast drug-target association and dissociation, and also fast internalization of the drug-target complex. When assuming the suggested QSS condition (i.e. when using the so-called "QSS TMDD model"), the number of parameters in the model is reduced: the drug-target association and dissociation constants, k_{on} and k_{off}, are substituted by k_{ss}, equal to $(k_{off} + k_{int})/k_{on}$, where k_{int} is the internalization rate constant of the drug-target complex. The QE approximation can be considered to be a particular case of the QSS approximation when the internalization rate constant k_{int} is much smaller than the dissociation rate constant k_{off} (hence $k_D \sim k_{ss}$) [44]. There is an important difference between the QSS constant k_{ss} and the dissociation constant k_D. The dissociation constant is a measure of affinity between the drug and the target, and can be obtained in in-vitro experiments. On the contrary, k_{ss} includes also the elimination rate constant of the drug-target complex that can only be obtained in-vivo.
Equations of the QSS model can be re-parametrized in order to obtain a formulation similar to that observed for describing MM elimination, with parameters V_{max} and K_m. The difference from the standard MM equation is that V_{max} is allowed to vary over time, as it is dependent from total target concentration [44]. Obviously, as for the QSS model, also the parameters of the MM model are a combination of the parameters of the full TMDD model. The MM approximation may be

used to describe systems and dosing regimens that result in the fully saturated target, e.g. because drug concentrations significantly exceed the total target concentration [44].
The development of QE and QSS TMDD models is based on the separation of the microscopic time-scales (usually seconds to minutes), related to antibody-target binding, and macroscopic time-scales (usually hours to days), related to antibody-target complex elimination process. In [42], besides investigating the above mentioned QSS assumption on antibody-target complex, also two other approximations were explored:

- QSS for target concentration, i.e. target zero-order synthesis is considered to be balanced by target first-order elimination and by antibody-target association and dissociation processes.

- QSS for antibody concentration at target site, i.e. the net amount of antibody binding to the target is balanced by the amount entering the target site; this can be the case when the target is not easily accessible for the drug.

Other simplifications of the full TMDD model, based on QSS or other assumptions, are explored in [41]. There, furthermore, the importance of selecting the right approximation for the data at hand is underlined and some considerations for guiding this choice are suggested.
In summary, TMDD is not easy to characterize, especially when information on the target is poor. Appropriate data are required, coming from adequately designed studies; unfortunately, this is not always the case [41]. Therefore, care should be taken so that the most appropriate and parsimonious model is applied [4]. Furthermore, it should be taken into account that all the TMDD models presented in this section assume that binding occurs in plasma or tissues rapidly equilibrating with plasma; in some cases this assumption might not hold.

3.3 Minimal physiologically based model

PBPK models, initially developed for describing small molecule PK, from the mid 80s were extended to large molecules [47, 48]; a PBPK platform for mAbs was built, based on extensive literature data, able to predict the PK concentration in plasma and tissues in different species utilizing a limited number of parameters of the compound to be studied [2]. As in general the validation of a novel PBPK model may require a substantial amount of information, in the presence of limited data, and for reducing model complexity, techniques that lump tissues with similar kinetic characteristics were proposed, both for small [24, 49, 25, 50] and large molecules [3, 51, 52]. In particular, in [3] the mAb PBPK model [2, 53] was reduced into a mPBPK model. When only plasma (or blood) data are available, a mPBPK model offers a simpler approach than PBPK models, but provides parameters with more practical value than empirical compartmental models. Furthermore, in mPBPK models system- and drug-specific parameters are separated, and can be compared among congeneric drugs and across species. Additionally, as with PBPK models, the mPBPK models have the flexibility in handling different clearance sites and various mechanisms of elimination and absorption.
The mPBPK model proposed for mAbs in [3] considers specific PK characteristics of these drugs, such as poor transcapillary and cellular permeability, less renal filtration and hepatic metabolism, possible clearance from peripheral tissues, and nonlinearity due to receptor binding. Separate compartments for plasma, lymph, and ISF (considered as the only extravascular distribution space) in two types of tissues are defined. Tissues are discerned into tight and leaky, based on their vascular endothelium structures. Tight tissues have continuous capillaries; muscle, skin, adipose and brain have been assigned to this class. Leaky tissues have discontinuous (or fenestrated) capillaries, and they include all other tissues, e.g., liver, kidney, and heart

[3]. The model is represented in Figure 3.3: the drug enters in plasma, and its distribution to tight and leaky tissues depends on their vascular reflection coefficients. Through the tissues, the drug arrives in the lymph, in a manner dependent on lymphatic capillary reflection coefficient. From here, the drug goes back to plasma, where it can be eliminated; clearance pathways from the tissues could also be considered.

3.3.1 Integration with TMDD

The mechanistic description of TMDD, either in plasma or in tissue, was subsequently incorporated in the mPBPK model [6, 54, 55], leading to the so-called "mPBPK-TMDD" models. Incorporating TMDD into a mPBPK model allows to consider target binding consistently with target-expressing tissues, which is important to obtain reliable characterizations of the target profile and of drug-target binding. The feasibility of mPBPK-TMDD integration was firstly explored in [54]: the authors proposed mPBPK-TMDD models exploiting either the full or QSS TMDD model, with binding occurring either in plasma or ISF. These models were applied in a number of case studies and identified based only on plasmatic drug concentration measurements.
In the next chapter (Chapter 4), four integrated mPBPK-TMDD models are thoroughly detailed and explored, under the assumption that target sites are located in leaky tissues, with particular attention to the case when limited data are available.

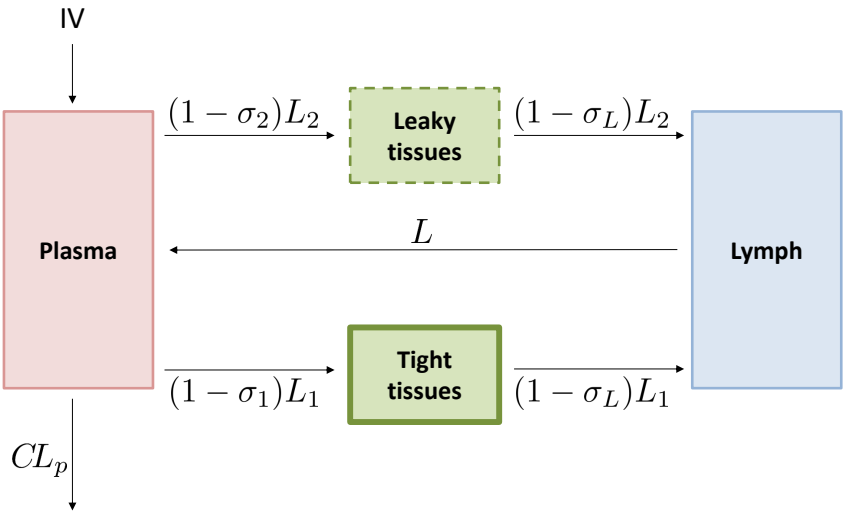

Figure 3.3: Scheme of the mPBPK model for mAbs proposed in [3], supposing IV administration and elimination from the plasmatic compartment. Plasma is represented in red, lymph in lightblue, tight tissues in green with marked outline, and leaky tissues in green with dashed outline. Vascular reflections are σ_1 and σ_2 respectively for tight and leaky tissues, with $\sigma_1 > \sigma_2$. Lymphatic capillary reflection coefficient is instead represented by σ_L. L, i.e. total lymph flow, is equal to the sum of L_1 and L_2, which are lymph flow for tight and leaky tissues, respectively. Drug clearance from plasma is denoted with CL_p.

Chapter 4

Integrated minimal PBPK-TMDD models: comparison and identifiability issues

In this chapter, a thorough feasibility assessment of the mPBPK-TMDD incorporation for describing mAb PK is proposed, considering binding occurring only in leaky tissues (a similar methodology can be applied with binding occurring in tight tissues, or in both leaky and tight tissues). In the following, four mPBPK-TMDD models are introduced: the full one (Section 4.1, see [54] and related Supplementary Material), and three different approximated models including QSS conditions on TMDD dynamics [42] (Section 4.2). The impact of such approximations is comparatively assessed through simulations of plasma and tissue concentration profiles with reference to the full mPBPK-TMDD model (Section 4.3). A sensitivity test is also per-

formed on meaningful parameters. Furthermore, identifiability of the full and approximated models is investigated, with respect to both data richness and sampling design optimization; both a priori and a posteriori identifiability issues are explored (Section 4.4). A discussion of the results of this chapter is finally reported (Section 4.5).

4.1 The full mPBPK-TMDD model

The full mPBPK-TMDD model is built incorporating the so-called full TMDD model [4, 41, 44] into the mPBPK model for mAbs (see Supplementary Material of [54]), supposing that the binding occurs in the leaky tissue. The differential equations of such model (see Figure 4.1) are:

$$
\begin{aligned}
C_p &= A_p/V_p \\
\frac{dA_p}{dt} &= In(t) + C_{lymph}L - C_pL_1(1-\sigma_1) - C_pL_2(1-\sigma_2) \\
&\quad -C_pCL_p \\
\frac{dC_{tight}}{dt} &= \frac{1}{V_{tight}}\left[L_1(1-\sigma_1)C_p - L_1(1-\sigma_L)C_{tight}\right] \\
\frac{dC_{leaky_{free}}}{dt} &= \frac{1}{V_{leaky}}\left[L_2(1-\sigma_2)C_p - L_2(1-\sigma_L)C_{leaky_{free}}\right] \\
&\quad -k_{on}C_{leaky_{free}}R_{leaky_{free}} + k_{off}CR_{leaky} \\
\frac{dR_{leaky_{free}}}{dt} &= k_{syn} - k_{deg}R_{leaky_{free}} - k_{on}C_{leaky_{free}}R_{leaky_{free}} \\
&\quad +k_{off}CR_{leaky} \\
\frac{dCR_{leaky}}{dt} &= k_{on}C_{leaky_{free}}R_{leaky_{free}} - k_{off}CR_{leaky} - k_{int}CR_{leaky} \\
\frac{dC_{lymph}}{dt} &= \frac{1}{V_{lymph}}[L_1(1-\sigma_L)C_{tight} + L_2(1-\sigma_L)C_{leaky} \\
&\quad -C_{lymph}L]
\end{aligned}
$$

C_p and C_{lymph} are free antibody concentrations in plasma volume (V_p) and lymph volume (V_{lymph}) respectively, while C_{tight} and $C_{leaky_{free}}$ are antibody free concentrations in system ISF volume of tissues with continuous endothelium (V_{tight}) and in ISF volume of tissues with fenestrated or discontinuous endothelium (V_{leaky}), respectively. Cao and colleagues [3] have assigned the muscle, skin, adipose and brain to V_{tight}, and all other tissues to V_{leaky} (liver, kidney, heart, etc.). Free target concentration is expressed as $R_{leaky_{free}}$, while antibody-target concentration is CR_{leaky}. The total lymph flow L equals the sum of the flows for leaky tissue, L_1, and tight tissue, L_2. Vascular reflection coefficients for tight and leaky tissue are σ_1 and σ_2 (constrained to be < 1), while σ_L is the lymphatic capillary reflection coefficient. Rate constants are k_{syn} for target biosynthesis, k_{deg} for target degradation, k_{int} for antibody-target complex internalization, k_{on} for antibody-receptor association and k_{off} for antibody-receptor dissociation. Finally, CL_p is clearance from plasma. All initial conditions of the differential equations are set to zero, except for $R_{leaky_{free}}(0) = k_{syn}/k_{deg}$.
Other simplified TMDD descriptions can be incorporated into the mPBPK model, as shown in the next section.

4.2 Other three mPBPK-TMDD models: QSS approximations

The QSS approximation proposed by Gibiansky et al [44], and the two additional QSS conditions proposed by Grimm [42] (see Chapter 3, Section 3.2) can be applied to the TMDD model incorporated in the leaky tissue compartment of the mPBPK model. Hence, in particular, the following QSS approximations were considered:

- on antibody-target complex concentration in binding tissue, assuming that the right-hand side of the differential equation for

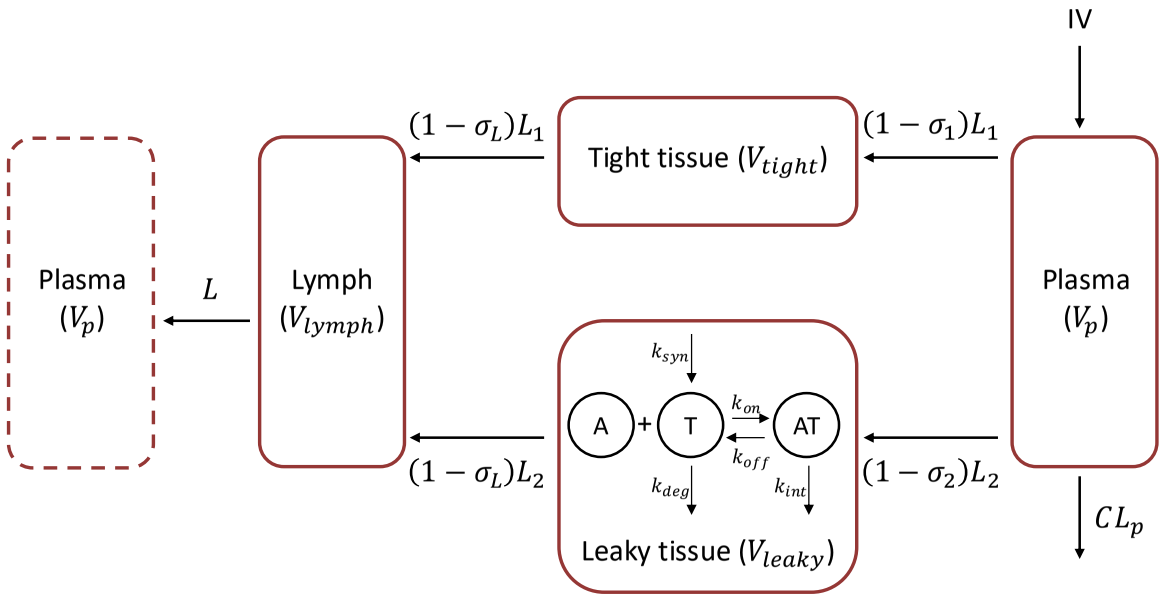

Figure 4.1: Representation of the full mPBPK-TMDD model with binding in the leaky tissue. A and T represent, respectively, antibody and target.

the complex (CR_{leaky}) equals zero:

$$k_{int}CR_{leaky} = k_{on}C_{leaky_{free}}R_{leaky_{free}} - k_{off}CR_{leaky} \tag{4.1}$$

- on free target concentration in binding tissue, assuming that target zero-order synthesis (k_{syn}) is balanced by first-order elimination (k_{deg}), and antibody-target complex association (k_{on}) and dissociation (k_{off}):

$$k_{syn} - k_{deg}R_{leaky_{free}} = k_{on}C_{leaky_{free}}R_{leaky_{free}} - k_{off}CR_{leaky} \tag{4.2}$$

- on free antibody concentration in binding tissue, assuming that the net amount of antibody binding to the target must be balanced by the amount entering the target site (here, the leaky tissue):

$$\begin{aligned} &C_pL_2(1-\sigma_2) - C_{leaky_{free}}L_2(1-\sigma_L) = \\ &(k_{on}C_{leaky_{free}}R_{leaky_{free}} - k_{off}CR_{leaky})V_{leaky} \end{aligned} \tag{4.3}$$

Note that, by virtue of the adoption of a QSS approximation, the differential equation for the variable at QSS is replaced by an algebraic one.

4.2.1 Model A

A mPBPK model with a TMDD component including the approximation on antibody-target complex concentration (Equation 4.1) and expressed in terms of total drug concentration in the leaky tissue ($C_{leaky_{total}} = C_{leaky_{free}} + CR_{leaky}$) and total target concentration in the leaky tissue ($R_{leaky_{total}} = R_{leaky_{free}} + CR_{leaky}$) was already considered

in [54]:

$$
\begin{aligned}
C_p &= A_p/V_p \\
\frac{dA_p}{dt} &= In(t) + C_{lymph}L - C_pL1(1-\sigma_1) - C_pL_2(1-\sigma_2) \\
&\quad -C_pCL_p \\
\frac{dC_{tight}}{dt} &= \frac{1}{V_{tight}}\left[L_1(1-\sigma_1)C_p - L_1(1-\sigma_L)C_{tight}\right] \\
\frac{dC_{leaky_{total}}}{dt} &= \frac{1}{V_{leaky}}\left[L_2(1-\sigma_2)C_p - L_2(1-\sigma_L)C_{leaky_{free}}\right] \\
&\quad -k_{int}CR_{leaky} \\
\frac{dR_{leaky_{total}}}{dt} &= k_{syn} - k_{deg}R_{leaky_{free}} - k_{int}CR_{leaky} \\
\frac{dC_{lymph}}{dt} &= \frac{1}{V_{lymph}}\left[L_1(1-\sigma_L)C_{tight} + L_2(1-\sigma_L)C_{leaky_{free}}\right. \\
&\quad \left.-C_{lymph}L\right]
\end{aligned}
\tag{4.4}
$$

where $C_{leaky_{free}}$ and CR_{leaky} are computed as:

$$
\begin{aligned}
C_{leaky_{free}} &= \frac{1}{2}(C_{leaky_{total}} - R_{leaky_{total}} - k_{ss} \\
&\quad +\sqrt{(C_{leaky_{total}} - R_{leaky_{total}} - k_{ss})^2 + 4k_{ss}C_{leaky_{total}}}) \\
CR_{leaky} &= \frac{R_{leaky_{total}}C_{leaky_{free}}}{k_{ss} + C_{leaky_{free}}}
\end{aligned}
\tag{4.5}
$$

Adding this QSS simplification, the model is reduced by one parameter: instead of the association and dissociation constants (k_{on} and k_{off}), the QSS constant $k_{ss} = (k_{int} + k_{off})/k_{on}$ is introduced. In this work, the mPBPK-TMDD model described by Equations 4.4 and 4.5 is referred to as model A.

4.2.2 Model B

If also the approximation on target concentration in leaky tissue (Equation 4.2) is added, model B is obtained:

$$\begin{aligned}
C_p &= A_p/V_p \\
\frac{dA_p}{dt} &= In(t) + C_{lymph}L - C_pL1(1-\sigma_1) - C_pL_2(1-\sigma_2) \\
&\quad -C_pCL_p \\
\frac{dC_{tight}}{dt} &= \frac{1}{V_{tight}}\left[L_1(1-\sigma_1)C_p - L_1(1-\sigma_L)C_{tight}\right] \\
\frac{dC_{leaky_{total}}}{dt} &= \frac{1}{V_{leaky}}\left[L_2(1-\sigma_2)C_p - L_2(1-\sigma_L)C_{leaky_{free}}\right] \\
&\quad -k_{int}CR_{leaky} \\
\frac{dC_{lymph}}{dt} &= \frac{1}{V_{lymph}}\left[L_1(1-\sigma_L)C_{tight} + L_2(1-\sigma_L)C_{leaky_{free}}\right. \\
&\quad \left.-C_{lymph}L\right]
\end{aligned} \tag{4.6}$$

where:

$$\begin{aligned}
\alpha &= k_{int} \\
\beta &= k_{ss}k_{deg} - k_{int}C_{leaky_{total}} + k_{syn} \\
\gamma &= -k_{ss}k_{deg}C_{leaky_{total}} \\
C_{leaky_{free}} &= \frac{1}{2\alpha}\left(-\beta + \sqrt{\beta^2 - 4\alpha\gamma}\right) \\
R_{leaky_{free}} &= \frac{k_{syn}k_{ss}}{(k_{ss}k_{deg} + k_{int}C_{leaky_{free}})} \\
CR_{leaky} &= \frac{R_{leaky_{free}}C_{leaky_{free}}}{k_{ss}}
\end{aligned} \tag{4.7}$$

This time, no reduction of the model in terms of number of parameters is achieved.

4.2.3 Model C

Finally, adding the approximation on free antibody concentration in leaky tissue (Equation 4.3), model C is:

$$\begin{aligned}
C_p &= A_p/V_p \\
\frac{dA_p}{dt} &= In(t) + C_{lymph}L - C_pL_1(1-\sigma_1) - C_pL_2(1-\sigma_2) \\
&\quad -C_pCL_p \\
\frac{dC_{tight}}{dt} &= \frac{1}{V_{tight}}\left[C_pL_1(1-\sigma_1) - L_1(1-\sigma_L)C_{tight}\right] \\
\frac{dC_{lymph}}{dt} &= \frac{1}{V_{lymph}}\left[L_1(1-\sigma_L)C_{tight} + L_2(1-\sigma_L)C_{leaky_{free}}\right. \\
&\quad \left.-C_{lymph}L\right]
\end{aligned}$$

where $C_{leaky_{free}}$, $R_{leaky_{free}}$ and CR_{leaky} are obtained as:

$$\begin{aligned}
\alpha &= -k_{int}L_2(1-\sigma_L) \\
\beta &= k_{int}C_pL_2(1-\sigma_2) - k_{ss}k_{deg}L_2(1-\sigma_L) - k_{int}V_{leaky}k_{syn} \\
\gamma &= k_{ss}k_{deg}C_pL_2(1-\sigma_2) \\
C_{leaky_{free}} &= \frac{1}{2\alpha}(-\beta - \sqrt{\beta^2 - 4\alpha\gamma}) \\
R_{leaky_{free}} &= \frac{k_{syn}k_{ss}}{(k_{ss}k_{deg} + k_{int}C_{leaky_{free}})} \\
CR_{leaky} &= \frac{R_{leaky_{free}}C_{leaky_{free}}}{k_{ss}}
\end{aligned}$$

Again, the number of model parameters does not decrease.
In the next sections, a detailed assessment of the four mPBPK-TMDD models (full, A, B, C) is illustrated.

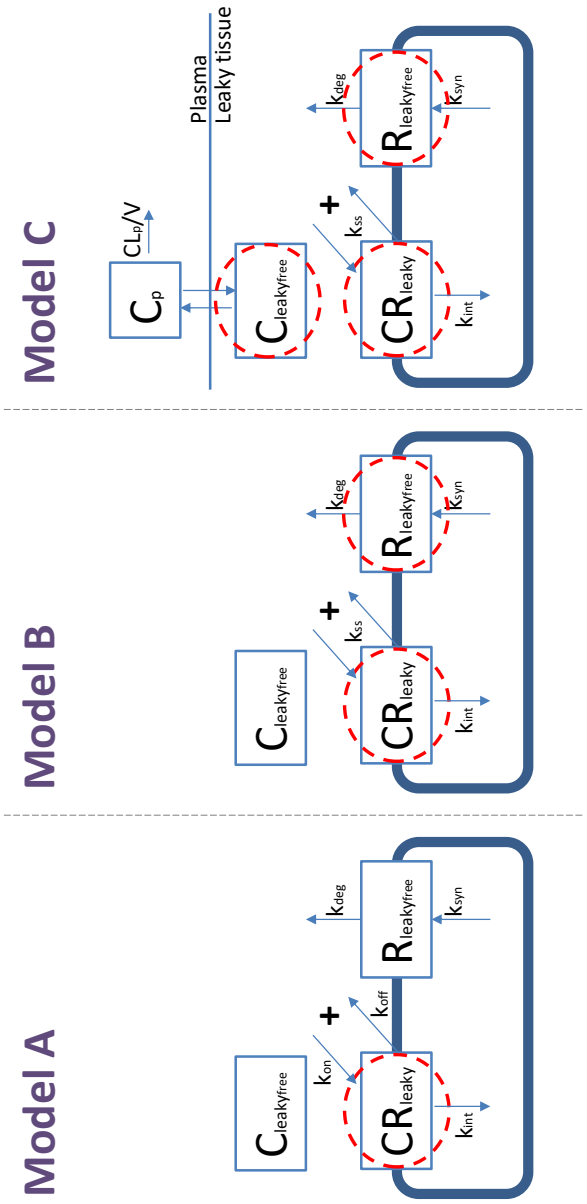

Figure 4.2: Structure of models A (left panel), B (central panel) and C (right panel) obtained adding progressively the QSS approximations on antibody-target complex, free target and free antibody in leaky tissue as described respectively by Equations 4.1, 4.2 and 4.3. The red dashed circles indicate the variable at QSS [6].

4.3 A simulated study: comparison of the four models and sensitivity test

A simulated study of the four models presented above (Figures 4.1 and 4.2) was carried out with the software for statistical computing and graphics R (version 3.1.2, `https://cran.r-project.org/`), using the deSolve package for solving the differential equations systems. First of all, taking as a reference the full model (as it does not make simplifying assumptions), the four models were simulated and compared. The aim was to see what changes are entailed by the addition of the steady-state approximations, both in terms of antibody and target concentrations.

4.3.1 Simulations settings and results

Simulation of the four models was performed using mPBPK and TMDD model parameters estimated in [54] for the case study of romosozumab [56] assuming: a) a plausible value of the dissociation constant k_D equal to 0.963 nM ($k_D = k_{off}/k_{on}$, see Supplementary Material of [56]); b) a body weight of 70 kg in order to derive CL_p in L/hr (see Table 4.1). The remaining required values, L_1, L_2, V_{tight}, and V_{leaky}, are derived with the following assumptions:

$$
\begin{aligned}
L_1 &= 0.33\, L \\
L_2 &= 0.67\, L \\
V_{tight} &= 0.65\, ISF\, K_p \\
V_{leaky} &= 0.35\, ISF\, K_p
\end{aligned}
$$

where $ISF = 15.6$ L is the total ISF volume for a 70 kg body weight person, 0.33 and 0.67 are the relative fractions to L of L_1 and L_2 respectively, 0.65 and 0.35 are the relative fractions to available total ISF

Table 4.1: Model parameters for mPBPK-TMDD simulations.

	value	unit
V_p	2.6	L
V_{lymph}	5.2	L
L	2.9/24	L/hr
σ_L	0.2	−
σ_1	0.99	−
σ_2	0.712	−
CL_p	0.896	10^{-2}L/hr
k_{ss}	1.31	nM
k_{syn}	0.172	nM/hr
k_{deg}	1.21	10^{-2}/hr
k_{int}	0.624	10^{-2}/hr
k_D	0.963	nM
k_{on}	0.018	1/nM/hr
k_{off}	0.017	1/hr

of V_{tight} and V_{leaky} respectively [2, 53], and $K_p = 0.8$ is the available fraction of ISF for antibody distribution [54]. Simulations were performed at the same dose levels of the case study reported in [56], which were administered intravenously: one low, 1 mg/kg, and one high, 5 mg/kg. At low doses the mechanism of target mediated drug disposition significantly contributes to the overall clearance, while at higher doses, when the target is saturated, the overall clearance is mainly governed by the typical catabolism process for mAbs (i.e. CL_p).
In the simulations, one virtual 70 kg body weight subject was considered per each dose level, with samples simulated every 5 hours up to 84 days. The input dose per subject expressed in nM was obtained via the following formula: $10^3(doseBW)/MW$, where $dose$ represents the dose in mg/kg, BW is the body weight (i.e., 70 kg), and MW is

the MW of the mAb, here assumed to be equal to 150 kDa.
It was found that model A generates the closest profiles to the full mPBPK-TMDD model in plasma and target site for both compound and receptor variables, free and total. Model B deviates from the full model in free and total target concentration profiles, while model C systematically deviates from the full one for both drug and target concentrations (see Figure 4.3).

4.3.2 Sensitivity test

For all the four models, also a univariate sensitivity test on the following parameters was performed: σ_1, σ_2, CL_p, k_{ss}, k_{int} and k_D, in order to study their influence on the antibody and target concentration profiles. In particular, the sensitivity of C_p, $C_{leaky_{total}}$ and $R_{leaky_{total}}$ profiles with respect to the considered parameters is here of interest. Usually, the plasmatic concentrations of the drug (and target, when it resides in plasma) are indeed available; less frequently, measurements in tissue (e.g. total drug and target concentrations) are also collected. More in detail, a minimum and a maximum value were defined for σ_1, σ_2, CL_p, k_{ss}, k_{int} and k_D (see Table 4.2): in general, the nominal value in Table 4.1 divided and multiplied by 10, respectively. This rule was appropriately tailored for σ_1, σ_2, k_{ss}, and k_D to respect the constraints

$$
\begin{aligned}
&0 < \sigma_1, \sigma_2 < 1 \\
&\sigma_1 > \sigma_2 \\
&k_{ss} > k_D.
\end{aligned}
$$

The four models were simulated varying one parameter at a time, in order to compare the results obtained with the minimum value to the ones obtained with the maximum value.

The model parameters tested have a detectable impact at both doses (e.g. CL_p, see Figure 4.4), with similar magnitude in the four

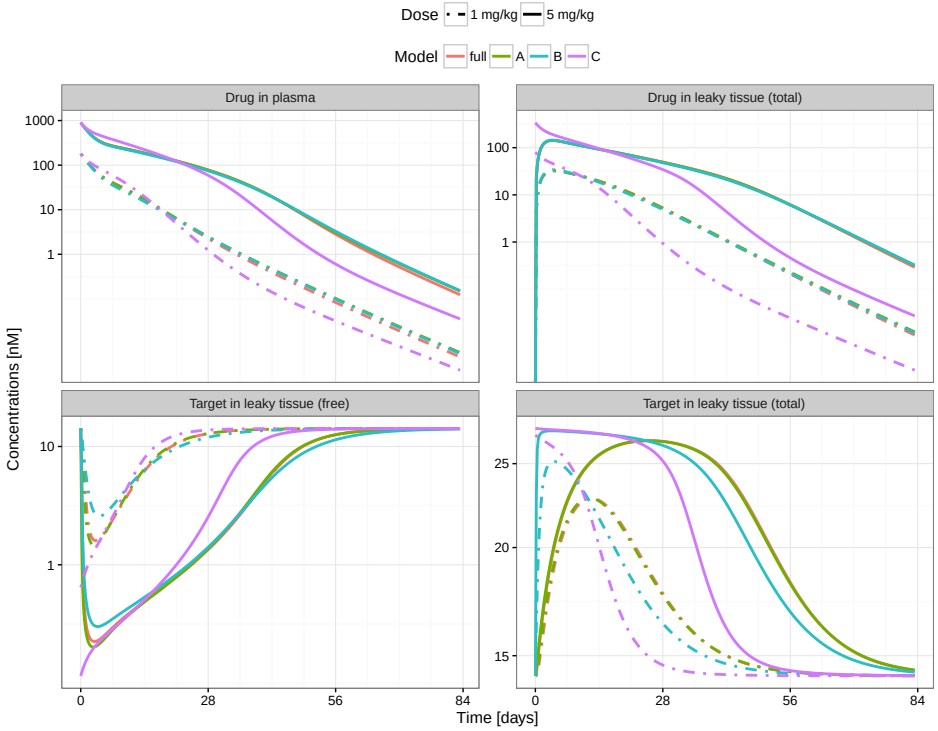

Figure 4.3: Simulations of the two IV doses, with binding in the leaky tissue with full model (Indian red) and approximations of the binding process (olive), binding process and target turnover (sea green), binding process, receptor turnover and drug concentration at the target site (orchid). Upper left panel: free drug concentration in plasma. Upper right panel: total drug concentration in leaky tissue. Lower left panel: free receptor concentration in leaky tissue. Lower right panel: total receptor concentration in leaky tissue.

Table 4.2: Parameter ranges for the sensitivity test (units as reported in Table 4.1).

	min	max
σ_1	0.715	0.99
σ_2	0.25	0.75
CL_p	0.07	7
k_{ss}	0.965	20
k_{int}	0.06/100	6/100
k_D	0.1	1.30

mPBPK-TMDD models. The only exception is the dissociation constant k_D, which, in its range of investigation, does not seem to influence significantly the three profiles of interest (see Figure 4.5), especially for the approximated mPBPK-TMDD models. The almost null influence of k_D on the simulated profiles was further investigated by perfoming another univariate sensitivity analysis, separately on k_{on} and k_{off}, only on the full model, in order to discern the effects of the two parameters. As before, minimum and maximum values were selected as ten times lower and higher than the real parameter value. As depicted in Figure 4.6, both k_{on} and k_{off} influence separately the three profiles of interest, but their sensitivity curves appear to be highly correlated: the scenario in which k_{on} is low appear almost identical to the scenario in which k_{off} is high and viceversa. This might explain why k_D, by including the effects both of k_{on} and k_{off}, has no significant influence on the simulated profiles.

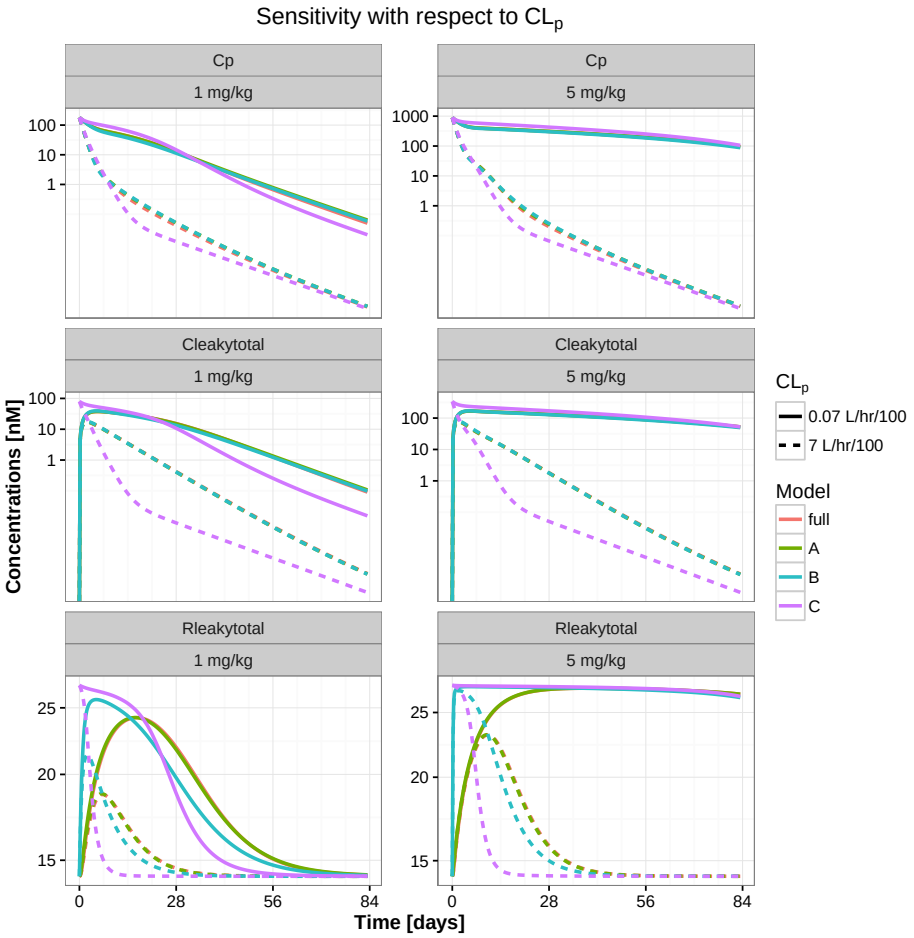

Figure 4.4: Plasma drug concentration, drug concentration in binding tissue and target amount in binding tissue obtained with the four models varying CL_p, from its minimum (dashed line) to its maximum (solid line). The dashed lines are clearly distinguishable from the solid lines, indicating a significant sensitivity of concentration profiles to CL_p values. Left panels: simulations at 1 mg/kg; right panels: simulations at 5 mg/kg.

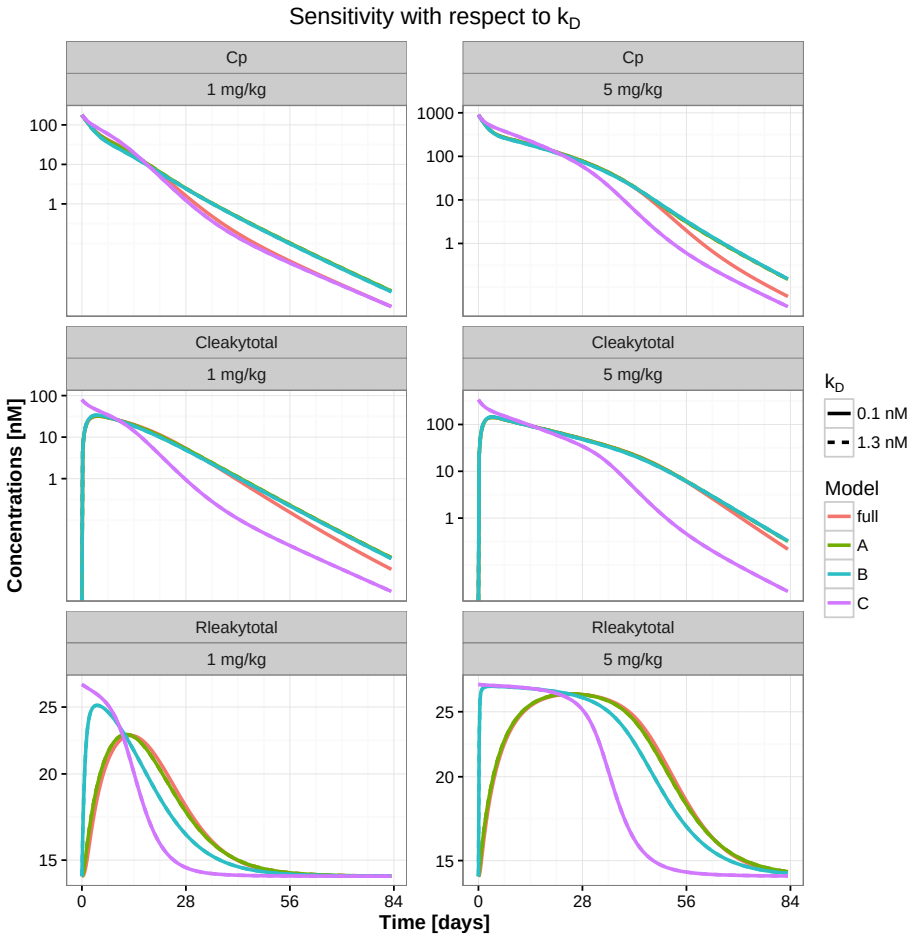

Figure 4.5: Plasma drug concentration, drug concentration in binding tissue and target amount in binding tissue obtained with the four models varying k_D, from its minimum (dashed line) to its maximum (solid line). In contrast with Figure 4.4, here the dashed lines are hardly visible because they are overlapped with solid lines, indicating that concentration profiles are not much sensitive to k_D values. Left panels: simulations at 1 mg/kg; right panels: simulations at 5 mg/kg.

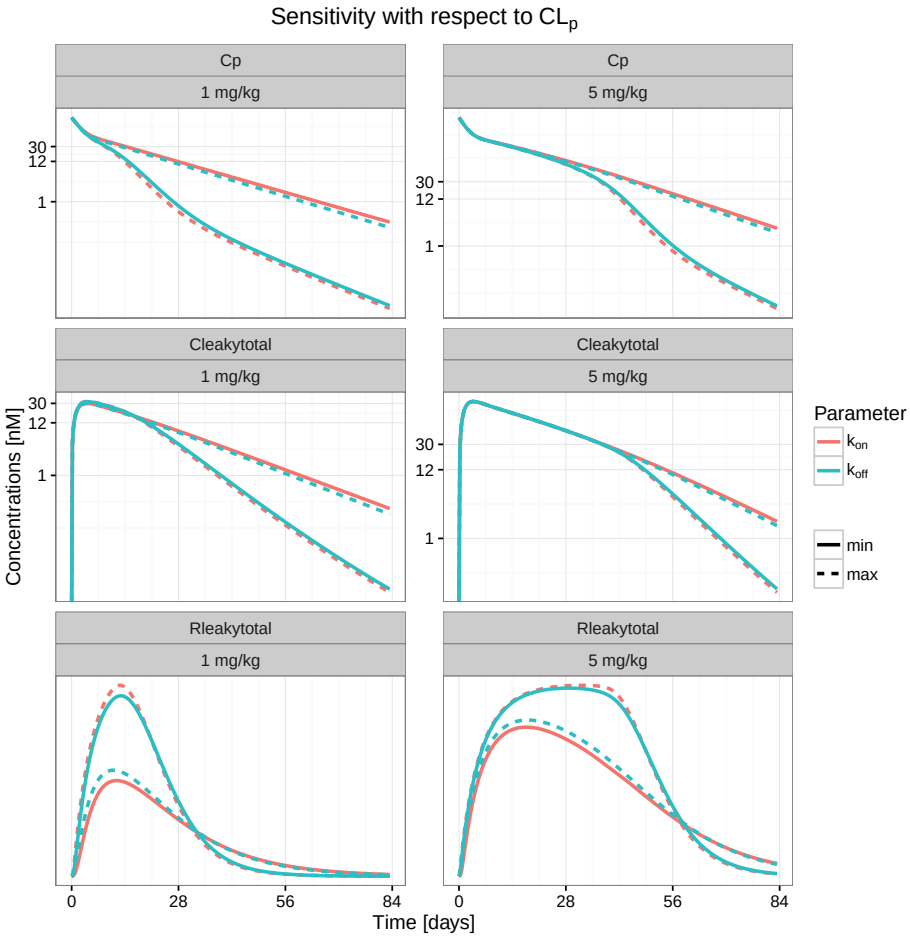

Figure 4.6: Plasma drug concentration, drug concentration in binding tissue and target amount in binding tissue obtained with the full models varying: (i) k_{on} (red lines), from its minimum, i.e. 0.0018 (dashed line), to its maximum, i.e. 0.18 (solid line), (ii) k_{off} (blue lines), from its minimum, i.e. 0.0017 (dashed line), to its maximum, i.e. 0.17 (solid line). Left panels: simulations at 1 mg/kg; right panels: simulations at 5 mg/kg.

4.4 Identifiability issues

The previous analysis suggests that not all mPBPK-TMDD models parameters influence in a detectable way the antibody and target profiles that could be measured in clinical trials: hence, in general, there may be identification issues. For this reason, the identifiability of the four models, both structural (a priori) and practical (a posteriori), was studied.
The measurements of total mAb and target concentrations in the binding tissue ($C_{leaky_{total}}$ and $R_{leaky_{total}}$, respectively) are in general quite invasive, hence only few samples may be generally available. Considering this constraint, the a priori and a posteriori identifiability of the four models was studied in three realistic scenarios, in which:

i. Only C_p is measured

ii. C_p and $C_{leaky_{total}}$ are measured

iii. C_p and $R_{leaky_{total}}$ are measured

4.4.1 A priori identifiability

A priori identifiability is a theoretical property of the model structure; it ensures that model parameters can be uniquely (globally or locally) determined from knowledge of the input-output behavior assuming perfect experimental data. Hence, the fulfillment of this property is independent of experimental design conditions. A priori identifiability is a necessary prerequisite for parameter estimation in practice. Its study is therefore important to establish whether parameter estimation difficulties are due either to the particular experimental design or the mathematical structure of the model.
For nonlinear systems, several methods are available for the testing of a priori identifiability, but methods for testing global identifiability

entail a more demanding implementation, especially for large systems [57]. An algorithm inspired by [58] for the assessment of local identifiability was proposed in [59] and implemented in the IdentifiabilityAnalysis package of the software Mathematica [59, 60]. This tool was chosen to explore the local a priori identifiability of the four mPBPK-TMDD models, in scenarios i., ii. and iii.
The Mathematica implementation takes the parametrized initial conditions, the system equations, and the set of measurable outputs, and computes a number of properties of interest, e.g. identifiability and the sets of identifiable or unidentifiable parameters [59].
Since the method implemented in the IdentiabilityAnalysis package of Mathematica requires the model system to be rational with respect to all its arguments [59], model A, B and C needed to be rationalized. However, it was not possible to complete this process for the last model because of an unremovable irrational initial condition: in this case, local a priori identifiability could not be assessed. Rationalized equations of model A and B are reported in Appendix A, Section A.1. Full Model and Model A were found to be a priori identifiable in every scenario. Model B turned out to be a priori identifiable only with the output choice iii. (see Table 4.3); in cases i. and ii. k_{deg} and k_{ss} are the non-identifiable parameters. For more details on theory and implementation, see Appendix A, Section A.1.

4.4.2 A posteriori identifiability

A posteriori identifiability refers to the ability of practically estimating an unknown parameter vector; it is inherently related to the type and amount of experimental data available. Since a priori identifiability is a necessary, yet not sufficient condition for a posteriori identifiability, the latter property was analyzed only for the cases where a priori identifiability is met. The Fisher Information Matrix (FIM) [61] can provide insight into the amount of information available in the

Table 4.3: A priori identifiability results for all models in all scenarios: "yes/no" indicate that there is/there is not a priori identifiability, while the "-" indicates that it's not possible to assess the theoretical property.

	i.	ii.	iii.
Full	yes	yes	yes
A	yes	yes	yes
B	no	no	yes
C	-	-	-

Table 4.4: Condition number of the FIM.

Scenario	Full Model	Model A	Model B
i: C_p	2.9×10^6	97.3×10^6	–
ii: C_p and $C_{leaky_{total}}$	1.0×10^6	108.0×10^6	–
iii: C_p and $R_{leaky_{total}}$	1.8×10^6	45.8×10^6	98.8×10^6

data (i.e. their quality), and a Monte Carlo (MC) procedure can be exploited for the exploration of fitting results, as far as it regards both the parameter estimates and the adherence of estimated concentration profiles on the data.
The condition number of the FIM for all a priori identifiable mPBPK-TMDD models and scenarios was computed (see Table 4.4). When the condition number is large, the matrix is close to singular or, more precisely, ill-conditioned; this entails a large uncertainty along some directions in the parameter space. The condition number results to be particularly elevated for models with QSS approximations, especially if only C_p or C_p and $C_{leaky_{total}}$ are measured. The MC procedure comprises the following steps (see Figure 4.7):

- Simulation from the Full Model of 100 datasets per each output

choice (i., ii. and iii.), using a sampling schedule mimicking the clinical practice and a proportional residual error model with coefficient of variation equal to 0.2 for C_p (CV_{C_p}) and $C_{leaky_{total}}$ ($CV_{C_{tot}}$), and 0.3 for $R_{leaky_{total}}$ ($CV_{R_{tot}}$).

- Fitting of the mPBPK-TMDD models (in NONMEM, `http://www.iconplc.com/innovation/nonmem/`) on each simulated dataset, with initial parameter values equal to the true ones with a perturbation of $\pm 15\%$.

- Examination of the distribution of parameter estimates via boxplots, and computation of outliers, sample variance, confidence intervals (CIs), bias, percent coefficient of variation (CV%) and Root Mean Square Error (RMSE). Furthermore, the parameters were ranked on the basis of an index, δ, equal to the percent RMSE with respect to the true value of the parameter.

- Exploration of fitting quality by plotting: differential equations states vs. time, Conditional Weighted Residuals (CWRES) vs. Time, CWRES vs. the dependent variable (DV) [62], and Goodness Of Fit (GOF) plots. Furthermore, Predictive Plots (PPs) are used to compare the noise-free simulated data with the percentiles of the predicted noise-free curves, computed from the 100 estimates obtained.

In particular, in the simulation step, the following sampling scheme was considered: for plasma concentration, sampling time $t \in \mathcal{T}_p = \{0, 1, 2, 3, 4, 8, 16, 24, 48, 72, 96, 120, 168, 336, 504, 672, 840, 1008, 1176, 1344, 2016\}$ (i.e. rich sampling schedule on the first day, then gradually more sparse), and for total antibody and target concentration in binding leaky tissue, $t \in \mathcal{T}_{leaky} = \{72, 336, 672, 2016\}$ (i.e. day $3, 14, 28, 84$). For more details about theory, implementation and the software tools exploited, see Appendix A, Section A.2.

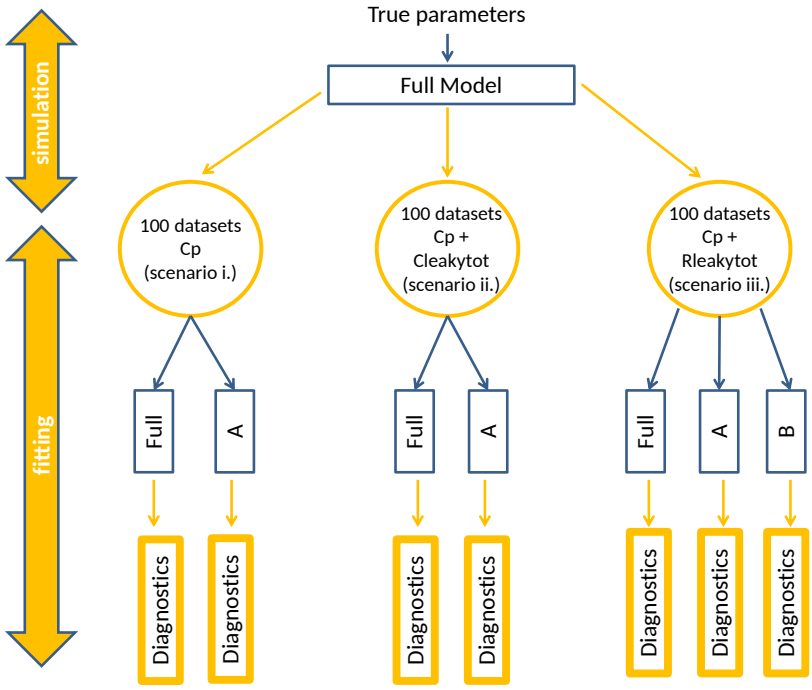

Figure 4.7: Diagram of the MC a posteriori identifiability analysis. Datasets were simulated with the Full Model and used to identify the mPBPK-TMDD models. NONMEM output tables were obtained and analysed.

Table 4.5: Parameter ranking based on δ obtained after fitting model A on drug plasmatic concentration and total drug concentration in binding tissue (scenario ii.).

	Parameter	δ%
1.	σ_1	0.5
2.	σ_2	4.8
3.	k_{int}	6.0
4.	CV_{C_p}	13.5
5.	CL_p	13.7
6.	k_{syn}	26.0
7.	$CV_{C_{tot}}$	37.3
8.	k_{ss}	84.5
9.	k_{deg}	729.9

From the results of the a posteriori identifiability analysis, it can be observed that the parameters with the maximum CV% and δ are the ones linked to the processes of binding, degradation and internalization of the complex. In Figure 4.8 the distributions of the parameter estimates are reported, for the scenario with the Full Model and plasma drug concentration as output measure (scenario i.). The ranking of the parameters based on δ allowed the quantification of the sensitivity of parameter estimates to noise in the data: it is worth noticing that, regardless of the scenario considered, the "worst" parameters are, for the Full Model, k_{on}, k_{off} and k_{deg} (with δ often exceeding 120%), and, for models A and B, k_{deg} and k_{ss} (with rank greater than 700%). In Table 4.5, an example of parameter ranking, for model A estimated on C_p and $C_{leaky_{total}}$ data, is reported (scenario ii.). A classification of the different scenarios, based on the maximum CV% obtained for the estimates (that can be computed also from fitting on real data, with unknown true parameter values), is also proposed in Table 4.6. In

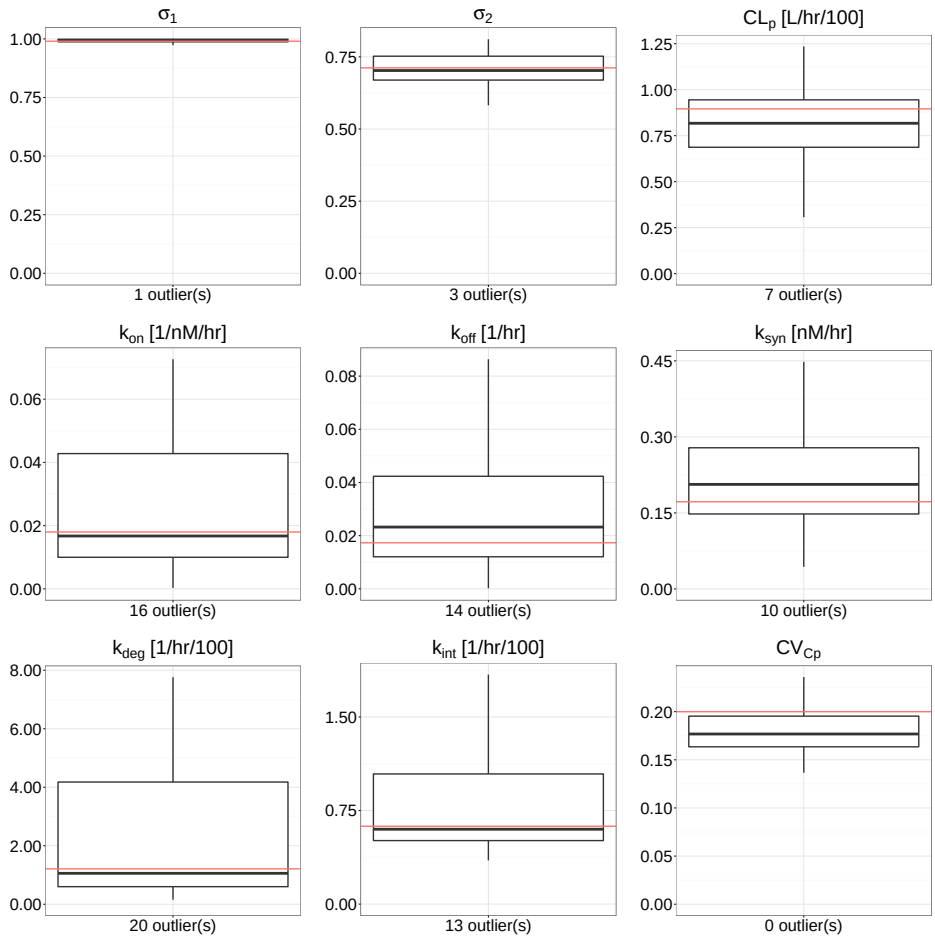

Figure 4.8: Boxplots of the estimates obtained by fitting the Full Model on the 100 datasets with only C_p measurements (scenario i.). The bottom and top of the box represent the first and third quartiles, while the band inside the box is the median; whiskers extend till ± 1.5 IQR (Inter Quartile Range). The horizontal red line indicates the true value of the parameter.

Table 4.6: Identification scenarios in decreasing order based on the maximum CV% of the parameter estimates; the third column indicates the parameter that leads to the maximum CV%.

Scenario	max CV%	parameter
Model A, i.	184.3	k_{deg}
Model A, ii.	160.5	k_{deg}
Full Model, i.	107.3	k_{deg}
Full Model, ii.	97.1	k_{on}
Full Model, iii.	93.4	k_{off}
Model B, iii.	71.4	k_{ss}
Model A, iii.	65.7	k_{ss}

this ranking, the scenario that gives the minimum maximum CV% is the third one, where both plasma drug concentration and tissue target concentration are measured.

As for CWRES and GOF plots, they did not show significant trends in any scenario (see e.g. Figure 4.9). Indeed, the distribution of the residuals always appears compatible with a Gaussian with null mean and unitary variance (they are often comprised between -2 and 2). GOF plots, representing the simulated data (DV) compared to the population prediction (PRED), show a behavior in accordance with the proportional residual error model: the scatterplot is concentrated around the identity line and the dispersion appears to be greater for higher concentrations. Despite the great variability in parameter estimates, in every scenario the PPs show that the corresponding predicted curves agree well with the noise-free measurable outputs considered. These plots were produced by overlapping the noise-free simulated data to the percentiles of the noise-free predicted curves obtained in each "100 runs set". An example is reported in Figure 4.10, for the scenario which presented the highest parameter CV% (see Table 4.6), i.e. Model A

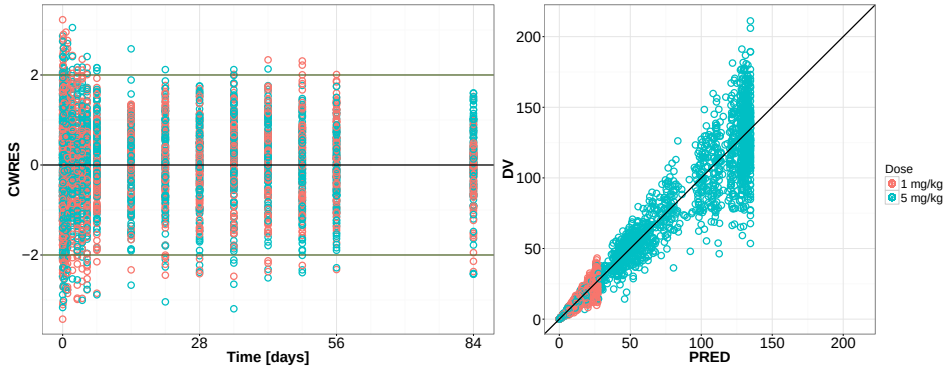

Figure 4.9: An example of CWRES vs time (left panel) and GOF plot (right panel) obtained for the Full Model estimated on plasma data (scenario i.). On the left, the residuals for all 100 NONMEM runs are grouped together; on the right, the data (DV) are compared to the predictions (PRED) for both doses and all runs (units: mg/L).

and plasma drug concentration as output measure.

Since the results obtained for a posteriori identifiability depend on data richness, alternative and possibly more informative sampling designs were considered.

Alternative designs

The two other sampling schedules considered were:

- an optimal one, in order to minimize the variance of parameter Maximum-Likelihood (ML) estimators;
- a more frequent one, in order to increase the amount of information.

More in detail, the more frequent sampling schedule was obtained assuming that each output variable (i., ii., iii.) can be measured every 5

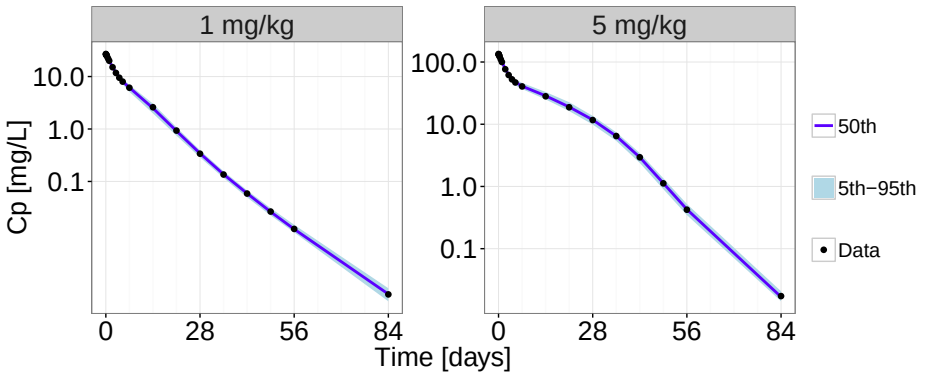

Figure 4.10: PP with the profiles of plasma concentration obtained with all the combinations of parameters estimated for Model A on plasmatic data. 5th, 50th and 95th percentiles of estimated profiles (area and line) are reported, together with noise-free simulated data (points).

hours up to day 84. The aim is to see if by collecting more data it is possible to improve the a posteriori identifiability. The optimal sampling schedule instead was obtained via PFIM, a software tool which evaluates and/or optimizes population designs based on the expression of the FIM in nonlinear mixed effects models [63]. Each possible output, C_p, $C_{leaky_{total}}$ and $R_{leaky_{total}}$ was considered separately in the optimization process, mostly because they were associated with a different number of requested samplings. For more details about the settings implemented in PFIM, see Appendix A, Section A.3.
The schedules obtained via optimal sampling still contain a realistic number of sample times; the results of all optimizations are represented in Figure 4.11.

The a posteriori identifiability analysis procedure presented in Section 4.4.2 was repeated using datasets generated with the more fre-

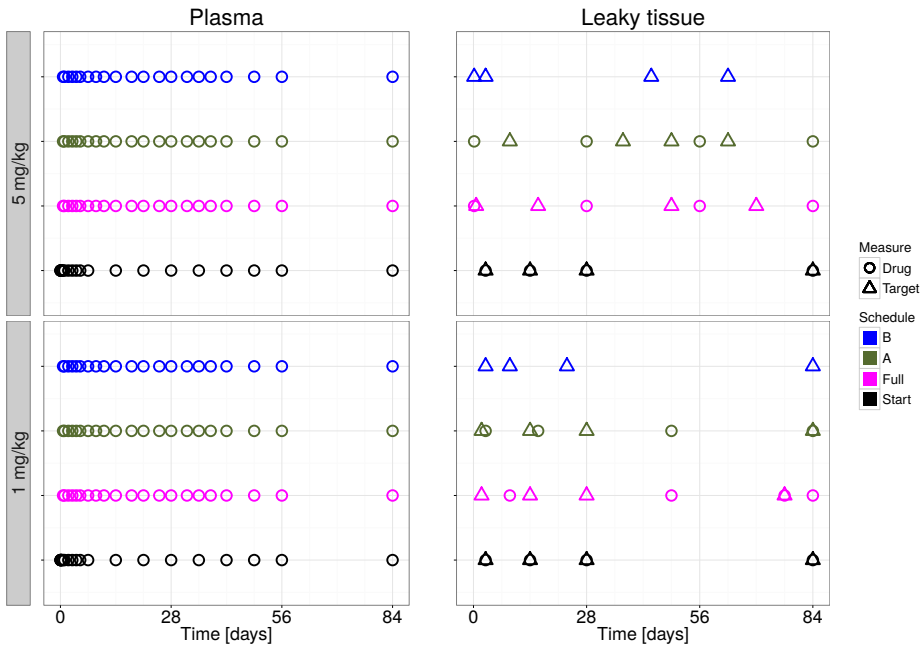

Figure 4.11: Optimal sampling schedules obtained with PFIM, for high (upper panels) and low (lower panels) dose level. The 21 optimal drug samples in plasma (left) and 4+4 optimal drug and target samples in leaky tissue (right) for each a priori identifiable model, compared with the initial schedule (Start), are represented.

quent sampling and with the optimal sampling. As an illustrative example, in Table 4.7 a comparison of CV% for Model A estimates identified on plasma data is reported.
It can be observed that the use of an optimal sampling schedule does not improve significantly the estimates precision with respect to the original realistic sampling schedule used for the analysis. The more frequent sampling seems to provide a better identification of the model parameters, maintaing the CV% of all parameter estimates below 45%. This does not hold for all models in all scenarios: for the full model, the dispersion in k_{on} and k_{off} estimates remains high even with the more frequent sampling (CV% $>$ 55% in scenario ii. and iii., greater than 85% in scenario i.).
In summary, the identifiability issues cannot be considered resolved by the realistic optimal design, while the unrealistic frequent sampling provides an appreciable improvement in parameter estimates dispersion, especially for simplified models; these observations would point to an overall over-parametrization issue.

Target saturating dose

The previous sections have shown that the addition of tissue data improves the identification of some critical parameters and that more frequent sampling improves precision on estimates, but not the optimal design. Here, a third dose of 20 mg/kg has been considered to assess potential improvements in practical identifiability. Data for the three scenarios i., ii. and iii. were again simulated with the full model, at doses: 1, 5 and 20 mg/kg. Full model and model A were tested for a posteriori identifiability on all the three scenarios, while model B only on scenario iii. CV% and δ were computed for comparison with the two doses condition.
When considering only plasmatic concentrations (scenario i.), both for full model and model A, the CV% generally decrease (with the

Table 4.7: CV% of Model A parameter estimates obtained from plasmatic data (scenario i.) with the three sampling schedules.

parameter	CV% for different sampling schedules		
	original	optimal	frequent
σ_1	0.6	0.6	0.2
σ_2	7.4	6.2	2.3
CL_p	24.0	12.5	2.3
k_{ss}	110.1	102.6	20.6
k_{syn}	44.3	29.5	8.5
k_{deg}	184.3	165.2	42.9
k_{int}	37.3	32.3	10.2
CV_{C_p}	11.8	12.5	2.4

exception of k_{ss} for model A), but they do not go below 60% (see Table 4.8).
By adding tissue concentrations (scenario ii. and iii.), CV% reduction becomes more significant. In particular, for model A in scenario iii., δ on average is equal to 15% and it is always below 40% (see Table 4.8), which is reasonable, since in data simulation a 20% and a 30% proportional residual errors were included, respectively, for drug in plasma or tissue, and target tissue concentration. For the full model instead, δ upper limit is around 80% for both scenarios, while for model B (scenario iii.) the maximum δ is approximately 50%.

4.5 Discussion

The integration of mPBPK and TMDD models has been studied in depth for mAbs binding to their pharmacological target in tissues with leaky vasculature.

Table 4.8: CV% and δ of Model A parameter estimates obtained from scenarios i. and iii., using either the two doses (1 and 5 mg/kg) or three doses (1, 5, and 20 mg/kg) datasets.

scenario	parameter	CV%		δ	
		two doses	three doses	two doses	three doses
i.	σ_1	0.564	0.563	0.612	0.565
	σ_2	7.405	4.620	7.385	4.649
	CL_p	23.958	5.826	23.308	5.846
	k_{ss}	110.068	115.188	79.982	83.183
	k_{syn}	44.270	18.962	47.252	19.524
	k_{deg}	184.312	160.134	1139.393	1051.462
	k_{int}	37.326	31.832	39.745	37.915
	CV_{C_p}	11.847	8.570	14.972	10.378
iii.	σ_1	0.535	0.535	0.594	0.561
	σ_2	4.699	2.976	4.694	3.133
	CL_p	14.676	4.817	14.525	4.842
	k_{ss}	65.665	41.98	58.761	39.965
	k_{syn}	27.825	16.083	27.516	15.888
	k_{deg}	40.371	22.23	49.960	22.866
	k_{int}	33.414	20.63	35.651	21.010
	CV_{C_p}	11.807	8.348	13.606	9.501
	$CV_{R_{tot}}$	34.14	22.308	32.607	22.143

First, a full mPBPK-TMDD model was built. Secondly, since the molecular processes are usually more rapid than PK processes, different approximations of TMDD dynamics based on QSS conditions were considered. Three additional mPBPK-TMDD models (model A, B and C) were hence derived adding sequentially QSS approximations, respectively on: (a) antibody-target complex concentration, (b) target concentration, and (c) free antibody concentration.
The four mPBPK-TMDD models have been simulated and compared to assess the effects of quasi-steady-state assumptions on both drug and target concentration-time profiles. The simulations have shown that model A generates the closest profiles to the full model, while model B differs mainly in the target concentration profiles, and model C systematically deviates from the full one for both drug and target concentrations at the site of action. A sensitivity test focused on plasma drug concentration and drug and target concentration in binding tissue, highlighted their insensitiveness to k_D, probably due to a confounding effect of k_{on} and k_{off} influences.
A priori and a posteriori identifiability of the four mPBPK-TMDD models were explored in three experimental scenarios: (i) when measurements of drug in plasma are available, and with possible addition of (ii) total drug in tissue or (iii) total target in tissue data.
A priori identifiability is always met for the full model and for model A, while such property is valid in model B only when both total target concentration in binding tissue and drug plasma concentration can be assessed. A priori identifiability cannot be assessed for model C.
The study of the a posteriori identifiability by an MC method highlighted practical identifiability issues, especially when only measurements relative to the drug, either in tissue or in plasma, are available. To overcome identifiability issues, three possible solutions have been attempted, by enriching the experimental design: (i) the use of optimal design methods, performed on the sampling scheme, (ii) the resort to a non-realistic high number of sampling instants, equally spaced,

(iii) the addition of an informative dose. While the use of an optimal or more frequent sampling schedule could not improve significantly the practical identifiability of all parameters, the addition of a saturating dose to the dataset was able to bear noticeable improvements in terms of CV%, especially when target in tissue data were considered available.

As reported in [54], mPBPK-TMDD models can handle TMDD at the target-expressing tissues, thus extending the usual TMDD modeling framework, where target binding is considered only in vascular space. Nevertheless, in contrast with what was suggested in the same work [54], mPBPK-TMDD models with binding occurring in the ISF (specifically, in our case, in leaky tissues), do present parameter identifiability issues, especially when only plasmatic data, collected with a realistic sampling, are available.

Besides providing explicitly the equations of four mPBPK-TMDD models, pointing out their behavior in terms of drug and target concentration profiles, this work addressed the potential identifiability issues of these models, indicating possible solutions (via informative study designs). In particular, the a priori identifiability of full model and model A in three scenarios, and of model B in the presence of target concentration in binding tissue measurements was analytically demonstrated. For all the four models, practical identifiability issues were highlighted in all scenarios and two possible solutions were proposed. In fact, the inclusion of target data in tissue and the addition of a saturating dose can reduce identifiability uncertainty, especially if both remedies are applied.

However, these solutions may not be always viable. Target concentration in tissue is not easily measurable, hence it may not be always assessed. Furthermore, the evaluation of sufficiently high doses may not be possible: a dose providing enough target saturation to improve parameter identification could also lead to toxicity episodes.

While the use of mPBPK-TMDD models allows the inclusion in a

mechanistic framework of PK and PK-PD information, attention should be given to the existence of practical identifiability issues. In general, for any model, such issues could be first easily detected via simulations, investigating different designs, dosing regimens, and parameter values. This is demonstrated in the next chapter, using as a case study the full TMDD model, whose practical identifiability issues have been mentioned in Chapter 3 (Section 3.2).

Chapter 5

PK/PK-PD simulator for exploring a TMDD model

Prior or in addition to a thorough model analysis as the one presented in Chapter 4, identifiability issues can be first detected with an exploratory simulation analysis. Indeed, simulation experiments can be employed to explore assumptions made about the model's structure and parameters, and to investigate experimental designs [64]. With appropriate tools, it is possible to investigate model-predicted profiles in different scenarios (e.g. changing parameter values and dosing regimens), inferring possible model identifiability issues.
A valid visualization software is necessary to allow for rapid exploratory analyses, for hypotheses verification and generation [65]: interactive web-based applications created with the R package Shiny (`https://shiny.rstudio.com/`) appear to be the ideal tool for the listed purposes. For this reason, a Shiny app for PK and PK-PD model simulation and exploration, called INES (INteractive Explorator and Simulator), was developed within this thesis project.
In this chapter, an exploratory analysis of the full TMDD model is

conducted with INES, to demonstrate how inference on the model can be made starting from simulations. First, the Shiny app INES is briefly introduced, and the settings of the simulations are listed (Section 5.1). Then, the exploratory analysis steps are presented and developed (Section 5.2). Finally (in Section 5.3) the main results of this chapter are discussed. Details about INES structure, both in terms of processing code and user interface are reported in Appendix B, together with a digression about a corollary tool.

5.1 Simulation tool and settings

INES is an interactive web-based Shiny application, written in R code. It is able to simulate, both deterministically and stochastically, the models contained in its PK and PD repositories. The PK repository contains also the full TMDD model [4] presented in Chapter 3, Section 3.2, without peripheral compartment. The models included in the repositories can all be implemented either with a 0^{th} order input (e.g. IV bolus) or 1^{st} order input (e.g. oral administration). INES is provided with a user-friendly web interface, where PK/PD model, parameters, dosing schedules, and simulation time instants can be set and interactively changed. INES generates output plots (concentration vs time, effect vs time, effect vs concentration), and tables summing up simulation settings and results. More details about INES processing code, user interface, and features are provided in Appendix B.

The full TMDD model implemented in INES is here considered as a case study, assuming that drug administration is provided via a single IV bolus. Parameters have been selected as in [66], see Table 5.1; parameter notations are as in Chapter 4 (see Section 4.1).

Table 5.1: Case study TMDD model parameters.

parameter	value	unit
V_p	3.75	L
k_{10}	0.0015	1/hr
k_{on}	0.091	1/(mg/L)/hr
k_{off}	0.001	1/hr
k_{syn}	0.11	(mg/L)/hr
k_{deg}	0.0089	1/hr
k_{int}	0.003	1/hr

5.2 Simulations at different doses

Model simulations were generated with INES at low doses (1.125, 3.75, 11.25, and 37.5 mg) and high doses (112.5, 375, 1125, and 3375 mg), see Figure 5.1. The dose-dependent PK implied by the TMDD model is here evident. Indeed, while for low doses the PK behavior appears to be approximately linear, for high doses it is clearly nonlinear.

By comparing, at different doses, the full TMDD model and the one compartmental linear model, a "threshold dose" representing the demarcation line between approximate linear and nonlinear behavior can be identified. The low and high doses listed above were tested; parameters for the one-compartment linear model were selected as $V = 3.75$ L (as in the TMDD model) and $CL = (k_{10} + k_{on}\frac{k_{syn}}{k_{deg}})/V$ (i.e. approximately 4.22 L/hr). Comparing the model-derived concentration profiles, both on the natural and semilogarithmic scale, it can be observed that for low doses, from 1.125 to 11.25 mg, differences in the two PK models are visible for small concentrations, and hence more discernible on the semilogarithmic scale (see Figure 5.2 (a) and (b)). These differences could be misinterpreted as stochastic dispersion when identifying

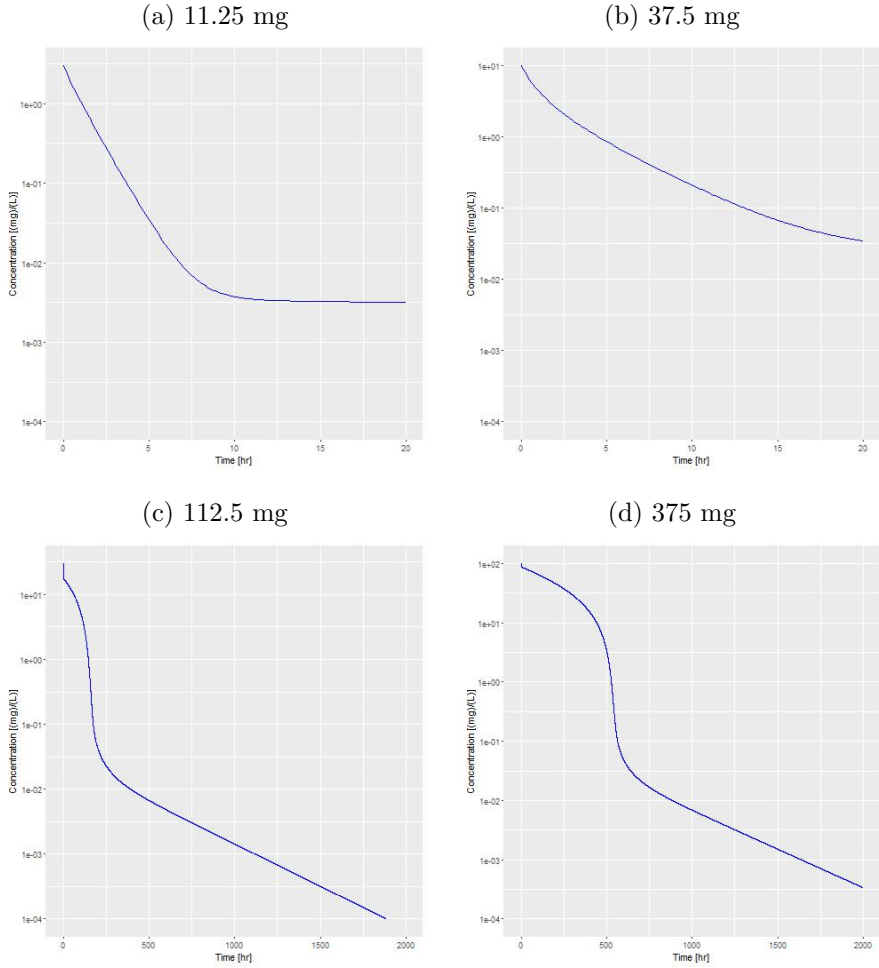

Figure 5.1: Plots downloaded from INES, representing drug concentration in central compartment in semilogarithmic scale for two low doses: (a) 11.25 mg, (b) 37.5 mg; and for two high doses: (c) 112.5 mg, (d) 375 mg.

a noisy dataset, containing only plasmatic data after low dose administration: in this case, the linear model would probably be considered the best choice and the TMDD model would be non-identifiable. With a dose of 37.5 mg, on the natural scale, the linear and nonlinear profiles appear similar, yet it can be easily observed that the TMDD model has a slower descent (see Figure 5.2 (c) and (d)). For doses from 112.5 to 3375 mg, the difference is marked: for instance for 112.5 mg, the nonlinear profile is close to zero at a time greater than 150 hr, while the one-compartment model becomes null before 15 hr (Figure 5.3).

5.3 Simulations with different parameters: rough sensitivity analysis

In order to further explore the model, exploiting the interactivity of INES, it is possible to perform a rough sensitivity analysis (similar to the one reported in Chapter 4, Section 4.3), by modifying the order of magnitude of each parameter (e.g. multiplying or dividing its value by ten) and observing the possible concentration profile changes. The doses here considered as reference are 11.25 mg (low) and 1125 mg (high).
For the low dose, for instance, changing the value of k_{10} ($k_{10} = 0.015$ or $k_{10} = 0.00015$ 1/hr), it can be observed that the concentration profile both in natural and semilogarithmic scale does not drastically change (see e.g. Figure 5.4). For k_{off}, differences are visible only on the semilogarithmic scale for small concentrations. For k_{int}, changes in the concentration profile can be observed only when the parameter is multiplied by ten and the plot is on semilogarithmic scale, for concentrations below 10^{-2} mg/L. For all other parameters, changes are always discernible for all concentration magnitudes, and for both plot

(a) 1.125 mg, natural scale

(b) 1.125 mg, semilog scale

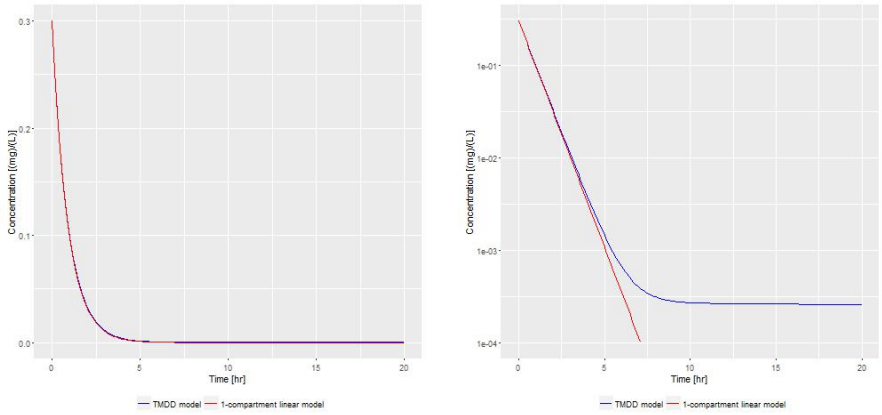

(c) 37.5 mg, natural scale

(d) 37.5 mh, semilog scale

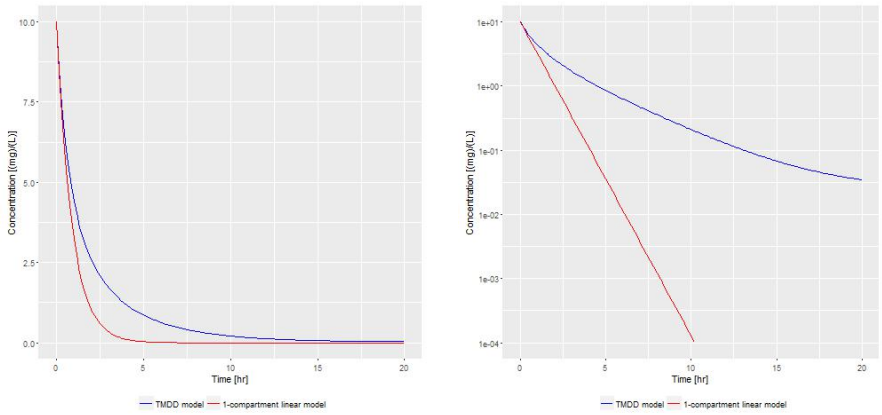

Figure 5.2: Plots downloaded from INES, representing drug concentration in central compartment, obtained from TMDD (blue) and one-compartment linear models (red), following the low doses of 1.125 mg (top), or of 37.5 mg (bottom), in natural scale (left) and semilogarithmic scale (right).

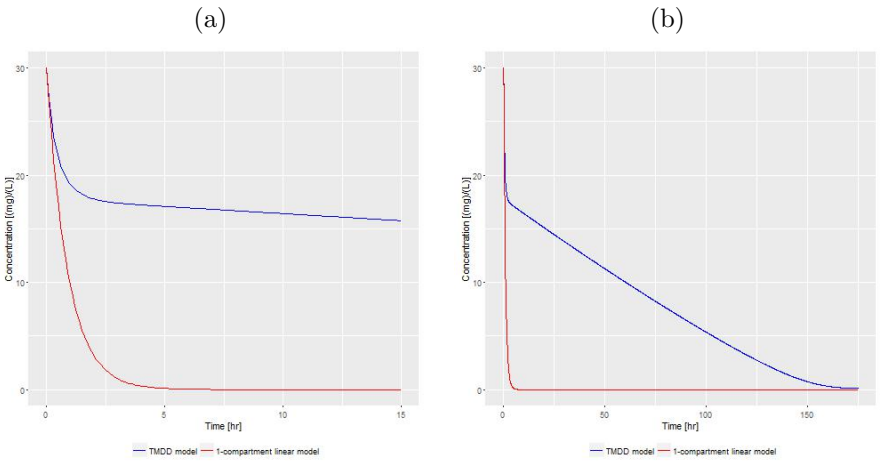

Figure 5.3: Plots downloaded from INES, representing drug concentration in central compartment, obtained from TMDD (blue) and one-compartment linear models (red), following the high dose of 112.5 mg, truncated at 15 hr (left) or after 150 hr (right).

(a) Sensitivity with respect to k_{10} (b) Sensitivity with respect to k_{syn}

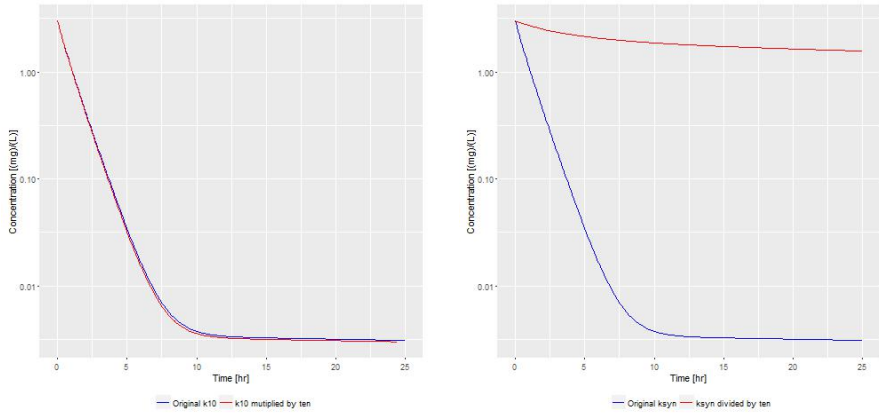

Figure 5.4: Comparison of drug concentrations obtained with the low dose (11.25 mg), by changing (a) k_{10} (multiplied by ten), (b) k_{syn} (divided by ten). Plots downloaded from INES.

scales (natural or semilogarithmic; see e.g. k_{syn} in Figure 5.4).

For the high dose, by increasing k_{on} (i.e., $k_{on} = 0.91$ 1/(mg/L)/hr), it can be observed that the concentration profiles are only slightly different (differences for concentrations approximately below 10 mg/L, better visible on semilogarithmic scale, see Figure 5.5). The same holds for k_{off} and k_{int}, where differences are clearly discernible only on semilogarithmic scale for concentrations below 1-10 mg/L. For all other parameters, changes in drug concentration are easily detectable (see e.g. Figure 5.5).

From this rough sensitivity analysis, it can be inferred that, when only plasma drug concentration data are available, if only low doses are studied, it may be difficult to identify k_{10}. This can be explained considering that at low drug concentrations the target is not saturated, hence the linear clearance pathway and the TMDD-related one

(a) Sensitivity with respect to k_{on} (b) Sensitivity with respect to k_{deg}

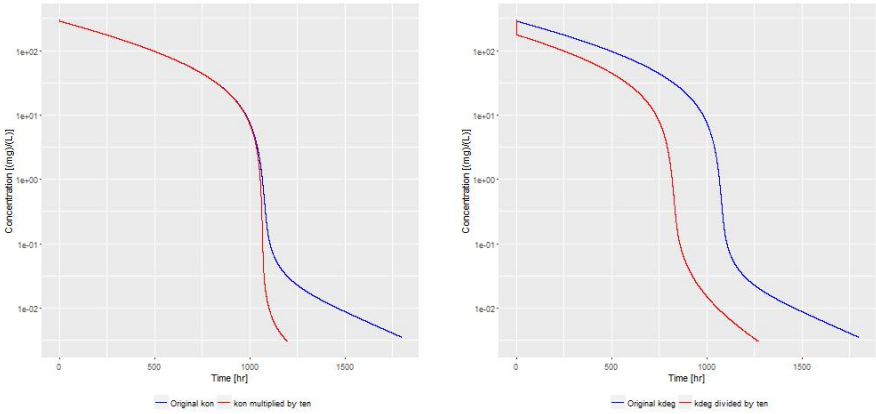

Figure 5.5: Comparison of drug concentrations obtained with the high dose (1125 mg), by changing (a) k_{on} (multiplied by ten), (b) k_{deg} (divided by ten). Plots downloaded from INES.

are not distinguishable. Furthermore, identifiability issues can rise for parameters related to binding and complex internalization: k_{on} does not influence the concentration profile for high doses, while modifications in k_{off} and k_{int} values do not imply significant PK changes, both at low and high doses. Obviously, these considerations are valid only locally, around the reference parameters of Table 5.1, for doses similar to the ones here considered.
Anyway, these observations may be seen as a confirmation of the complexity of the full TMDD model, both in terms of differences in processes time-scale and of over-parametrization.

5.4 Deterministic and stochastic explorations of significant thresholds

When the initial plasma drug concentration is larger than the endogenous receptor concentration (i.e., $R(0) = \frac{k_{syn}}{k_{deg}} \simeq 12.36$ mg/L), the dynamics of the TMDD model results in a characteristic plasma drug concentration profile. On the semilogarithmic scale, four different phases are clearly distinguishable [66]: (i) a brief initial phase, where drug and target rapidly equilibrate; (ii) an apparent linear phase, where target is saturated and drug is eliminated mainly via a slow 1^{st} order process; (iii) a transition phase, where the target is no longer saturated and drug is eliminated both linearly and via TMDD; (iv) a linear terminal phase, where the drug concentration is so low that drug and drug-target complex elimination is a linear 1^{st} order process. The target saturation phase (ii) might be of particular interest, as it gives information about parameters not related to drug-target binding and internalization (k_{10}, k_{syn}, k_{deg}). Under the hypothesis $C_p(0) \geq R(0)$, this phase can be assumed to start right after bolus administration (because of the rapidity of drug and target equilibration), and it ends

when C_p becomes comparable to the dissociation constant k_D, here $\simeq 0.011$ mg/L [66]. By plotting the TMDD PK profile together with a concentration threshold at $10k_D$ (under which C_p and k_D are considered comparable), it is possible to deduce the duration of target saturation phase.
For the high doses here explored (112.5, 375, 1125, and 3375 mg), the required hypothesis on $C_p(0)$ is satisfied. For instance, for the 112.5 mg dose, the target saturation phase lasts about 7 days. Hence, in this case, sufficiently rich data should be collected during the first week of treatment in order to facilitate the identification of k_{10}, k_{syn}, and k_{deg}. With stochastic simulations, it is also possible to evaluate the impact of variability on the duration of target saturation phase and, more generally, on TMDD model-derived plasma drug concentration. A virtual population composed of 100 patients is built, assuming that k_{on}, k_{off}, and k_{int} are equal for all individuals, while V, k_{10}, k_{syn}, and k_{deg} display inter-individual variability (IIV) following a lognormal distribution. In particular the latter parameters are supposed to be uncorrelated. The CV% are equal to 30% and 50%, for V and k_{10} respectively, while equal to 20% for k_{syn} and k_{deg}. Even if IIV has been included only on four parameters, and with reasonable CV%, its impact on the duration of target saturation phase is remarkable, especially for higher doses. For instance, by plotting the 5th, 50th and 95th percentiles of the plasma drug concentrations observed in the virtual population taking the dose of 3375 mg, it can be observed that the duration of target saturation phase can span from about 5 weeks to about four months (Figure 5.6).

INES displays only graphically the impact of variability on model outcomes in general, and on the achievement of significant thresholds in particular. A quantitative evaluation corresponds to the computation of the PTS. PTS is indeed defined as the probability of achieving specific PK and/or PD thresholds following a particular dosing regimen, considering both variability (e.g. IIV) and uncertainty (e.g. due

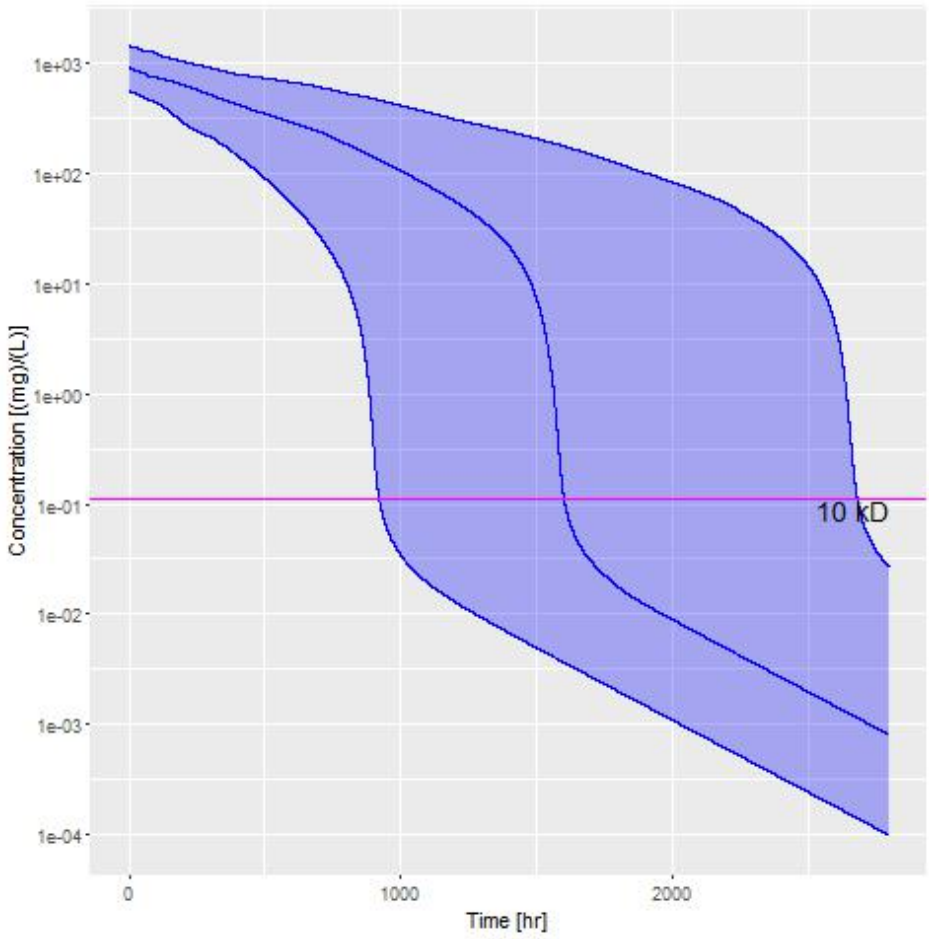

Figure 5.6: Drug concentration obtained in the simulated population administered with 3375 mg (plot downloaded from INES). The three blue lines represent 5th, 50th and 95th concentration percentiles, while the horizontal line represents the $10k_D$ threshold.

to allometric scaling) on model parameters. PTS is usually computed for a range of doses or for different dosage regimens in order to find the most convenient (or "successful"), i.e. the one that gives the highest probability. Following the example presented here, one could compute PTS e.g. in order to find the dose which maximizes the proportion of patients achieving $C_p = 10k_D$ after a certain time instant.
An additional Shiny application, simply called "PTS app", was built specifically for PTS computation; it is briefly discussed in Appendix B.

5.5 Discussion

During model building and selection, it is important to be aware of the peculiar characteristics and the weaknesses of the models taken into consideration, e.g. for which PK or PD features they are usually indicated, or in which scenarios they are identifiable. In order to have a good grasp on the model, simulation and identifiability analyses are highly recommended. Simulations, in particular, represent a valuable means by which identifiability issues and model peculiarities can be first detected, e.g. before diving into solving algebraic problems like a priori identifiability assessment, or setting up MC analyses for a posteriori identifiability evaluation.
Interactive simulation tools provide a starting point for model exploration, allowing to test different scenarios. The achievement of clinically and theoretically significant thresholds, and the impact of random variability on model outcomes can be also visually inspected.
INES is taken as an example tool, to show how to implement model exploration. With its unique and user-friendly graphical interface, this Shiny application offers a simple way to perform interactive model simulations. Furthemore, it returns a series of graphical outputs, together with tables that afford the implementation of possible further

analyses in other softwares. Of course, INES, as a newly created tool, still needs further testing and refinement, especially as far as it regards efficiency in differential equations solving.
In this work, via INES, it was demonstrated how to perform and exploit exploratory simulation analyses to make inference on the full TMDD model. In particular, this model was explored through the following steps: (i) simulations at low and high doses, (ii) (rough) sensitivity analysis, (iii) deterministic and stochastic exploration of significant thresholds. These analyses allowed to draw inferences about: (i) model dose-dependence and nonlinearity, (ii) parameter influence on possibly measurable model outcomes, (iii) impact of nonlinearity and variability on model outcomes (and thresholds attainment).
Indeed, by simulating the full TMDD model at different dose levels, it was made evident that this model is able to replicate the dose-dependency often observed in mAbs PK. Furthermore, it was noted that for low doses it could be difficult to discern between a linear and a nonlinear TMDD-related behavior, especially if only noisy blood data are available, which is often the case. In this experimental scenario, through a quick sensitivity analysis, it was possible to detect which parameters could be practically non identifiable according to the dose level. By investigating significant thresholds achievement, it could be inferred in which time intervals it may be important to sample, in order to identify specific model parameters. Finally, via stochastic simulations, the great impact of random variability (e.g. IIV) on this nonlinear TMDD model outcomes was observed, e.g. suggesting that, in an actual trial where a mAb is administered to a patient population, high variations in PK/PD endpoints achievement can be expected among individuals.
The observations that were made in this chapter are partly dependent on the parameter and dose level choices; nevertheless the presented work represents a useful example of exploratory analysis. The inferences obtained from such analysis not only may be used as a basis

for further investigations but could help establishing whether the full TMDD model is appropriate for a complete characterization of the data at hand.
As already mentioned in Chapter 3 (Section 3.2) and as remarked here, when only blood data are available, the identification of the full TMDD model may not be a viable choice. Therefore, in this experimental scenario, either approximated or empirical models may represent valid instruments for mAb PK assessement. This is exemplified in the next chapter, where both rituximab PK and its interaction with a small molecule in CLL patients are characterized via an empirical compartmental model.

Chapter 6

Application in oncology: TMDD phenomenon as the cause of DDIs

When either nonlinear or linear mAb PK needs to be assessed, especially on sparse and/or poor data, simple and easily identifiable models are often preferred over more complex mechanistic models (as the one explored in the previous chapter).
Indeed, in [7], a simple two-compartment model with both linear and nonlinear elimination was considered for describing rituximab PK in CLL patients. In the work presented in this chapter, this model was identified and refined via evaluation of covariate effects using data coming from the HELIOS trial, where CLL patients received rituximab in combination either with bendamustine and placebo or bendamustine and ibrutinib.
In Section 6.1, some relevant information about rituximab and ibrutinib is reported. Then, in Section 6.2, details about the HELIOS trial design and assessments are illustrated. In Section 6.3 model build-

ing methods and results are described, and finally in Section 6.4 a discussion about the main contributions of this work is presented.

6.1 The drugs: rituximab and ibrutinib

Rituximab is a genetically engineered chimeric murine/human monoclonal IgG1 antibody, directed against the CD20 antigen on the surface of normal and malignant B cells. In particular, in vitro, the Fab domain binds to the CD20 antigen on B lymphocytes, and the Fc domain recruits immune effectors functions to mediate B-cell lysis. It is currently approved for the treatment of NHL, CLL, and rheumatoid arthritis [67].
For the treatment of patients with CD20-positive CLL (both previously treated and untreated), rituximab is indicated in combination with the chemotherapy fludarabine and cyclophosphamide [67]. However, most patients eventually experience relapse and may become refractory to fludarabine-containing regimens. For such patients, rituximab in combination with the alkylating agent bendamustine (BR) may represent an effective and safe alternative treatment [68, 69].
Ibrutinib, an oral covalent inhibitor of Bruton's tyrosine kinase (BTK, a key enzyme in B-cell signaling), is also indicated for the treatment of patients with B-cell malignancies, such as CLL/Small Lymphocytic Lymphoma (SLL) [70]. In this population, single-agent ibrutinib has been shown to significantly improve overall survival in both relapsed/refractory and previously untreated patients [70]. The addition of ibrutinib to BR (BR-I) was investigated in a phase Ib study to determine its safety and efficacy in patients with previously treated CLL: therapy was well tolerated and effective [71].
In a recent phase III study, HELIOS, the efficacy and safety of the combination BR-I versus BR were assessed in patients with previously treated relapsed/refractory CLL or SLL [69].

6.2 The HELIOS trial

HELIOS was a phase III, randomized, placebo-controlled, double blind study, whose design and main efficacy and safety results have been published in [69]. Eligible patients were ≥ 18 years, had a diagnosis of CLL or SLL, and had relapsed or refractory disease with at least ≥ 1 previous lines of systemic therapy. Patients with del(17p) were excluded. Eligible patients were randomly assigned to receive 420 mg ibrutinib (n = 289) or placebo (n = 289) in combination with 6 cycles (28 days per cycle) of bendamustine and rituximab until disease progression or unacceptable toxicity. The bendamustine IV dose was 70 mg/m^2 on days 2-3 of cycle 1 and days 1-2 of cycles 2-6. The rituximab IV dose was 375 mg/m^2 on day 1 of cycle 1 and 500 mg/m^2 on day 1 of cycles 2-6. Infusion durations were typically 30 minutes for bendamustine and varied based on individual tolerability for rituximab (as per rituximab prescribing information [67]). The study was performed in accordance with the principles of the Declaration of Helsinki and the guidelines for Good Clinical Practice.
In the next subsections, details about study assessments (Subsection 6.2.1) and observational PK results (Subsection 6.2.2) are presented.

6.2.1 Study Assessments

Ibrutinib PK samples were collected from all patients at predose, 1, 2, and 4 hours on day 1 of cycles 1 and 2. In a subset of patients at selected study sites, sparse blood sampling was performed in both treatment arms for bendamustine and rituximab PK analyses, for the exploration of PK interactions between the three drugs. Bendamustine PK samples were collected on day 2 of cycles 1 and 2 at predose, end of infusion, and at 1, 2, and 4 hours. Rituximab PK samples were collected on days 1 (predose) and 15 of cycle 1, day 1 (predose) of cycles 2-6, and on day 1 of cycles 7-9 (washout phase) [72, 73].

The primary efficacy endpoint of HELIOS was progression-free survival (defined as the interval between the date of randomization and the date of disease progression or death); for other secondary endpoints, see [69]. Tumor burden was evaluated via computed tomography scans at baseline and then every 12 weeks. It was assessed as sum of the products of the two largest diameters of the selected lesions (SPD), according to iwCLL 2008 criteria [74]. Treatment with BR-I led to significant improvements in disease outcomes, including PFS, overall response, and quality of life, without unexpected or cumulative toxicities [69].
All adverse events, with the exception of progression of CLL/SLL, were collected until 30 days following the last dose of study treatment or until the start of a subsequent systemic antineoplastic therapy, if earlier. Adverse events reported after 30 days following the last dose of study treatment were to be reported if considered related to study treatment. Safety was reported for all randomized patients who received ≥ 1 dose of study drug. No relevant differences in safety profile were observed between the BR-I and BR arms with the increase in systemic exposure of rituximab.

6.2.2 Observational PK results

Bendamustine and rituximab PK samples were collected only at selected study sites from 178 patients; 84 and 94 patients from the placebo and ibrutinib arm, respectively. Demographics and baseline characteristics were comparable between both treatment arms in the pharmacokinetic population. The mean dose levels of bendamustine and rituximab were also similar in the placebo (68.9 ± 4.7 and 465.2 ± 65.0 mg/m^2, respectively) and ibrutinib arm (68.2 ± 6.3 and 468.1 ± 55.3 mg/m^2, respectively).
Dose-normalized bendamustine (70 mg/m^2) and rituximab (500 mg/m^2) concentration-time data were stratified by treatment to evaluate the

effect of ibrutinib on the PK of bendamustine and rituximab. For bendamustine, they were comparable in the two treatment arms, indicating that ibrutinib did not alter bendamustine PK [72]. Conversely, systemic exposure of rituximab was higher in patients coadministered with ibrutinib than in patients who received placebo. Mean predose serum concentrations were 2- to 3-fold higher in the first three cycles and 1.2- to 1.7-fold higher in subsequent cycles (Figure 6.1) [72, 73].

It was hypothesized that this difference in rituximab exposure may be linked to TMDD. As reported in previous works [7, 75, 76], rituximab PK appear to be nonlinear, probably mainly because of TMDD, where CD20-positive B cells represent the pharmacological target. This would explain the dose-dependence of rituximab PK: the number of target cells is decreased by the treatment and, in turn, influences rituximab disposition and elimination [31]. Furthermore, circulating drug levels have been shown to be affected by tumor burden in an inversely proportional way: clinical studies have demonstrated that a high tumor burden is associated with low rituximab serum levels [37, 76, 77, 78]. This is because the tumor cells act as a sink for the antibody, adsorbing rituximab via CD20 binding and inducing target mediated elimination.

Ibrutinib is a drug characterized by a fast clinical response [79, 80]; since this is believed to happen via B-cells depletion, rituximab TMDD-related clearance should be lower when the BTK inhibitor is given. The aim of the work presented in this chapter is to explore the validity of this hypothesis and describe the observed PK interaction using a NLME modeling approach.

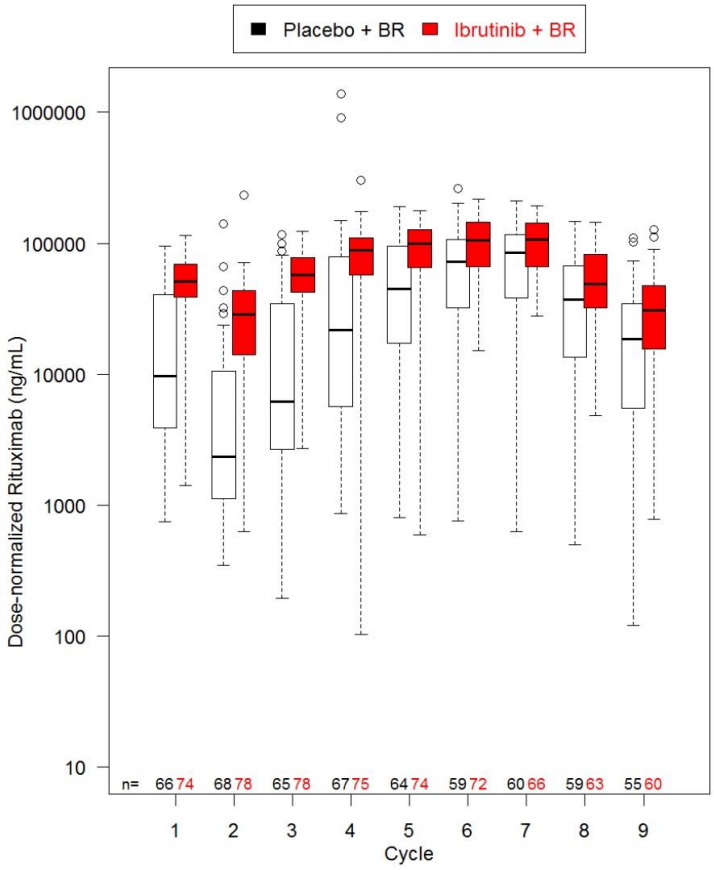

Figure 6.1: Log-transformed rituximab serum concentrations vs time, normalized to the dose of 500 mg/m^2, in subjects co-administered with placebo (white boxes) or ibrutinib (red boxes) in the HELIOS study. The extremes of the boxes identify the 25th and 75th concentration percentiles for each cycle; the horizontal lines in the boxes represent medians; the whiskers extend till ± 1.5 IQR (Inter Quartile Range); outliers are represented as open circles. At the bottom: n refers to the number of samples analyzed at each cycle (black for placebo arm, red for ibrutinib arm).

6.3 Model building

In order to describe the observed change in rituximab exposure according to the treatment arm, and to demonstrate that the amount of target plays an important role in this phenomenon, both rituximab PK data and tumor burden assessments (SPD) were needed. In the HELIOS study, non-missing values for rituximab serum concentrations were reported only for 157 patients out of 178 (71 for BR arm, 86 for BR-I arm). SPD instead was assessed in 156 patients, but only 149 had more than two measurements (one of which at baseline). By intersecting the two subsets, only 147 remained available for analysis, 70 for the BR arm and 77 for the BR-I arm. Demographics and baseline characteristics of this subset are reported in Table 6.1.
In the next subsection (Subsection 6.3.1) the steps and the approaches employed for model building are described. Then, results of this procedure are presented and validated (Subsection 6.3.2).

6.3.1 Methods

Population rituximab PK was assessed using NLME modeling implemented in NONMEM version 7.1.0 (first-order conditional estimation [FOCE] method). A published model for rituximab PK in CLL patients was used as basis [7]. As serum concentration-time relationship displayed bi-exponential decay and time-dependent PK was observed in the selected population, in [7] a 2-compartment model comprising a time-varying clearance component was selected. The model (Figure 6.2) was parameterized in terms of: (i) a constant clearance term related to endogenous catabolic processes of IgG (CL_1), (ii) a time-varying clearance term related to the decrease in capacity of the target mediated clearance pathway, expressed as a decreasing exponential ($CL_{2_0} \exp(-k_{des}t)$), (iii) apparent volumes of distribution in the central and peripheral compartments (V_1 and V_2), and (iv) inter-

Table 6.1: Characteristics of the 147 patients with both rituximab PK data and SPD assessments.

	BR (n=70)	BR-I (n=77)
Number of rituximab PK observations	562	612
Number of SPD observations	381	476
Male patients, n (%)	45 (64.3)	46 (59.7)
Female patients, n (%)	25 (35.7)	31 (40.3)
Median age (range), yrs	61 (36-83)	61 (40-82)
Median body weight (range), kg	78.35 (45-130)	82.75 (52.5-125.4)*
Median CRCL (range), mL/min	82.8 (47.0-197.3)	91.5 (43.8-207.3)*
Median TB (range), μmol/L	10.5 (3.42-36.3)	10.6 (3.42-28.4)
Median ALT (range), U/L	21 (4.3-101.7)	22 (9-75)
Median AST (range), U/L	23.15 (10-67)	23 (5-57.1)

BR = bendamustine and rituximab; I=ibrutinib; SPD=Sum of the Products of the largest Diameters; CRCL=Creatinine Clearance; TB=Total Bilirubin; ALT=alanine transaminase; AST=aspartate transaminase; *Data missing for 1 subject.

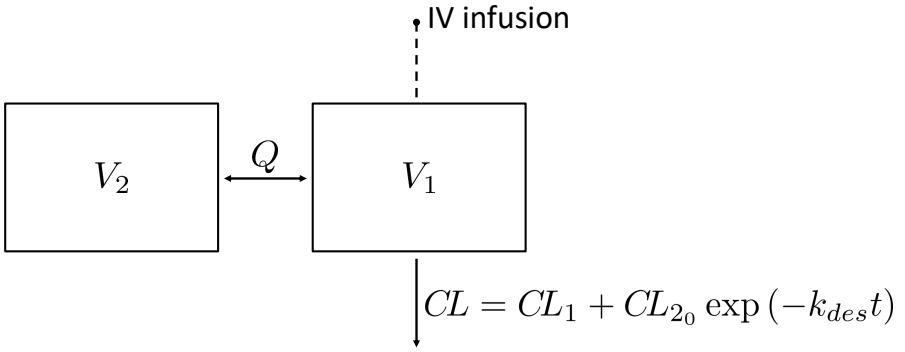

Figure 6.2: Base model for rituximab PK [7].

compartmental clearance (Q).

No covariate analysis was performed in [7] because of the limited number of patients in the available study. Here, the PK model was applied and refined via evaluation of covariate effects (see Figure 6.3), using the data coming from the patients depicted in Table 6.1. More in detail, model parameters were initialized equal to the estimates obtained in [7]; inter-compartmental clearance Q and volume of peripheral compartment V_2 were kept fixed and without IIV, as essentially only C_{trough} data were available from the HELIOS study. Volume of distribution in the central compartment V_1, instead, was not fixed, but its IIV was negligible and hence removed from the model.
Inclusion of sex as categorical covariate was investigated, as it is often reported as significant for rituximab clearance or volume of distribution [81]. As weight is correlated with sex, it was also tested as a continuous covariate. Furthermore, in order to characterize the observed PK differences in the two study arms, the influence of treatment arm was explored via the inclusion of a categorical covariate. It is hypothesized that the difference in exposure between the BR and BR-I arms

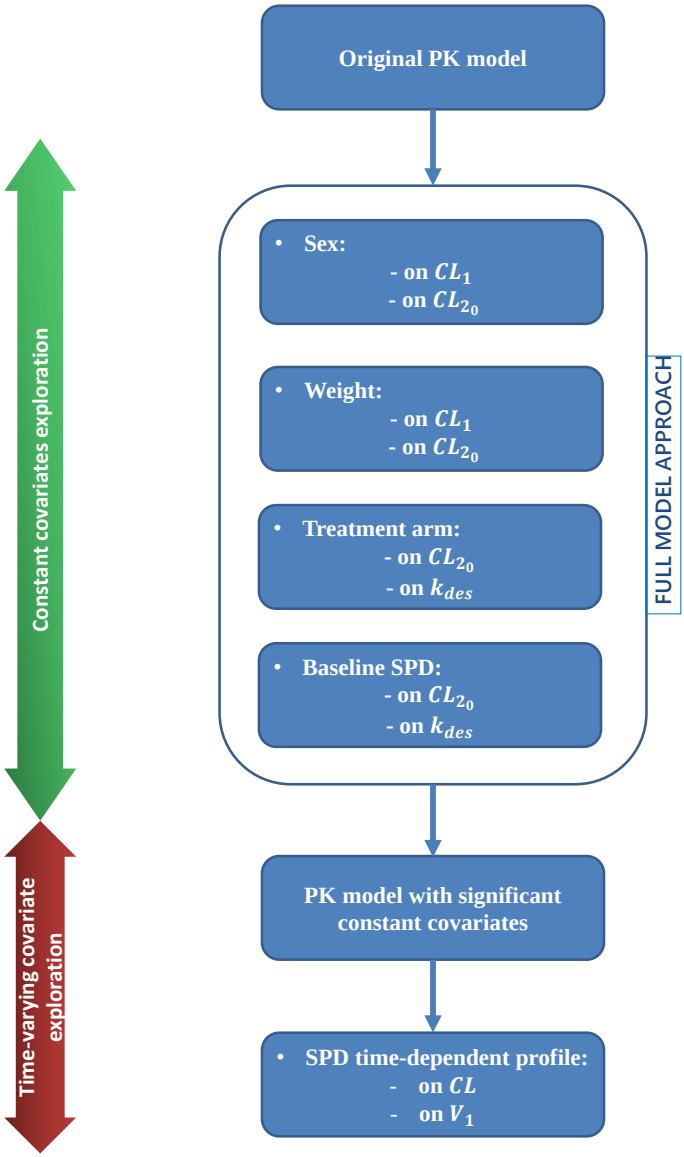

Figure 6.3: Scheme of model building methods.

observed in HELIOS study is due, at least in part, to TMDD, as B cells are targeted by rituximab and depleted by ibrutinib. For this reason, tumor burden (measured as SPD) was evaluated as meaningful covariate, considering the effects of both baseline value (continuous constant covariate) and of the entire time-dependent profile (continuous time-varying covariate).
Constant (both categorical and continuous) covariate analysis was performed with the full model approach, based on clinical significance and estimates precision [82]. According to this approach, the relationships between covariates and parameters, to be included in the full model, are selected based on known pharmacological information and plausibility. After simultaneous identification of these relationships, their meaningfulness is inferred from parameter estimates and their CIs. Here, only sex and weight influences were tested on CL_1: as this parameter represents endogenous clearance, neither treatment arm nor baseline SPD effect should be meaningful. On CL_{2_0} instead, all four constant covariates were tested for inclusion, while on k_{des} only the influence of treatment and baseline SPD (treatment- and disease-related covariates) was evaluated. No constant covariates were tested on V_1, V_2 and Q, as they do not have IIV.
Once the full covariate model was built and identified, and the non-significant constant covariates were removed, the influence of time-varying SPD, on total clearance (CL) and on volume of distribution in the central compartment (V_1), was investigated. The entire time-dependent SPD profile was obtained via linear interpolation of the PD data (Figure 6.4). Categorical covariates were included as flags for PK parameters, while continuous covariates, both constant and time-varying, were tested via power models. In particular, time-varying SPD values were normalized via median baseline (4567.2 mm^2), and the power model was tested via the inclusion as an additive term on

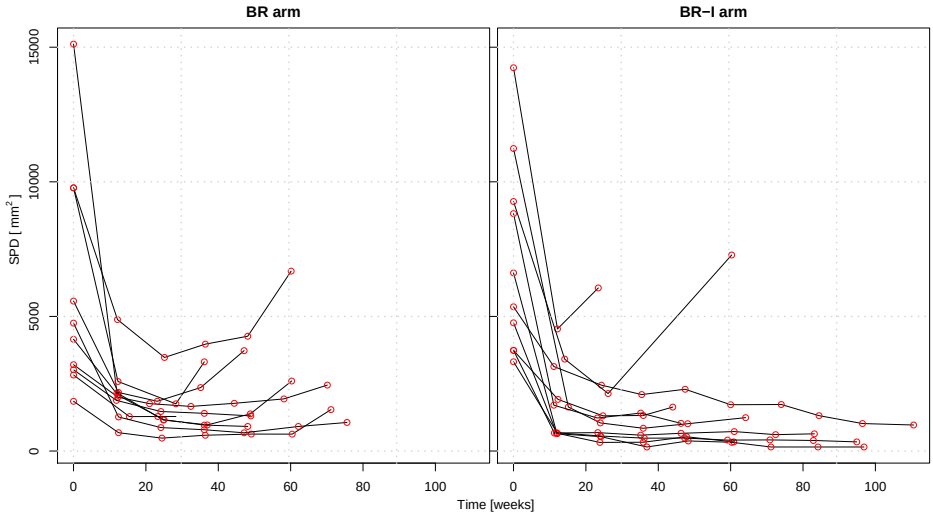

Figure 6.4: Linear interpolation (black lines) of individual SPD data (red dots). As an example, ten subjects from each treatment arm are depicted; BR arm on the left, and BR-I on the right.

total clearance and as a substitute for the constant term on volume:

$$CL = CL_1 + CL_{2_0} \exp(-k_{des} t) + CL_{2_P} \left(\frac{SPD}{4567.2}\right)^{pow}$$
$$V_1 = V_{1_0} \left(\frac{SPD}{4567.2}\right)^{\gamma_V}$$

Parameters with IIV were assumed to be lognormally distributed in the population. Residual error on PK observations was included with an additive model, using the logarithm-both-sides approach.
Model diagnostics were obtained via Pirana 2.9.5b and R version 3.2.4; the R software was used also for the realization of model plots.

6.3.2 Results

From the estimation of the full covariate model, sex and weight resulted to be significant on endogenous clearance (CL_1), as well as treatment on time-varying clearance decay (k_{des}). Indeed, CIs for CL_1 in males (M) and females (F) were respectively $9.35 \div 12.2$ and $6.85 \div 9.69$ (mL/hr), while the exponent of the power model for weight inclusion on CL_1 had CI equal to $0.051 \div 0.977$ and was estimated as approximately 0.5. CIs for k_{des} in patients treated with BR or BR-I combination were, respectively, $0.000755 \div 0.00203$ and $0.00857 \div 0.0308$ (1/hr).
As far as CL_{2_0} is concerned, the CIs in males and females, treated either with ibrutinib or placebo co-administration were overlapping ($54.5 \div 96.9$ for F+BR, $35.4 \div 123.2$ for F+BR-I, $57.3 \div 75.7$ for M+BR, $45.4, 84.6$ for M+BR-I, in mL/hr). Furthermore, the CI of the exponent of the power model for baseline SPD effect on CL_{2_0} included the value zero ($-0.099 \div 0.265$). Exponents of the power models for weight inclusion on CL_{2_0} and for baseline SPD inclusion on k_{des} were estimated to be close to zero.
The model including only the significant constant covariates was further refined by testing the inclusion of SPD as a continuous time-varying covariate on total clearance (CL) and volume of distribution

in the central compartment (V_1). The inclusion of SPD on CL provided a better fit (see Figures 6.5, 6.6, 6.7), while its inclusion on V_1 led to model over-parameterization and was not considered relevant as the exponent of the power model was small (with magnitude 10^{-2}).

Hence, the final structure of the mixed effects model is represented by the following equations:

$$\begin{aligned}
CL_{1_{TV}} &= (SEX CL_{1_F} + (1 - SEX) CL_{1_M}) \left(\frac{WT}{80.1}\right)^{\gamma_{WT}} \\
k_{des_{TV}} &= (1 - IBR) k_{des_{BR}} + IBR k_{des_{BR-I}} \\
CL &= CL_1 + CL_{2_0} exp(-k_{des} t) + CL_{2_P} \left(\frac{SPD}{4567.2}\right)^{pow} \\
\frac{dA_1}{dt} &= -A_1 \frac{Q}{V_1} - A_1 \frac{CL}{V_1} + A_2 \frac{Q}{V_2} \\
\frac{dA_2}{dt} &= A_1 \frac{Q}{V_1} - A_2 \frac{Q}{V_2}
\end{aligned}$$

SEX is a flag variable equal to 1 for F and 0 for M; CL_{1_F} and CL_{1_M} are CL_1 for females and males, respectively. Similarly, IBR is a flag for ibrutinib administration (equal to 1 if co-administered, 0 otherwise); $k_{des_{BR}}$ and $k_{des_{BR-I}}$ are k_{des} values for the placebo and ibrutinib treatment arm, respectively. Finally, *WT* represents the individual weight (normalized by the median, 80.1 kg), and *SPD* is the time-varying tumor burden (with median baseline 4567.2 mm^2). Final model parameter estimates are reported in Table 6.2.

The declining exponential clearance term was included in rituximab PK model [7] as an empirical strategy to render target mediated clearance: the addition of the SPD-related term could make it unnecessary, as SPD is related to tumor burden and hence rituximab target. For this reason, also an alternative version of the final model, where the exponential term is removed from the expression of total clearance, was fitted to rituximab serum concentration data. Such a model provided

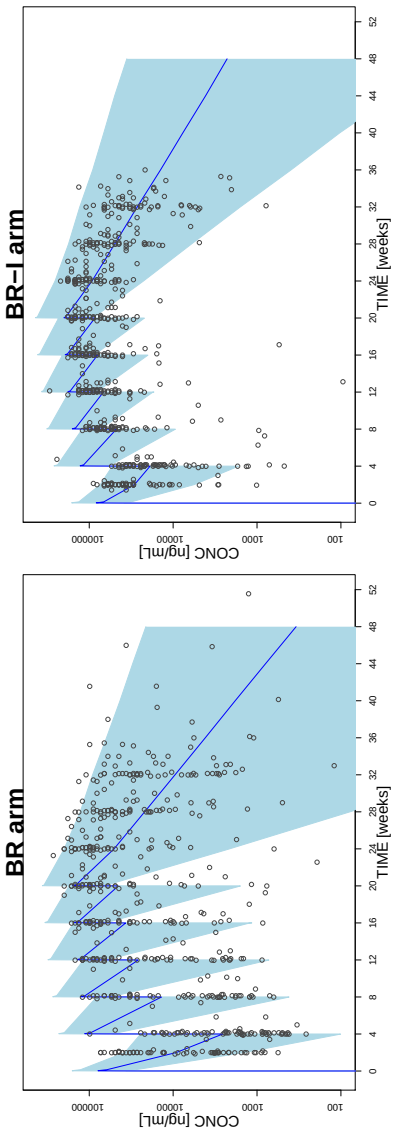

Figure 6.5: Visual predictive checks (VPCs) stratified on treatment arm. The dots represent observed PK data, the blue line the median of model-predicted rituximab serum concentration, and the light-blue area represents the 5th-95th percentile interval.

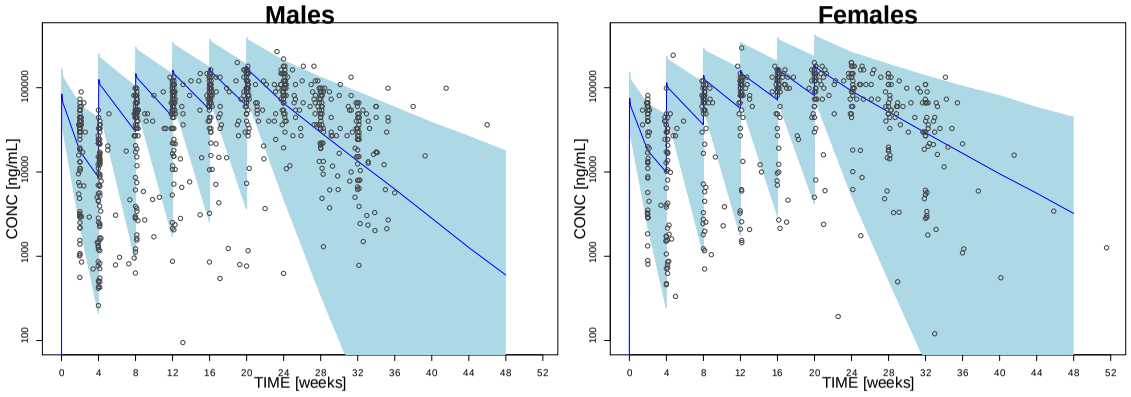

Figure 6.6: VPCs stratified on sex. The dots represent observed PK data, the blue line the median of model-predicted rituximab serum concentration, and the light-blue area represents the 5th-95th percentile interval.

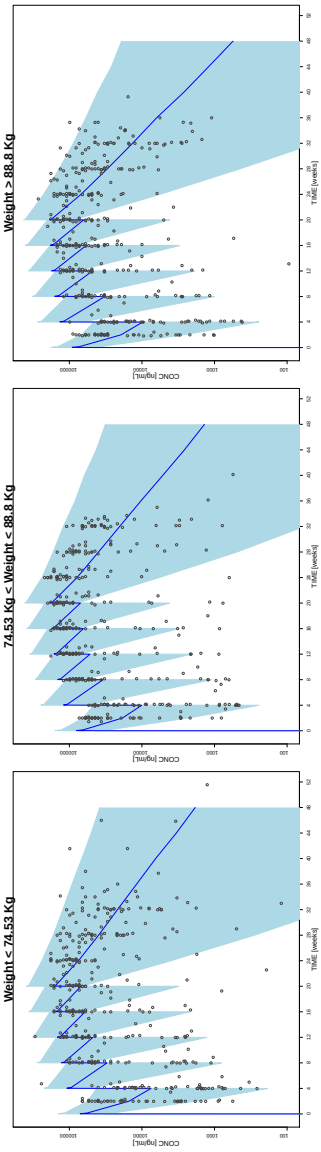

Figure 6.7: VPCs stratified on weight. The dots represent observed PK data, the blue line the median of model-predicted rituximab serum concentration, and the light-blue area represents the 5th-95th percentile interval.

Table 6.2: Final model parameter estimates and precisions (expressed as CV%).

Parameter	Estimate	CV%
CL_1 for F (mL/hr)	5.85	15%
CL_1 for M (mL/hr)	8.37	14%
γ_{WT}	0.73	10%
V_1 (mL)	8510	10%
Q (mL/hr)	47.9	FIX
V_2 (mL)	2320	FIX
k_{des} for BR arm (1/hr)	0.00146	20%
k_{des} for BR-I arm (1/hr)	0.0261	35%
CL_{2_0} (mL/hr)	67.4	11%
CL_{2_P} (mL/hr)	3.94	39%
pow	0.431	18%
IIV on CL_1 (ω_{CL_1})	0.165	39%
IIV on V_1 (ω_{V_1})	0	FIX
IIV on k_{des} ($\omega_{k_{des}}$)	2.3	30%
IIV on CL_{2_0} ($\omega_{CL_{2_0}}$)	0.146	46%
IIV on CL_{2_P} ($\omega_{CL_{2_P}}$)	1.11	56%
RV (σ_{add})	0.165	19%

F=females; M=males; FIX=fixed parameter; BR=bendamustine and rituximab; I=ibrutinib; IIV=inter-individual variability; RV=residual variability; ω=variance of parameter IIV term; σ=variance of residual variability term.

an increase in objective function of more than 500 points with respect to the model including all clearance terms. This indicated that the inclusion of SPD alone is not able to explain well the observed data.

6.4 Discussion

Herein, a model for rituximab PK was developed, based on the data from CLL patients enrolled in the HELIOS trial, co-administered with bendamustine and either ibrutinib or placebo. The main objective was to determine whether the difference in rituximab exposure observed in the BR and BR-I arms of the study, demonstrating an interaction between ibrutinib and the mAb, is due to TMDD.
Here, the amount of target influencing mAb disposition was not truly quantified: no measurements of B-cell counts were available. Nevertheless, tumor burden should be proportional to the amount of CD20-positive B cells; here SPD assessments were available.
Hence, besides sex, weight and treatment arm, which were found clinically significant, baseline and time-varying SPD were explored as potential covariates, to explore the influence of the amount of target on rituximab PK. In the end, baseline SPD was not found to be clinically significant, while the inclusion of the time-varying covariate on rituximab total clearance provided a better model fit. Final model parameters (Table 6.2) appear in agreement with those reported in [7], with the exception of the more rapid k_{des} in the BR-I arm. Indeed, when tumor burden effect was included in rituximab PK model, the influence of treatment on rituximab exposure was reflected only by a different decay rate in clearance. Patients administered with placebo display a slower clearance decay with respect to patients administered with ibrutinib. This is in agreement with the observed data (Figure 6.1), and with the hypothesis that the difference in exposures between the two treatment arms is due to ibrutinib-related target depletion,

which contributes to the decrease in target mediated clearance.
Tumor burden was already identified (together with baseline CD19) as statistically significant covariate (affecting CL_{2_0} and k_{des}) in the base PK model by Li et al [7] applied to NHL patients data [83]. Similarly, pretreatment tumor size was inversely correlated with exposure in Japanese NHL patients [84], and, recently, rituximab clearance was related to CD20 antigen count at baseline in CLL patients [85]. The tumor burden influence on rituximab exposure and response has also been confirmed in a mouse study [86].
Target mediated clearance was here expressed as sum of exponential and power model terms: it is noteworthy that the inclusion of an SPD-dependent term on total clearance did not permit to remove the empirical exponential term. This indicates that SPD alone is not able to fully explain the change in rituximab clearance during treatment; this observation was reported also in a similar work on another target mediated compound [87]. As SPD may not fully represent the overall tumor burden and/or B-cell count (i.e. rituximab target), such conclusion is not unexpected.
A limitation of the modeling assessment here reported was related to the sparse characterization of rituximab PK, which essentially included only trough concentrations. In addition, the developed PK model for rituximab may not be generally applicable as longitudinal measurements of tumor size (e.g. SPD) are not always available. Furthermore, the model here described is to some degree empirical. Additional data (e.g., PK, BTK occupancy, B-cell measurements, etc.) and further modeling work may be needed to have a fully mechanistic representation that further elucidates rituximab disposition, for instance employing a "true" TMDD model (e.g. full or QSS) or including a PD model for SPD progression. Moreover, the clinical significance of the presented findings needs additional exploration.
Although based on an empirical model and sparse data, the work presented in this chapter provided some mechanistic insight into ritux-

imab PK: it was made evident that TMDD plays a role in rituximab PK and that this phenomenon is at the basis of the observed interaction with ibrutinib.

Chapter 7

Conclusions

Therapeutic antibodies display peculiar PK features, different from those of small-molecule drugs [29]; the disposition of the majority of mAbs is, at least in part, target mediated. In order to capture the nonlinearity frequently observed in mAbs PK, numerous models have been proposed: (minimal) PBPK, mechanistic (e.g. explicitly including TMDD), and two-compartmental (with linear and/or nonlinear elimination).
The open challenges addressed in this thesis were to explore and deepen the understanding of mAbs PK and of the mathematical models usually employed to characterize its main features (e.g. nonlinearity), from the more complex ones, such as integrated mPBPK-TMDD models, to the simpler empirical compartmental ones.
In the following, the conclusions and the main contributions of the thesis are discussed.

Overall, this thesis represents an advancement in the understanding of the PK behavior of mAbs. Some mechanistic models were investigated, with a special focus on identifiability, to establish whether or not they can be used to characterize mAb PK, depending on the

experimental scenario. Furthermore, via an empirical model it was proved, for a specific mAb, that TMDD is involved in its PK processes and is the cause of an interaction with a small molecule.
More in detail, the integration of mPBPK and four different TMDD models has been considered and studied in depth, assuming that binding occurs in leaky tissues (Chapter 4). Four integrated models were built, incorporating into the mPBPK model the full TMDD model (full mPBPK-TMDD model), and three approximations based on QSS assumptions (model A, B and C). The four mPBPK-TMDD models have been analysed via simulation and sensitivity analyses, and in particular their identifiability has been assessed. It was analytically demonstrated whether and when the integrated models are a priori identifiable (except model C). Furthermore, it was observed that all four models display practical identifiability issues, and two possible solutions were proposed: the collection of target concentration data in tissue, and the evaluation of an additional high dose. Despite mPBPK-TMDD models may be key in mAbs discovery and development, by virtue of their mechanistic and physiological grounding, practical identifiability issues should be taken into account, especially when the use of rich experimental designs is not feasible.
Identifiability issues can be first detected via exploratory simulation analysis. This was shown using as a case study the full TMDD model, with the aid of the newly developed interactive tool INES (Chapter 5). Dose-dependence, influence of model parameters on measurable outcomes, and impact of random variability were investigated via deterministic and stochastic simulations, confirming the known complexity and identifiability issues of the model. This work demonstrated that a simple exploratory simulation analysis may provide important considerations, useful for further investigations, for having a good grasp on the model's peculiarities and weaknesses, and for establishing whether the model taken into account is appropriate for a complete characterization of the data at hand.

When the data are poor in information, it is often found that simpler models are needed to describe mAb PK. For instance, rituximab PK in CLL patients was first described via an empirical two-compartmental model with nonlinear and linear elimination [7], which was here refined via covariate inclusion. The relationship between rituximab serum levels and tumor burden (considered as a surrogate of target amount), already observed in [37, 77, 78], was here confirmed, giving further proof that rituximab PK is, at least in part, target mediated. Furthermore, the hypothesis that the interaction between rituximab and ibrutinib is due to rituximab TMDD was validated: the tumor burden seems to play a role in the change in clearance (and, hence, in exposure) of rituximab when ibrutinib is co-administered.

From a methodological point of view, it can be observed that, in the development of the thesis, different research objectives and models with a diverse degree of complexity have been discussed. The present investigation focused not only on theoretical aspects, such as sensitivity, identifiability and simulation analyses, but also practical ones, i.e. the identification of a model from real data. Accordingly, the models under study ranged from mechanistically grounded ones (either complex models integrating a mPBPK and a TMDD component, or simpler models considering only the TMDD phenomenon), to more empirical ones, well suited for identification purposes. These levels of description reflect the necessity of matching the complexity of the model with the research objective. When the research objective is more theoretical, more complex models can be employed; in this case, parameters may be obtained from physiological knowledge and/or previous publications. Instead, when the research objective is more practical, simpler models should be taken into consideration. This thesis has demonstrated that it is important to theoretically and/or graphically explore the model under exam before using it, either for simulation of new scenarios or identification on real data.

From the experimental and pharmacological point of view, this thesis provides considerations on models a priori and a posteriori identifiability, that can influence future study designs, e.g. the selection of the number and the level of doses to be tested, or the choice of additional measurements to be collected. An appropriately designed study, together with the application of a mechanistic model, could lead to a deeper physiological understanding of mAb PK processes. Furthermore, also the conclusions drawn for the case study of rituximab not only could inform possible future trials related to this mAb, but also suggest the testing of the TMDD and DDI hypotheses also in other contexts, where the underlying mechanisms of action are similar (other mAbs, other co-administrations, other diseases).

In conclusion, in this thesis, methods for exploring, building and refining mathematical models for mAb PK including TMDD were illustrated. The application of these methods is important to gain confidence with the model under exam, explore possible alternative study designs, and gain a deeper understanding of mAb PK processes.

Appendix A

Appendix to Chapter 4

A.1 A priori identifiability

A.1.1 Theory

A priori (structural) identifiability is a property of a nonlinear system based on its mathematical structure; it concerns the possibility to determine the parameters of the model (at least for suitable input functions) assuming that all observable variables are error-free [88]. Suppose that the system is represented as:

$$\begin{cases} \frac{dx}{dt} = f(x(t), p) + G(x(t), p)u(t) \\ y(t) = h(x(t), u(t), p) \end{cases} \tag{A.1}$$

where x is the $n-$dimensional state variable (e.g. concentration of drug in compartments), u is the $m-$dimensional input vector (e.g. an i.v. infusion), y is the $r-$dimensional output (e.g. measurable plasmatic drug concentration); $p \in P$ is the $q-$dimensional parameter vector. Then it is possible to provide the following technical definition (as

found in [88]):
Definition: Let $y = \phi(p, u)$ be the input-output map of the system in Equation A.1. Such system is said to be a priori globally identifiable if and only if, for at least a generic set of points $p^* \in P$, the equation

$$\phi(p^*, u) = \phi(p, u) \tag{A.2}$$

has only one solution $p^* = p$ for at least one input function u; the system is locally identifiable if and only if, for at least a generic set of points $p^* \in P$, Equation A.2 has more than one, but at most a finite number of solutions, for all input functions u; the system is nonidentifiable if, for at least a generic set of points $p^* \in P$, the equation has an infinite number of solutions for all input functions u.

A.1.2 Evaluation via Mathematica- Rationalized equations

The software tool Mathematica, with its IdentiabilityAnalysis package, was chosen to explore the local a priori identifiability of the four mPBPK-TMDD models presented in Chapter 4. Recalling that the method implemented in the IdentiabilityAnalysis package requires model equations to be rational, rationalized equations for model A and B are here reported.

Rationalized equations for model A. Adding a dummy variable x_A defined as:

$$x_A = \sqrt{(C_{leaky_{total}} - k_{ss} - R_{leaky_{total}})^2 + 4k_{ss}C_{leaky_{total}}},$$

from Equations 4.4 and 4.5, the rationalized equations for model A

are obtained:

$$
\begin{aligned}
C_p &= A_p/V_p \\
\frac{dA_p}{dt} &= In(t) + C_{lymph}L - C_pL1(1-\sigma_1) - C_pL_2(1-\sigma_2) \\
&\quad -C_pCL_p \\
\frac{dC_{tight}}{dt} &= \frac{1}{V_{tight}}\left[L_1(1-\sigma_1)C_p - L_1(1-\sigma_L)C_{tight}\right] \\
\frac{dC_{leaky_{total}}}{dt} &= \frac{1}{V_{leaky}}[L_2(1-\sigma_2)C_p - \frac{1}{2}L_2(1-\sigma_L)(C_{leaky_{total}} - k_{ss} \\
&\quad -R_{leaky_{total}} + x_A)] - k_{int}CR_{leaky} \\
\frac{dR_{leaky_{total}}}{dt} &= k_{syn} - k_{deg}R_{leaky_{total}} - (k_{deg} - k_{int})CR_{leaky} \\
\frac{dC_{lymph}}{dt} &= \frac{1}{V_{lymph}}[L_1(1-\sigma_L)C_{tight} + \frac{1}{2}L_2(1-\sigma_L)(C_{leaky_{total}} - k_{ss} \\
&\quad -R_{leaky_{total}} + x_A) - C_{lymph}L] \\
\frac{dx_A}{dt} &= \frac{1}{2x_A}[2C_{leaky_{total}}(\frac{1}{V_{leaky}}(C_pL_2(1-\sigma_2) - \frac{1}{2}(C_{leaky_{total}} \\
&\quad -k_{ss} - R_{leaky_{total}} + x_A)L_2(1-\sigma_L)) - k_{int}CR_{leaky} \\
&\quad +2R_{leaky_{total}}(k_{syn} - k_{deg}R_{leaky_{total}} \\
&\quad +(k_{deg} - k_{int})CR_{leaky} - 2k_{ss}(\frac{1}{V_{leaky}}(C_pL_2(1-\sigma_2) \\
&\quad -\frac{1}{2}(C_{leaky_{total}} - kss - R_{leaky_{total}} + x_A)L_2(1-\sigma_L)) \\
&\quad -k_{int}CR_{leaky} - 2C_{leaky_{total}}(k_{syn} - k_{deg}R_{leaky_{total}} \\
&\quad +(k_{deg} - k_{int})CR_{leaky} - 2R_{leaky_{total}}(\frac{1}{V_{leaky}}(C_pL_2(1-\sigma_2) \\
&\quad -\frac{1}{2}(C_{leaky_{total}} - k_{ss} - R_{leaky_{total}} + x_A)L_2(1-\sigma_L)) \\
&\quad -k_{int}CR_{leaky} + 2k_{ss}(k_{syn} - k_{deg}R_{leaky_{total}} \\
&\quad +(k_{deg} - k_{int})CR_{leaky})]
\end{aligned}
$$

where

$$CR_{leaky} = \frac{1}{2} R_{leaky_{total}} \frac{C_{leaky_{total}} - k_{ss} - R_{leaky_{total}} + x_A}{k_{ss} + \frac{1}{2}(C_{leaky_{total}} - k_{ss} - R_{leaky_{total}} + x_A)}$$

The notations are as in Chapter 4, Section 4.2. Initial conditions are: $C_p(0) = C_{tight}(0) = C_{leaky_{total}}(0) = C_{lymph}(0) = 0$, $R_{leaky_{total}} = k_{syn}/k_{deg}$, and $x_A(0) = -k_{ss} - k_{syn}/k_{deg}$.

Rationalized equations for model B. Similarly, for model B, the dummy variable x_B is introduced:

$$x_B = \sqrt{(k_{ss}k_{deg} - k_{int}C_{leaky_{total}} + k_{syn})^2 - 4k_{int}(-k_{ss}k_{deg}C_{leaky_{total}})},$$

and the following rationalized equations are derived from Equations 4.6 and 4.7:

$$\begin{aligned}
C_p &= A_p/V_p \\
\frac{dA_p}{dt} &= In(t) + C_{lymph}L - C_pL1(1-\sigma_1) - C_pL_2(1-\sigma_2) \\
&\quad -C_pCL_p \\
\frac{dC_{tight}}{dt} &= \frac{1}{V_{tight}}\left[L_1(1-\sigma_1)C_p - L_1(1-\sigma_L)C_{tight}\right] \\
\frac{dC_{leaky_{total}}}{dt} &= \frac{1}{V_{leaky}}[L_2(1-\sigma_2)C_p - \frac{L_2}{2k_{int}}(1-\sigma_L)(-k_{ss}k_{deg} \\
&\quad +k_{int}C_{leaky_{total}} - k_{syn} + x_B)] - k_{int}CR_{leaky} \\
\frac{dC_{lymph}}{dt} &= \frac{1}{V_{lymph}}[L_1(1-\sigma_L)C_{tight} + \frac{L_2}{2k_{int}}(1-\sigma_L)(-k_{ss}k_{deg} \\
&\quad +k_{int}C_{leaky_{total}} - k_{syn} + x_B) - C_{lymph}L]
\end{aligned}$$

$$\begin{aligned}\frac{dx_B}{dt} &= \frac{1}{2x_B}[2k_{int}^2 C_{leaky_{total}}(\frac{1}{V_{leaky}}(C_p L_2(1-\sigma_2)\\ &-\frac{L_2}{2k_{int}}(1-\sigma_L)(-k_{ss}k_{deg}+k_{int}C_{leaky_{total}}-k_{syn}\\ &+x_B))-k_{int}CR_{leaky})+2k_{int}k_{ss}k_{deg}(\frac{1}{V_{leaky}}(C_p L_2(1-\sigma_2)\\ &-\frac{L_2}{2k_{int}}(1-\sigma_L)(-k_{ss}k_{deg}+k_{int}C_{leaky_{total}}-k_{syn}+x_B))\\ &-k_{int}CR_{leaky})-2k_{int}k_{syn}(\frac{1}{V_{leaky}}(C_p L_2(1-\sigma_2)\\ &-\frac{L_2}{2k_{int}}(1-\sigma_L)(-k_{ss}k_{deg}+k_{int}C_{leaky_{total}}-k_{syn}+x_B))\\ &-k_{int}CR_{leaky})]\end{aligned}$$

where

$$CR_{leaky} = \frac{k_{syn}(-k_{ss}k_{deg}+k_{int}C_{leaky_{total}}-k_{syn}+x_B)}{k_{int}(k_{ss}k_{deg}+k_{int}C_{leaky_{total}}-k_{syn}+x_B)}$$

Notations and initial conditions are again as in Chapter 4, Section 4.2; furthermore, $x_B(0) = k_{ss}k_{deg} + k_{syn}$.

A.2 A posteriori identifiability

A.2.1 Theory

The notion of a posteriori (practical) identifiability refers to the quantity and quality of the collected data, i.e. their informativeness [89, 90]. Observed data are actually discrete and noisy, so that Equation A.1 is replaced by

$$\begin{cases} \frac{dx}{dt} = f(x(t),p) + G(x(t),p)u(t) \\ y(t_k) = h(x(t_k),u(t_k),p) + e_k, k = 1,\ldots,n \end{cases} \tag{A.3}$$

where $e \sim \mathcal{N}(0, \Sigma)$, $e = [e_1, \ldots, e_n]^T$. Letting $y = [y(t_1), \ldots, y(t_n)]^T$, it follows also that $y = \phi(p, u) + e$, where $u = [u(t_1), \ldots, u(t_n)]^T$, and ϕ is the input-output map defined in Section A.1. Hence the observed data $y(t_k)$ are realizations of random variables, implying that the same holds for parameter estimates $\hat{p}$ [90]. For this reason, true values of the parameters cannot be requested to be uniquely determined from the observed data; instead, the practical identifiability requirement applies to the confidence region of their estimates, which has to be bounded.

The FIM $\mathcal{I}(p)$ accounts for the effect on the variance of the parameter estimate of measurement error e and sensitivities of predicted responses to model parameters at all sampling times [57]:

$$\mathcal{I}(p) = \mathbb{E}\left[\left(\frac{\partial \ell(y;p)}{\partial p}\right)^2\right] \tag{A.4}$$

where $\ell(y;p)$ is the natural logarithm of the likelihood function.

Under regularity assumptions [91], $\mathcal{I}(p)$ is linked to $C = Var(\hat{p})$ by the Cramér-Rao inequality:

$$C \geq \mathcal{I}(p)^{-1}. \tag{A.5}$$

The FIM $\mathcal{I}(p)$ is strictly connected to the notion of a posteriori identifiability. More precisely, a statistical model is said to be a posteriori identifiable if its associated $\mathcal{I}(p)$ has full rank [57].

Given an estimate $\hat{p}$ of the parameter vector p the FIM can be estimated as:

$$\hat{\mathcal{I}}(\hat{p}) = S(\hat{p})^T \Sigma^{-1} S(\hat{p}), \tag{A.6}$$

where $S(\hat{p}) = \partial\phi(\hat{p}, u)/\partial p$ is the sensivity matrix, and Σ is the covariance matrix for residual error.

In the context of a posteriori identifiability analysis, the role of the FIM is twofold. Its rank can be checked to assess the sharp fulfillment of the a posteriori identifiability condition. Furthermore, even

when it has full rank, it is worth inspecting its singular values in order to assess the size of the confidence region, given that a (formally) a posteriori identifiable model may still give rise to extremely unreliable estimates.
In practice, due to the need to resort to the estimate in Equation A.6 and numerical uncertainties, it may be difficult to unambigously ascertain the full rank condition [57], so that the condition number becomes a natural surrogate measure for identifiability. The condition number of a matrix is the ratio of the largest to the smallest of its singular values. When it is large, the multivariate confidence ellipsoid of parameter estimates is strongly elongated in at least one direction [90].
In the context of a simulation study like the one presented in Chapter 4, the information coming from the FIM can be complemented with a MC study (see Subsection 4.4.2). MC simulation based on the true model is used to gain information about the reliability of each parameter estimate. In particular, the MC procedure can be used to evaluate:

- boxplot and outliers, to assess shape and dispersion of estimate univariate distributions
- sample variance and confidence intervals, to quantify the dispersion of the empirical distributions
- bias and RMSE, to consider the difference between the expected value of the univariate distributions and the true value of the parameter
- CV% and δ (as defined in Subsection 4.4.2) to assess the dispersion of parameter estimates relative to expected and true value.

Fitting quality can also be graphically explored via:

- concentration profiles over time, to display the predictive performance of the mPBPK-TMDD models with the estimated sets of parameters

- CWRES against time and dependent variable, together with GOF plots, to evaluate the capability of the model to match the data

- PPs, to evaluate the distribution of predicted concentration profiles based on the distribution of parameter estimates.

A.2.2 Evaluation via R and NONMEM

R version 3.1.2 was used both for computing the condition number of the FIM (for all a priori identifiable mPBPK-TMDD models and scenarios) and for the MC procedure, as reported in Chapter 4. The ODEs of the mPBPK-TMDD models were solved using the deSolve package. The model parameters were then estimated with NONMEM version 7.3, with the FOCE method, initializing the algorithm with a parameter perturbation of $\pm 15\%$ from the real values. The creation and the execution of the control stream files were automated via suitably written batch files. As far as running times are concerned, NONMEM 7.3 could fit a "100 runs block" in 1 to 13 minutes, depending on the fitted model and the number of measurable outputs considered, on a PC with Intel(R) Core(TM) i7 processor, at 2.40 GHz. R was also used for the output analysis of the estimation processes.

A.3 Optimal design

A.3.1 Theory

Optimal design aims at establishing the experiment design which guarantees the "best" identification of nonlinear mixed effects model parameters. Optimization methods based on the FIM $\mathcal{I}(p)$ have been developed: according to the Cramér-Rao inequality, the inverse of $\mathcal{I}(p)$ is the lower bound of the variance-covariance matrix of any unbiased estimator of the parameters (see Equation A.5). The "best" identification of the parameters is obtained when their confidence region is as small as possible: following the D-optimality criterion, this can be achieved by minimizing the determinant of the inverse of the FIM [63]. From the square roots of the diagonal elements of the inverse of $\mathcal{I}(p)$, the predicted standard errors (SE) for estimated parameters can be calculated.

A.3.2 Evaluation via PFIM

The software tool PFIM optimizes population design using the D-optimal criterion; it was here employed for applying optimal design to the mPBPK-TMDD models that resulted a priori identifiable.
For each model, the objective was to find a vector of optimal sampling times for both dose levels (1 and 5 mg/kg), for each possible measurable output. The population FIM was selected (FIM="P"); the variances of the IIV terms had to be fixed to a value close to, but different from, zero in the optimization phase. After the optimization, an evaluation of the optimal design(s) with all the variances equal to zero was performed to obtain the correct criterion (equal to $det(\text{FIM})^{1/n_p}$, where n_p is the number of parameters). Furthermore, the block diagonal FIM was computed, as no dependence of intraindi-

vidual variability on fixed effects was considered. Since it was required to obtain 21 optimal sampling time points for plasmatic antibody concentration, and 4 for peripheric antibody and target concentration, the optimization was performed separately for each output, exploiting the Fedorov-Wynn algorithm [92].
Optimal sampling times have to be selected from a user-specified grid, that must include the instants of the initial schedule. The additional time instants to be inserted in the grid can be chosen through a graphical inspection of the sensitivities, i.e. the derivatives of the measurable output with respect to the parameters as functions of time. Here, a grid of 27 and 20 time points was built respectively for plasmatic concentration and for peripheric antibody and target concentration. PFIM performance times were around 5 hours and a half for plasmatic concentration sampling optimization, and approximately 5 minutes for peripheric concentrations sampling optimization, on a PC with Intel(R) Core(TM) i5 processor, at 2.67 GHz.

Appendix B

Appendix to Chapter 5

B.1 INES: a tool for exploring mathematical models

INES is a Shiny application developed within this thesis project. It is based on R code and its structure consists of two main R files:

- server.R, i.e. the processing code of the application,
- ui.R, with the instructions for building the user interface.

B.1.1 server.R

From the processing code file, server.R, other R functions are called, contributing to the functioning of the app (see Figure B.1). In fact, the PK and PD models, fundamental elements of INES, are written as separate R functions, contained in two distinct folders, which are referred to as PK and PD repositories. In order to keep track of measurement

units and avoid conversion mistakes, an additional R function for measurement units computation is provided.

Each PK and PD model function takes as input the model parameters and the simulation time instants in which the output has to be computed. PK models require also the dosing schedule to be selected; the main output is drug concentration in the central compartment over time. PD models require as additional input the PK output; the PD output is drug effect over time. The models that are included in the PK repository are:

- one-compartment linear model;
- one-compartment model with MM elimination;
- one-compartment linear model where the volume of distribution (V) is dependent on the dose (D), according to:

$$V = V_0 \exp(-slopeD);$$

- two-compartment linear model;
- full TMDD model [4], without peripheral compartment.

They can all be implemented either with a 0^{th} order input (e.g. IV bolus) or 1^{st} order input (e.g. oral administration).
The models included in the PD repository are:

- direct linear or loglinear model
- Hill model for inhibition or stimulation
- indirect response models [93, 94]
- Claret tumor growth inhibition model [95].

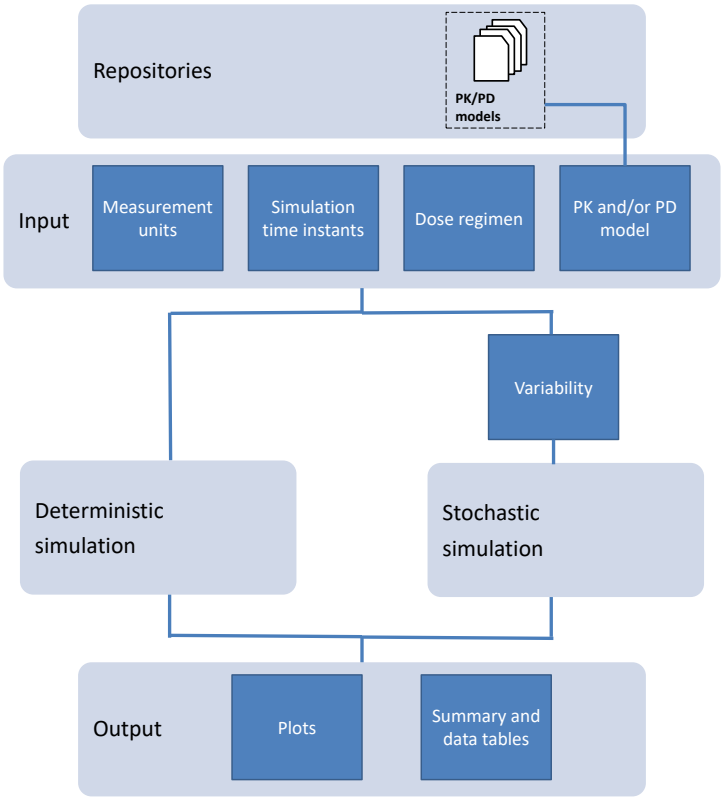

Figure B.1: Conceptual scheme of INES workflow as implemented in the processing code file.

First of all, the user is required to select the fundamental measurement units, i.e. amount, volume, and time units, which will be used by the app to compute all the derived ones (e.g., concentration unit as amount over volume units).
Then, models contained in the two repositories can be simulated, either deterministically or stochastically. Deterministic pharmacokinetic simulations can be performed by setting:

- the desired PK model;
- appropriate parameters values;
- the dosing schedule;
- simulation time instants.

In particular, the dosing schedule is allowed to be quite flexible: different dosing regimens can be superimposed (e.g. a dose of 10 mg/kg on the first day, then 5 mg/kg for the next 5 days). After a deterministic PK simulation, deterministic PD simulations can be performed, by setting:

- the desired PD model; and
- appropriate PD parameters values.

The outputs that are generated by INES after deterministic model simulations are: (i) modifiable plots of concentration vs time, effect vs time, effect vs concentration; (ii) tables summing up model parameters together with their measurement units, dosing schedule (only for PK table), simulation time instants and simulated concentration or effect. Stochastic simulations can be performed with the additional selection of a probabilistic distribution for each model parameter. The user can choose between a normal distribution, i.e. the parameter is expressed as $\theta + \eta$, or lognormal, i.e. the parameter is $\theta \exp \eta$, where θ is the

typical value and $\eta \sim \mathcal{N}(0, \omega^2)$. Variances and covariances of ηs have to be inserted in an OMEGA matrix, analogous to the one used in NONMEM control streams [96]. The typical values θ are inserted as in the deterministic simulation scenario. The user can also select the desired number of stochastic simulations, the simulation seed, and the percentiles to be computed and plotted. A PD stochastic simulation can be performed either giving as input a deterministic PK (hence considering variability only on PD parameters) or a stochastic PK (hence considering variability on both PK and PD parameters).
The outputs that are obtained after stochastic simulations are: (i) modifiable plots of the selected percentiles of concentration or effect vs time, and of effect vs concentration, (ii) tables summing up model parameters (both typical and including variability) together with their measurement units, dosing schedule (only for PK table), simulation time instants, simulation number, and simulated concentrations or effects.

INES was validated via the Matlab-based simulation tool A4S [97] and the software WinNonLin (`https://www.certara.com/software/pkpd-modeling-and-simulation/phoenix-winnonlin/`).

B.1.2 ui.R

User interface, built via ui.R, is subdivided in four main tabs (Figures B.2-B.5). The first tab, "Measurement units" (Figure B.2), is dedicated to the choice of the fundamental measurement units. The derived ones are promptly computed and showed by INES so that the user can perform the necessary unit conversions before selecting parameter values.
The second and third tabs (Figures B.3 and B.4), denoted with "PK analysis" and "(PK-)PD analysis", are designed respectively for the PK and PD settings. Here it is possible to (i) perform model selection; (ii) choose for deterministic or stochastic simulations; (iii) insert

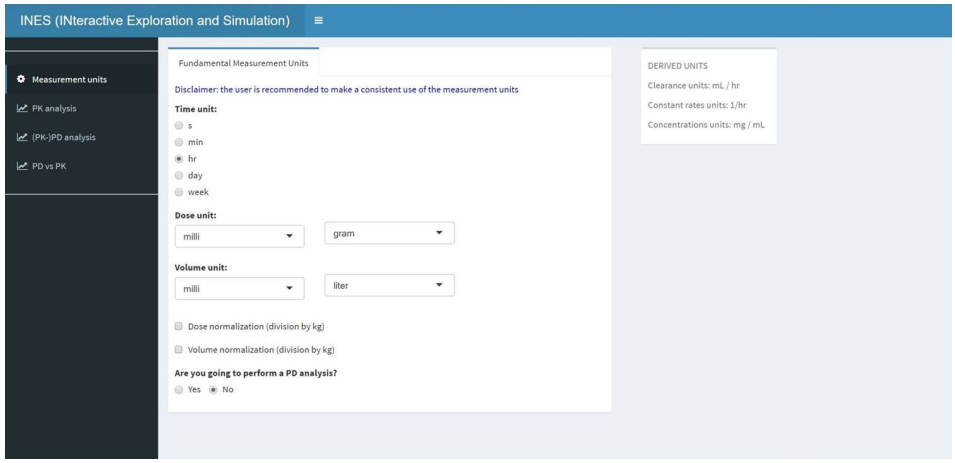

Figure B.2: Screenshot of the INES Shiny application: tab for measurement units selection and definition.

appropriate values for PK or PD parameters and possibly for their variability; (iv) visualize and manipulate graphical outputs, and in particular compare the simulation results with other scenarios, via the upload of an appropriate table; (v) download both plots and tables.
In the PK tab it is also possible to build the desired dosing schedule, which will be reminded by a written message in the PD tab. Dosing schedule can be specified in the section called "Dosage regimens". First of all, the user has to choose the number of regimens; then amount, number of doses, time of first dose and interdose interval need to be entered for each regimen. In case of a standard dosing schedule, e.g. seven doses of 5 mg every 24 hr starting from time 0, the number of regimens is only one. If the dosing schedule is more complicated, the number of superimposed regimens needs to be increased. For instance, if a QW3 schedule is used (three weeks of administration, 1 week of rest) for 8 weeks, the required number of regimens is two: both will have the same amount, number of doses (three) and interdose interval

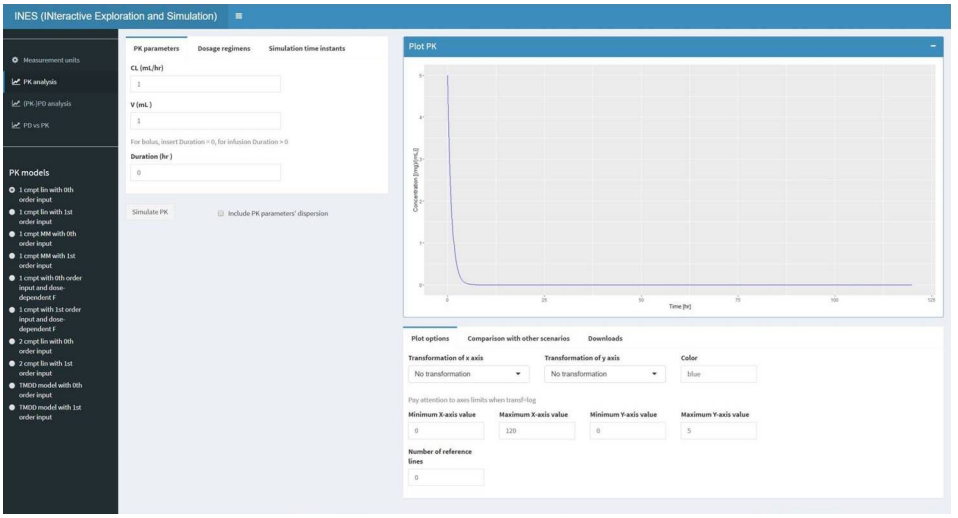

Figure B.3: Screenshot of the INES Shiny application: tab for PK settings and results.

(one week), but the time of first dose will be different (week 0 and week 5). As another example, if a loading dose is required, again the user can select two dosing regimens: the first one with the loading dose, and time of first dose equal to zero, and the second one with the low amount and time of first dose greater than zero.

The intended PK or PD model can be selected from a radio buttons list in the corresponding tab, denoted respectively with "PK models" (Figure B.3) and "PD models" (Figure B.4). According to the selected model, appropriate parameter boxes will appear (called "PK parameters" and "PD parameters"). In here, the user will insert the nominal values of the model parameters in case of deterministic simulation, or the typical value of each parameter in case of stochastic simulation.
In the latter situation, by checking an appropriate checkbox (named "Include PK parameters' dispersion" in the PK tab, and analogously

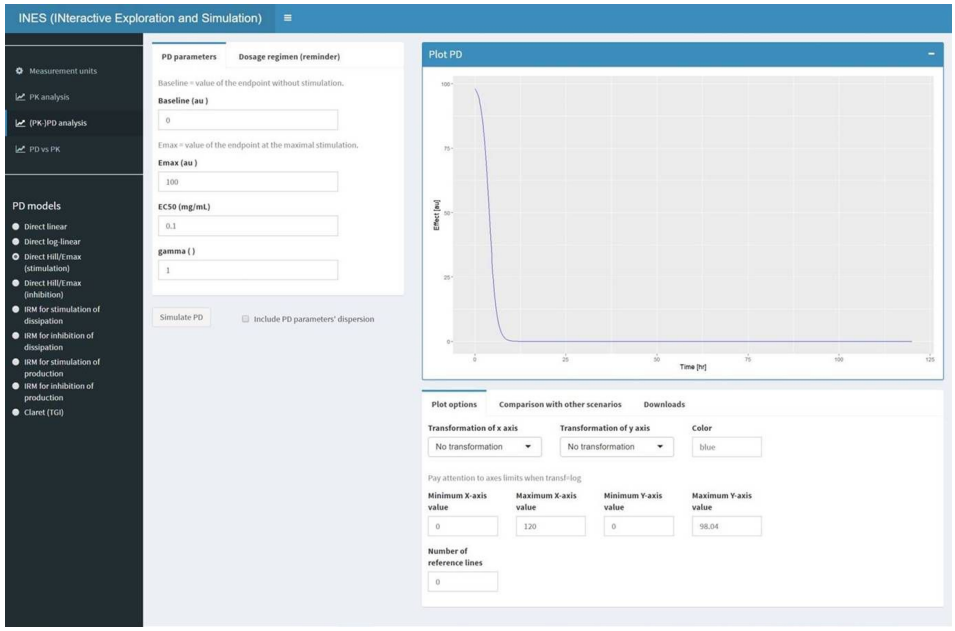

Figure B.4: Screenshot of the INES Shiny application: tab for PD settings and results.

in the PD tab), also a box for the choice of parameters distributions ("Distribution") and variability terms ("OMEGA matrix") will appear. In the "Options" tab, the user can choose the number of random simulations, the seed, and the percentiles to be computed and graphically displayed.
After each PK or (PK-)PD simulation (either deterministic or stochastic), the plot of concentration or effect versus time is displayed in the corresponding tab (Figures B.3 and B.4). Below, a box for output manipulation is provided. In the "Plot options" section, the user can: apply or remove logarithmic transformation to both axes, change the line colour, modify axes limits, and add some reference lines (representing, e.g., efficacy/toxicity thresholds) together with their labels. In "Comparison with other scenario", it is possible to upload an appropriate table (e.g. with results from a previous simulation), choosing the colour and line type of the new plotted curve and the legend labels. The user will also have the possibility to hide again the added curve. In the "Download" section both the final plot and the simulated data can be downloaded.
The fourth tab, "PD vs PK" (Figure B.5), is for comparing PK and PD profiles. In particular, the user can choose to visualize either PD vs PK, or PK and PD vs time overlaid. Analogously to the PK and (PK-)PD tabs, it is possible to modify axes scale and limits, and line color; the final plot is downloadable.

B.2 PTS app: a tool for PTS computation

In the same project, a corollary Shiny application was developed for PTS computation. In the context of early clinical development of

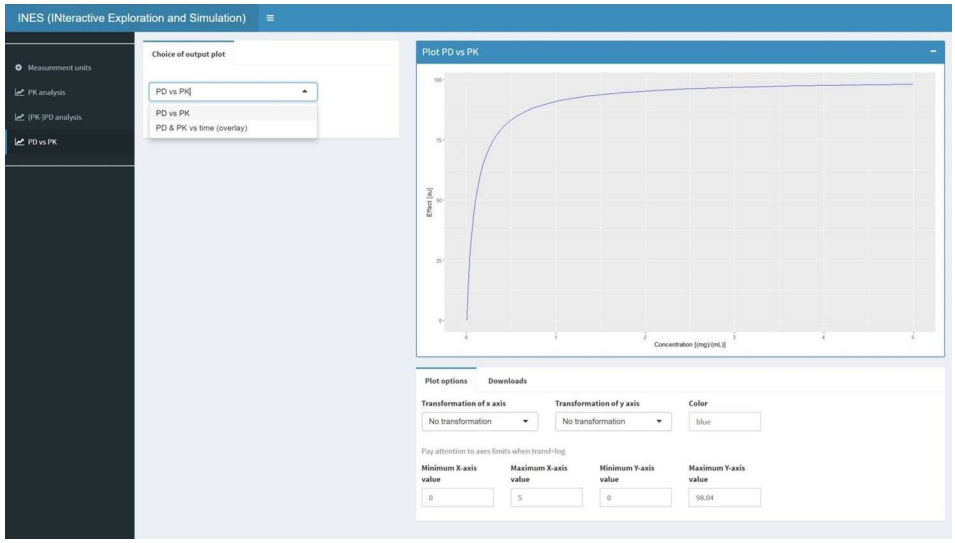

Figure B.5: Screenshot of the INES Shiny application: tab for comparison between PK and PD results.

new compounds, PTS computation is based on the relevant preclinical information (e.g. PK, efficacy and/or safety) to support the transition from preclinical to clinical development and the selection of the clinically relevant doses and dosing regimens [98]. In particular, PTS is computed based on:

- the desired PK or PD endpoint to ensure drug efficacy or limit toxicity (expressed for instance via steady state metrics, e.g.: "CminSS $>$ 5 ng/mL");
- a PK or PK-PD model;
- a range of dose levels and/or dosing regimens (e.g., QD vs BID);
- the vector of typical model parameters;
- the uncertainty and IIV of model parameters (expressed with the appropriate probability distributions).

PTS is evaluated as the ratio of the number of times the endpoint is achieved to the total number of simulations; a sufficiently high number of stochastic simulations is needed for each dose level/regimen. This might entail prohibitive run times: the repeated computation of entire concentration/effect versus time profiles, the exploration of a wide range of dose levels/regimens, and the inclusion of both uncertainty and variability on model parameters may contribute slowing down the app.
For all these reasons, in its current version, the PTS app considers only steady-state PK endpoints for 1 and 2 compartmental linear models (with 0^{th} or 1^{st} order input). Simulation and simultaneous comparison of multiple independent thresholds for the same PK metric are allowed. A case study demonstrating features and performances of this Shiny application was described in [98]. The PTS app, not unlike INES, represents a valuable visualization tool that can facilitate the discussions within program teams and early decision making.

Bibliography

[1] S.F. Marshall, R. Burghaus, V. Cosson, S.Y. Cheung, M. Chenel, O. DellaPasqua, N. Frey, B. Hamrén, L. Harnisch, F. Ivanow, T. Kerbusch, J. Lippert, P.A. Milligan, S. Rohou, A. Staab, J.L. Steimer, C. Tornøe, and S.A.G. Visser (EFPIA MID3 Workgroup). Good Practices in Model-Informed Drug Discovery and Development: Practice, Application, and Documentation. *CPT: pharmacometrics & systems pharmacology*, 5(3):93–122, 2016.

[2] D.K. Shah and A.M. Betts. Towards a platform PBPK model to characterize the plasma and tissue disposition of monoclonal antibodies in preclinical species and human. *Journal of Pharmacokinetics and Pharmacodynamics*, 39:67–86, 2012.

[3] Y. Cao, J.P. Balthasar, and W.J. Jusko. Second-generation minimal physiologically-based pharmacokinetic model for monoclonal antibodies. *Journal of Pharmacokinetics and Pharmacodynamics*, 40(5):597–607, 2013.

[4] D.E. Mager and W.J. Jusko. General pharmacokinetic model for drugs exhibiting target-mediated drug disposition. *Journal of Pharmacokinetics and Pharmacodynamics*, 28(6):507–532, 2001.

[5] D.R. Mould and K.R. Sweeney. The pharmacokinetics and pharmacodynamics of monoclonal antibodies-mechanistic modeling applied to drug development. *Current Opinion in Drug Discovery and Development*, 10(1):84–96, 2007.

[6] E. Mezzalana, S.M. Lavezzi, S. Zamuner, G. De Nicolao, P. Ma, and M. Simeoni, editors. *Integrating Target Mediated Drug Disposition (TMDD) into a minimal physiologically based modelling framework: evaluation of different quasi-steady-state approximations*, number Abstr 3598, 2015. Proceedings of PAGE 2015 meeting.

[7] J. Li, J. Zhi, M. Wenger, N. Valente, A. Dmoszynska, T. Robak, R. Mangat, A. Joshi, and J. Visich. Population pharmacokinetics of rituximab in patients with chronic lymphocytic leukemia. *The Journal of Clinical Pharmacology*, 52(12):1918–1926, 2012.

[8] S.R.B. Allerheiligen. Impact of modeling and simulation: myth or fact? *Clinical Pharmacology and Therapeutics*, 96(4):413–415, 2014.

[9] E. Manolis, S. Rohou, R. Hemmings, T. Salmonson, M. Karlsson, and P.A. Milligan. The role of modeling and simulation in development and registration of medicinal products: output from the EFPIA/EMA modeling and simulation workshop. *CPT: Pharmacometrics and Systems Pharmacology*, 2(2):1–4, 2013.

[10] D.W. Thomas, J. Burns, J. Audette, A. Carrol, C. Dow-Hygelund, and M. Hay. Clinical development success rates 2006-2015. Technical report, BIO Industry Analysis, 2016.

[11] S.M. Lavezzi, E. Borella, L. Carrara, G. De Nicolao, P. Magni, and I. Poggesi. Mathematical modeling of efficacy and safety for

anticancer drugs clinical development. *Expert Opinion on Drug Discovery*, pages 1–17, 2017.

[12] R.A. Rader. (Re) defining biopharmaceutical. *Nature Biotechnology*, 26(7):743–751, 2008.

[13] L. Zhao, E.Y. Shang, and C.G. Sahajwalla. Application of pharmacokinetics-pharmacodynamics/clinical response modeling and simulation for biologics drug development. *Journal of Pharmaceutical Sciences*, 101(12):4367–4382, 2012.

[14] https://www.fda.gov/aboutfda/centersoffices/officeofmedicalproductsandtobacco/cber/ucm133077.htm.

[15] T. Morrow and L. Hull Felcone. Defining the difference: what makes biologics unique. *Biotechnology Healthcare*, 1(4):24–29, 2004.

[16] P.A. Milligan, M.J. Brown, B. Marchant, S.W. Martin, P.H. van der Graaf, N. Benson, G. Nucci, D.J. Nichols, R.A. Boyd, J.W. Mandema, S. Krishnaswami, S. Zwillich, D. Gruben, R.J. Anziano, T.C. Stock, and R.L. Lalonde. Model-Based Drug Development: A Rational Approach to Efficiently Accelerate Drug Development. *Clinical Pharmacology and Therapeutics*, 93(6):502–514, 2013.

[17] R.L. Lalonde, K.G. Kowalski, M.M. Hutmacher, W. Ewy, D.J. Nichols, P.A. Milligan, B.W. Corrigan, P.A. Lockwood, S.A. Marshall, L.J. Benincosa, T.G. Tensfeldt, K. Parivar, M. Amantea, P. Glue, H. Koide, and R. Miller. Model-based drug development. *Clinical Pharmacology and Therapeutics*, 82(1):21–32, 2007.

[18] B. Meibohm and H. Derendorf. Pharmacokinetic/pharmacodynamic studies in drug product development. *Journal of Pharmaceutical Sciences*, 91(1):18–31, 2002.

[19] K. Romero, V. Sinha, S. Allerheiligen, M. Danhof, J. Pinheiro, N. Kruhlak, Y. Wang, S.-J. Wang, J.-M. Sauer J.F. Marier, B. Corrigan, J. Rogers, H.J. Lambers Heerspink, T. Gumbo, P. Vis, P. Waulkins, T. Morrison, W. Gillespie, M.F. Gordon, D. Stephenson, D. Hanna, M. Pfister, R. Lalonde, and T. Colatsky. Modeling and simulation for medical product development and evaluation: highlights from the FDA-C-Path-ISOP 2013 workshop. *Journal of pharmacokinetics and pharmacodynamics*, 41(6):545–552, 2014.

[20] M. Dostalek, I. Gardner, B.M. Gurbaxani, R.H. Rose, and M. Chetty. Pharmacokinetics, pharmacodynamics and physiologically-based pharmacokinetic modelling of monoclonal antibodies. *Clinical Pharmacokinetics*, 52(2):83–124, 2013.

[21] D.R. Mould and B. Meibohm. Drug development of therapeutic monoclonal antibodies. *BioDrugs*, 30(4):275–293, 2016.

[22] Guidance for Industry: Exposure-Response Relationships - Study Design, Data Analysis, and Regulatory Applications. https://www.fda.gov/ucm/groups/fdagov-public/@fdagov-drugs-gen/documents/document/ucm072109.pdf, 2003.

[23] S. Shi. Biologics: an update and challenge of their pharmacokinetics. *Current Drug Metabolism*, 15(3):271–290, 2014.

[24] I.A. Nestorov, L.J. Aarons, and M. Rowland. Physiologically based pharmacokinetic modeling of a homologous series of barbiturates in the rat: a sensitivity analysis. *Journal of Pharmacokinetics and Biopharmaceutics*, 25(4):413–447, 1997.

[25] S. Pilari and W. Huisinga. Lumping of physiologically-based pharmacokinetic models and a mechanistic derivation of classical com-

partmental models. *Journal of Pharmacokinetics and Pharmacodynamics*, 37:365–405, 2010.

[26] J. Kaur, D.K. Badyal, and P.P. Khosla. Monoclonal antibodies: Pharmacological relevance. *Indian Journal of Pharmacology*, 39(1):5–14, 2007.

[27] W. Wang, E.Q. Wang, and J.P. Balthasar. Monoclonal antibody pharmacokinetics and pharmacodynamics. *Clinical Pharmacology and Therapeutics*, 84(5):548–558, 2008.

[28] L.K. Roskos, C.G. Davis, and G.M. Schwab. The clinical pharmacology of therapeutic monoclonal antibodies. *Drug Development Research*, 61(3):108–120, 2004.

[29] R.J. Keizer, A.D. Huitema, and J.H. Schellensand J.H. Beijnen. Clinical pharmacokinetics of therapeutic monoclonal antibodies. *Clinical Pharmacokinetics*, 49(8):493–507, 2010.

[30] G. Köhler and C. Milstein. Continuous cultures of fused cells secreting antibody of predefined specificity. *Nature*, 256(5517):495–497, 1975.

[31] D. Ternant and G. Paintaud. Pharmacokinetics and concentration-effect relationships of therapeutic monoclonal antibodies and fusion proteins. *Expert Opinion on Biological Therapy*, 5(sup1):S37–S47, 2005.

[32] T.T. Hansel, H. Kropshofer, T. Singer, J.A. Mitchell, and A.J. George. The safety and side effects of monoclonal antibodies. *Nature reviews Drug discovery*, 9(4):325–338, 2010.

[33] R. Deng, F. Jin, S. Prabhu, and S. Iyer. Monoclonal antibodies: what are the pharmacokinetic and pharmacodynamic considera-

tions for drug development? *Expert Opinion on Drug Metabolism and Toxicology*, 8(2):141–160, 2012.

[34] G. Levy. Pharmacologic target-mediated drug disposition. *Clinical Pharmacology and Therapeutics*, 56(3):248–252, 1994.

[35] K. Seitz and H. Zhou. Pharmacokinetic Drug-Drug Interaction Potentials for Therapeutic Monoclonal Antibodies: Reality Check. *Journal of Clinical Pharmacology*, 47:1104–1118, 2007.

[36] D.R. Mould and B. Green. Pharmacokinetics and pharmacodynamics of monoclonal antibodies. *BioDrugs*, 24(1):23–39, 2010.

[37] N.L. Berinstein, A.J. Grillo-López, C.A. White, I. Bence-Bruckler, D. Maloney, M. Czuczman, D. Green, J. Rosenberg, P. McLaughlin, and D. Shen. Association of serum Rituximab (IDEC-C2B8) concentration and anti-tumor response in the treatment of recurrent low-grade or follicular non-Hodgkin's lymphoma. *Annals of Oncology*, 9:995–1001, 1998.

[38] R. Bruno, C.B. Washington, J.F. Lu, G. Lieberman, L. Banken, and P. Klein. Population pharmacokinetics of trastuzumab in patients with HEkR2+ metastatic breast cancer. *Cancer Chemotherapy and Pharmacology*, 56(4):361–369, 2005.

[39] T. A. Davis, C. A. White, A. J. Grillo-López, W. S. Velásquez, B. Link, D. G. Maloney, R. O. Dillman, M. E. Williams, A. Mohrbacher, R. Weaver, S. Dowden, and R. Levy. Single-agent monoclonal antibody efficacy in bulky non-Hodgkin's lymphoma: results of a phase II trial of rituximab. *Journal of Clinical Oncology*, 17(6):1851–1857, 1999.

[40] G.J. Wolbink, A.E. Voskuyl, W.F. Lems, E. de Groot, M.T. Nurmohamed, P.P. Tak, B.A.C. Dijkmans, and L. Aarden. Relation

between serum trough infliximab levels, pre- treatment CRP levels and clinical response to infliximab treatment in rheumatoid arthritis. *Annals of the Rheumatic Diseases*, 64(5):704–707, 2005.

[41] P. Ma. Theoretical considerations of target-mediated drug disposition models: simplifications and approximations. *Pharmaceutical Research*, 29(3):866–882, 2012.

[42] H.P. Grimm. Gaining insights into the consequences of target-mediated drug disposition of monoclonal antibodies using quasi-steady-state approximations. *Journal of Pharmacokinetics and Pharmacodynamics*, 36:407–420, 2009.

[43] R.J. Eudy, M.M. Riggs, and M.R. Gastonguay. A priori identifiability of target-mediated drug disposition models and approximations. *The AAPS journal*, 17(5):1280–1284, 2015.

[44] L. Gibiansky, E. Gibiansky, T. Kakkar, and P. Ma. Approximations of the target-mediated drug disposition model and identifiability of model parameters. *Journal of Pharmacokinetics and Pharmacodynamics*, 35:573–591, 2008.

[45] D.E. Mager and W. Krzyzanski. Quasi-equilibrium pharmacokinetic model for drugs exhibiting target-mediated drug disposition. *Pharmaceutical Research*, 22(10):1589–1596, 2005.

[46] L. Gibiansky and E. Gibiansky. Target-medited drug disposition model: approximations, identifiability of model parameters and applications to the population pharmacokinetic-pharmacodynamic modeling of biologics. *Expert Opinion on Drug Metabolism and Toxicology*, 5(7):803–812, 2009.

[47] D.G. Covell, J. Barbet, O.D. Holton, C.D.V. Black, R.J. Parker, and J.N. Weinstein. Pharmacokinetics of Monoclonal Im-

munoglobulin G1, F(ab')2, and Fab' in Mice. *Cancer Research*, 46:3969–3978, 1986.

[48] L.T. Baxter, H. Zhu, D.G. Mackensen, and R.K. Jain. Physiologically Based Pharmacokinetic Model for Specific and Nonspecific Monoclonal Antibodies and Fragments in Normal Tissues and Human Tumor Xenografts in Nude Mice. *Cancer Research*, 54:1517–1528, 1994.

[49] K. Ito, T. Iwatsubo, S. Kanamitsu, Y. Nakajima, and Y. Sugiyama. Quantitative prediction of in vivo drug clearance and drug interactions from in vitro data on metabolism, together with binding and transport. *Annual Review of Pharmacology and Toxicology*, 38(1):461–499, 1998.

[50] Y. Cao and W.J. Jusko. Applications of minimal physiologically-based pharmacokinetic models. *Journal of Pharmacokinetics and Pharmacodynamics*, 39:711–723, 2012.

[51] M. Elmeliegy, P. Lowe, and W. Krzyzanski. Simplification of Complex Physiologically Based Pharmacokinetic Models of Monoclonal Antibodies. *The AAPS Journal*, 16(4):810–842, 2014.

[52] L. Fronton, S. Pilari, and W. Huisinga. Monoclonal antibody disposition: a simplified PBPK model and its implications for the derivation and interpretation of classical compartment models. *Journal of Pharmacokinetics and Pharmacodynamics*, 41:87–107, 2014.

[53] A. Garg and J.P. Balthasar. Physiologically-based pharmacokinetic (PBPK) model to predict IgG tissue kinetics in wild-type and FcRn-knockout mice. *Journal of Pharmacokinetics and Pharmacodynamics*, 34(5):687–709, 2007.

[54] Y. Cao and W.J. Jusko. Incorporating target-mediated drug disposition in a minimal physiologically-based pharmacokinetic model for monoclonal antibodies. *Journal of Pharmacokinetics and Pharmacodynamics*, 41:375–387, 2014.

[55] S.M. Lavezzi, S. Zamuner, G. De Nicolao, P. Ma, and M. Simeoni, editors. *Structural and practical identifiability of some mPBPK-TMDD models*, number Abstr 5876, 2016. Proceedings of PAGE 2016 meeting.

[56] D. Padhi, G. Jang, B. Stouch, L. Fang, and E. Posvar. Single-Dose, Placebo-Controlled, Randomized Study of AMG 785, a Sclerostin Monoclonal Antibody. *Journal of Bone and Mineral Research*, 26(1):19–26, 2011.

[57] K.A.P. McLean and K.B. McAuley. Mathematical modelling of chemical processes-obtaining the best model predictions and parameter estimates using identifiability and estimability procedures. *The Canadian Journal of Chemical Engineering*, 90(2):351–366, 2012.

[58] A. Sedoglavic, editor. *A probabilistic algorithm to test local algebraic observability in polynomial time*. ACM, 2001. Proceedings of the International Symposium on Symbolic and Algebraic Computation.

[59] J. Karlsson, M. Anguelova, and M. Jirstrand. An efficient method for structural identifiability analysis of large dynamic systems. *IFAC Proceedings Volumes*, 45(16):941–946, 2012.

[60] M. Anguelova, J. Karlsson, and M. Jirstrand. Minimal output sets for identifiability. *Mathematical Biosciences*, 239(1):139–153, 2012.

[61] T. Hastie, R. Tibshirani, and J. Friedman. *The elements of statistical learning*. Springer, 2008. 265-267.

[62] A. Hooker, C.E. Staatz, and M.O. Karlsson. Conditional Weighted Residuals (CWRES): A Model Diagnostic for the FOCE Method. *Pharmaceutical Research*, 24(12):2187–2197, 2007.

[63] C. Bazzoli, S. Retout, and F. MentrÃ©. Design evaluation and optimisation in multiple response nonlinear mixed effect models: PFIM 3.0. *Computer Methods and Programs in Biomedicine*, 98:55–65, 2010.

[64] N.H. Holford, H.C. Kimko, J.P.R. Monteleone, and C.C. Peck. Simulation of clinical trials. *Annual Review of Pharmacology and Toxicology*, 40(1):209–234, 2000.

[65] J.D. Wetherington, M. Pfister, C. Banfield, J.A. Stone, R. Krishna, S. Allerheiligen, and D.M. Grasela. Model-Based Drug Development: Strengths, Weaknesses, Opportunities, and Threats for Broad Application of Pharmacometrics in Drug Development. *The Journal of Clinical Pharmacology*, 50(S9), 2010.

[66] L.A. Peletier and J. Gabrielsson. Dynamics of target-mediated drug disposition: characteristic profiles and parameter identification. *Journal of Pharmacokinetics and Pharmacodynamics*, 39:429–451, 2012.

[67] RITUXAN® (rituximab) prescribing information, 2016.

[68] K. Fischer, P. Cramer, R. Busch, S. Stilgenbauer, J. Bahlo, C.D. Schweighofer, S. Böttcher, P. Staib, M. Kiehl, M.J. Eckart, G. Kranz, V. Goede, T. Elter, A. Bühler, D. Winkler, M. Kneba, H. Döhner, B.F. Eichhorst, M. Hallek, and C.-M. Wendtner. Bendamustine combined with rituximab in patients with relapsed

and/or refractory chronic lymphocytic leukemia: a multicenter phase II trial of the German Chronic Lymphocytic Leukemia Study Group. *Journal of Clinical Oncology*, 29(26):3559–3566, 2011.

[69] A. Chanan-Khan, P. Cramer, F. Demirkan, G. Fraser, R. Santucci Silva, S. Grosicki, A. Pristupa, A. Janssens, J. Mayer, N.L. Bartlett, M.-S. Dilhuydy, H. Pylypenko, J. Loscertales, A. Avigdor, S. Rule, D. Villa, O. Samoilova, P. Panagiotidis, A. Goy, A. Mato, M.A. Pavlovsky, C. Karlsson, M. Mahler, M. Salman, S. Sun, C. Phelps, S. Balasubramanian, A. Howes, and M. Hallek. Ibrutinib combined with bendamustine and rituximab compared with placebo, bendamustine, and rituximab for previously treated chronic lymphocytic leukaemia or small lymphocytic lymphoma (HELIOS): a randomised, double-blind, phase 3 study. *The Lancet Oncology*, 17(2):200–211, 2016.

[70] IMBRUVICA® (ibrutinib) prescribing information, 2016.

[71] J.R. Brown, J.C. Barrientos, P.M. Barr, I.W. Flinn, J.A. Burger, A. Tran, F. Clow, D.F. James, T. Graef, J.W. Friedberg, K. Rai, and S. O'Brien. The Bruton tyrosine kinase inhibitor ibrutinib with chemoimmunotherapy in patients with chronic lymphocytic leukemia. *Blood*, 125(19):2915–2922, 2015.

[72] P. Cramer, F. Demirkan, G. Fraser, A. Pristupa, N.L. Bartlett, M.-S. Dilhuydy, J. Loscertales, A. Avigdor, S.A. Rule, O. Samoilova, A. Goy, S. Ganguly, I. Poggesi, S.M. Lavezzi, G. De Nicolao, J. de Jong, M. Neyens, M. Salman, A. Howes, and M. Mahler, editors. *Systemic Exposure of Rituximab Increased By Ibrutinib: Pharmacokinetic Results from the Helios Trial*, number 4403, 2016. Proceedings of the 58th ASH Annual Meeting and Exposition.

[73] Paula Cramer, Fatih Demirkan, Graeme Fraser, Alexander Pristupa, Nancy L. Bartlett, Marie-Sarah Dilhuydy, Javier Loscertales, Abraham Avigdor, Simon A. Rule, Olga Samoilova, Andre Goy, Siddhartha Ganguly, Italo Poggesi, Silvia Maria Lavezzi, Giuseppe De Nicolao, Jan de Jong, Martine Neyens, Mariya Salman, Angela Howes, and Michelle Mahler, editors. *Ibrutinib increases the systemic exposure of rituximab: pharmacokinetic results from the helios trial*, number 235, 2017. Proceedings of the 14th ICML.

[74] M. Hallek, B.D. Cheson, D. Catovsky, F. Caligaris-Cappio, G. Dighiero, H. Döhner, P. Hillmen, M.J. Keating, E. Montserrat, K.R. Rai, and T.J. Kipps. Guidelines for the diagnosis and treatment of chronic lymphocytic leukemia: a report from the International Workshop on Chronic Lymphocytic Leukemia updating the National Cancer Institute-Working Group 1996 guidelines. *Blood*, 111(12):5446–5456, 2008.

[75] M. A. Rudek, C.H. Chau, W.D. Figg, and H.L. McLeod. *Handbook of anticancer pharmacokinetics and pharmacodynamics*. Springer, New York, 2014.

[76] J. Golay, G. Semenzato, A. Rambaldi, R. Fo à, G. Gaidano, E. Gamba, F. Pane, A. Pinto, G. Specchia, F. Zaja, and M. Regazzi. Lessons for the clinic from rituximab pharmacokinetics and pharmacodynamics. *mAbs*, 5(6):826–837, 2013.

[77] J.M. Harrold, R.M. Straubinger, and D.E. Mager. Combinatorial chemotherapeutic efficacy in non-Hodgkin lymphoma can be predicted by a signaling model of CD20 pharmacodynamics. *Cancer Research*, 72:1632–1641, 2012.

[78] A. Yin, J. Li, D. Hurst, and J. Visich. Population pharmacokinetics (PK) and association of PK and clinical outcomes of rit-

uximab in patients with non-Hodgkin's lymphoma. *Journal of Clinical Oncology*, 28(suppl 15):e13108, 2010.

[79] I. Poggesi, M.L. Sardu, E. Marostica, J. Sukbuntherng, B.Y. Chang, J. de Jong, X. Woot de Trixhe, A. Vermeulen, G. De Nicolao, S.M. O'brien, J.C. Byrd, R.H. Advani, D.F. James, W. Deraedt, D. Beaupre, and M. Wang. Population pharmacokinetic-pharmacodynamic (PKPD) modeling of ibrutinib in patients with B-cell malignancies. In *AACR Special Conference on Hematologic Malignancies: Translating Discoveries to Novel Therapies*, number Abstract B19, 2015.

[80] R.H. Advani, J.J. Buggy, J.P. Sharman, S.M. Smith, T.E. Boyd, B. Grant, K.S. Kolibaba, R.R. Furman, S. Rodriguez, B.Y. Chang, J. Sukbuntherng, R. Izumi, A. Hamdy, E. Hedrick, and N.H. Fowler. Bruton tyrosine kinase inhibitor ibrutinib (PCI-32765) has significant activity in patients with relapsed/refractory B-cell malignancies. *Journal of Clinical Oncology*, 31(1):88–94, 2012.

[81] Food &Drug Administration. Center for Drug Evaluation and Research. Approval package for Application Number: BLA 103705 / S-5344. https://www.accessdata.fda.gov/drugsatfda_docs/bla/2011/103705orig1s5344.pdf, 2011.

[82] M.R. Gastonguay, editor. *Full covariate models as an alternative to methods relying on statistical significance for inferences about covariate effects: a review of methodology and 42 case studies*, number Abstr 2229, 2011. Proceedings of PAGE 20.

[83] J. Li, M. Levi, J.-E. Charoin, N. Frey, T. Kheoh, S. Ren, M. Woo, A. Joshi, N. Valente, and N. 'Shasha' Jumbe, editors. *Rituximab*

Exhibits a Long Half-Life Based on a Population Pharmacokinetic Analysis in Non-Hodgkin's Lymphoma (NHL) Patients, number 2371, 2008. Proceedings of the ASH Annual Meeting and Exposition 2007.

[84] K. Tobinai, T. Igarashi, K. Itoh, Y. Kobayashi, M. Taniwaki, M. Ogura, T. Kinoshita, T. Hotta, K. Aikawa, K. Tsushita, A. Hiraoka, Y. Matsuno, S. Nakamura, S. Mori, and Y. Ohashi. Japanese multicenter phase II and pharmacokinetic study of rituximab in relapsed or refractory patients with aggressive B-cell lymphoma. *Annals of Oncology*, 15(5):821–830, 2004.

[85] M. Tout, A.-L. Gagez, S. Leprêtre, V. Gouilleux-Gruart, N. Azzopardi, A. Delmer, M. Mercier, L. Ysebaert, K. Laribi, H. Gonzalez, G. Paintaud, G. Cartron, and D. Ternant. Influence of FCGR3A-158V/F Genotype and Baseline CD20 Antigen Count on Target-Mediated Elimination of Rituximab in Patients with Chronic Lymphocytic Leukemia: A Study of FILO Group. *Clinical Pharmacokinetics*, 56(6):635–647, 2017.

[86] D. Daydé, D. Ternant, M. Ohresser, S. Lerondel, S. Pesnel, H. Watier, A. Le Pape, P. Bardos, G. Paintaud, and G. Cartron. Tumor burden influences exposure and response to rituximab: pharmacokinetic-pharmacodynamic modeling using a syngeneic bioluminescent murine model expressing human CD20. *Blood*, 113(16):3765–3772, 2009.

[87] C. Liu, J. Yu, H. Li, J. Liu, Y. Xu, P. Song, Q. Liu, H. Zhao, J. Xu, V.E. Maher, B.P. Booth, G. Kim, A. Rahman, and Y. Wang. Association of time-varying clearance of nivolumab with disease dynamics and its implications on exposure response analysis. *Clinical Pharmacology and Therapeutics*, 101(5):657–666, 2017.

[88] E. Carson and C. Cobelli. *Modelling methodology for physiology and medicine*. Newnes, 2013.

[89] V. Shivva, J. Korell, I.G. Tucker, and S.B. Duffull. An approach for identifiability of population pharmacokinetic-pharmacodynamic models. *CPT: Pharmacometrics and Systems Pharmacology*, 2(6):1–9, 2013.

[90] M. Ashyraliyev, Y. Fomekong-Nanfack, J.A. Kaandorp, and J.G. Blom. Systems biology: parameter estimation for biochemical models. *The FEBS journal*, 276(4):886–902, 2009.

[91] J. Shao. *Mathematical Statistics*. Springer, 1998.

[92] S. Retout, E. Comets, A. Samson, and F. Mentré. Design in nonlinear mixed effects models: optimization using the Fedorov-Wynn algorithm and power of the Wald test for binary covariates. *Statistics in Medicine*, 26:5162–5179, 2007.

[93] N.L. Dayneka, V. Garg, and W.J. Jusko. Comparison of four basic models of indirect pharmacodynamic responses. *Journal of Pharmacokinetics and Pharmacodynamics*, 21(4):457–478, 1993.

[94] A. Sharma and W.J. Jusko. Characteristics of indirect pharmacodynamic models and applications to clinical drug responses. *British Journal of Clinical Pharmacology*, 45(3):229–239, 1998.

[95] L. Claret, P. Girard P.M. Hoff, E. Van Cutsem, K.P. Zuideveld, K. Jorga, J. Fagerberg, and R. Bruno. Model-based prediction of phase III overall survival in colorectal cancer on the basis of phase II tumor dynamics. *Journal of Clinical Oncology*, 27(25):4103–4108, 2009.

[96] A.J. Boeckmann, L.B. Sheiner, and S.L. Beal. *NONMEM users guide: Part V*.

[97] M. Germani, F. Del Bene, M. Rocchetti, and P.H. Van Der Graaf. A4S: A user-friendly graphical tool for pharmacokinetic and pharmacodynamic (PK/PD) simulation. *Computer Methods and Programs in Biomedicine*, 110(2):203–214, 2013.

[98] S.M. Lavezzi, Y. Cherkas, N. Haddish-Berhane, S. Jagannatha, G. De Nicolao, D. Ouellet, and I. Poggesi, editors. *A Shiny App for the Probability of Technical Success of a New Molecular Entity in the Preclinical to Clinical Translational Phase*, number Abstr 7160, 2017. Proceedings of PAGE 2017 meeting.

List of publications

Articles in peer reviewed journals

- **Lavezzi S.M.***, Borella E.*, Carrara L., De Nicolao G., Magni P., Poggesi I. (2018). Mathematical modeling of efficacy and safety for anticancer drugs clinical development. Expert Opinion on Drug Discovery, Vol. 13 (1): 5-21 (**shared first-authorship*).

- Carrara L., **Lavezzi S.M.**, Borella E., De Nicolao G., Magni P., Poggesi I. (2017). Current mathematical models for cancer drug discovery. Expert Opinion on Drug Discovery, Vol. 12 (8): 785-799.

Contributions to conference proceedings

- Cramer P., Demirkan F., Fraser G., Pristupa A., Bartlett N.L., Dilhuydy M.-S., Loscertales J., Avigdor A., Rule S.A., Samoilova O., Goy A., Ganguly S., Poggesi I., **Lavezzi S.M.**, De Nicolao G., de Jong J., Neyens M., Salman M., Howes A., Mahler M.. Ibrutinib increases the systemic exposure of rituximab: pharma-

cokinetic results from the Helios trial, 14-ICML, Hematological Oncology, 35 (S2), 232-233 (2017) [http://onlinelibrary.wiley.com /doi/10.1002/hon.2438_95/epdf]

- Cramer P., Demirkan F., Fraser G., Pristupa A., Bartlett N.L., Dilhuydy M.-S., Loscertales J., Avigdor A., Rule S.A., Samoilova O., Goy A., Ganguly S., Poggesi I., **Lavezzi S.M.**, De Nicolao G., de Jong J., Neyens M., Salman M., Howes A., Mahler M.. Systemic Exposure of Rituximab Increased By Ibrutinib: Pharmacokinetic Results from the Helios Trial, ASH 58 (Blood 2016), Abstr 4403 [http://www.bloodjournal.org/content/128/22/4403]

- **Lavezzi S.M.**, de Jong J., Neyens M., Cramer P., Dermikan F., Fraser G., Pristupa A., Bartlett N., Dilhuydy M.-S., Loscertales J., Avigdor A., Rule S., Samoilova O., Goy A., Ganguly S., Salman M., Howes A., Mahler M, De Nicolao G., Poggesi I.. Modelling of rituximab clearance reduction due to ibrutinib co-administration, PAGE 26 (2017), Abstr 7139 [www.page-meeting.org/?abstract=7139]

- **Lavezzi S.M.**, Cherkas Y., Haddish-Berhane N., Jagannatha S., De Nicolao G., Ouellet D., Poggesi I.. A Shiny App for the Probability of Technical Success of a New Molecular Entity in the Preclinical to Clinical Translational Phase, PAGE 26 (2017), Abstr 7160 [www.page-meeting.org/?abstract=7160]

- **Lavezzi S.M.**, Zamuner S., De Nicolao G., Ma P., Simeoni M.. Structural and practical identifiability of some mPNPK-TMDD models, PAGE 25 (2016), Abstr 5876 [http://www.page-meeting.org/default.asp?abstract=5876]

- Borella E., Carrara L., **Lavezzi S.M.**, Massaiu I., Sauta E., Tosca E.M., Vitali F., Zucca S., Pasotti L., De Nicolao G.,

Magni P.. Methods and tools for multiscale modelling in Systems Pharmacology: a review, PAGE 25 (2016), Abstr 5793 [http://www.page-meeting.org/default.asp?abstract=5793]

- Mezzalana E., **Lavezzi S.M.**, Zamuner S., De Nicolao G., Ma P., Simeoni M.. Integrating Target Mediated Drug Disposition (TMDD) into a minimal physiologically based modelling framework: evaluation of different quasi-steady-state approximations, PAGE 24 (2015) Abstr 3598 [www.page-meeting.org/?abstract=3598]

- **Lavezzi S.M.**, Mezzalana E., De Nicolao G.. Toxicity assessment via drug-drug interaction modeling for trabectedin in patients with advanced malignancies, PAGE 24 (2015) Abstr 3393 [www.page-meeting.org/?abstract=3393]

- Borella E., Carrara L., **Lavezzi S.M.**, Mezzalana E., Pasotti L., De Nicolao G., Magni P.. Evaluation of software tools for Bayesian estimation on population models with count and continuous data, PAGE 24 (2015) Abstr 3452 [www.page-meeting.org/?abstract=3452]

Acknowledgements

First of all, I want to thank my advisor, prof. Giuseppe De Nicolao, who supervised me during the PhD course and who gave me his guidance and constant support. Thank you for giving me the opportunity to work with you these last three years.

I would like to express my sincere gratitude also to Monica Simeoni and Italo Poggesi, who helped me through new and stimulating research projects, being always ready to answer my questions and provide their precious insight.

A very special gratitude goes to my friends and former colleagues at BMS lab, Enrica Mezzalana and Maria Luisa Sardu: you were the first to teach me the basis of pharmacometrics, with patience and trust in me. You also demonstrated me that a PhD course involves not only professional but also personal growth.

A special mention is owed to my friends and colleagues Elisa Borella and Elena Maria Tosca: thank you for our "brain-storming moments", and also for the laughs, of course!
I am also grateful to Elisabetta Sauta and Ilaria Massaiu, for all the time spent together (especially coffee breaks!) talking about fun and serious things.

I thank also Eleonora Marostica and Alberto Russu, who made me feel welcome during the period abroad.

Heartfelt thanks to my parents and to my sister: even if maybe they do not grasp what my research activity is really about, as long as I'm happy with it, they're happy for me.
Many thanks also to Marcello, for his love and for being always there for me with his advices and encouragements.

Finally, I thank also all my friends, for taking my mind off things during the rough days, all the people who worked with me, for their help, and all the members of the BMS lab, for spending the last three years together.